

# CANADIAN THESES ON MICROFICHE

I.S.B.N.

# THESES CANADIENNES SUR MICROFICHE



National Library of Canada  
Collections Development Branch

Canadian Theses on  
Microfiche Service

Ottawa, Canada  
K1A 0N4

Bibliothèque nationale du Canada  
Direction du développement des collections

Service des thèses canadiennes  
sur microfiche

## NOTICE

The quality of this microfiche is heavily dependent upon the quality of the original thesis submitted for microfilming. Every effort has been made to ensure the highest quality of reproduction possible.

If pages are missing, contact the university which granted the degree.

Some pages may have indistinct print especially if the original pages were typed with a poor typewriter ribbon or if the university sent us a poor photocopy.

Previously copyrighted materials (journal articles, published tests, etc.) are not filmed.

Reproduction in full or in part of this film is governed by the Canadian Copyright Act, R.S.C. 1970, c. C-30. Please read the authorization forms which accompany this thesis.

**THIS DISSERTATION  
HAS BEEN MICROFILMED  
EXACTLY AS RECEIVED**

## AVIS

La qualité de cette microfiche dépend grandement de la qualité de la thèse soumise au microfilmage. Nous avons tout fait pour assurer une qualité supérieure de reproduction.

S'il manque des pages, veuillez communiquer avec l'université qui a conféré le grade.

La qualité d'impression de certaines pages peut laisser à désirer, surtout si les pages originales ont été dactylographiées à l'aide d'un ruban usé ou si l'université nous a fait parvenir une photocopie de mauvaise qualité.

Les documents qui font déjà l'objet d'un droit d'auteur (articles de revue, examens publiés, etc.) ne sont pas microfilmés.

La reproduction, même partielle, de ce microfilm est soumise à la Loi canadienne sur le droit d'auteur, SRC 1970, c. C-30. Veuillez prendre connaissance des formules d'autorisation qui accompagnent cette thèse.

**LA THÈSE A ÉTÉ  
MICROFILMÉE TELLE QUE  
NOUS L'AVONS REÇUE**

**Canada**



National Library of Canada

Bibliothèque nationale du Canada

Canadian Theses Division

Division des thèses canadiennes

105

Ottawa, Canada  
K1A 0N4

56909

**PERMISSION TO MICROFILM — AUTORISATION DE MICROFILMER**

• Please print or type — Écrire en lettres moulees ou dactylographier

Full Name of Author — Nom complet de l'auteur

MARILYN KAY KONKIN

Date of Birth — Date de naissance

April 18, 1954

Country of Birth — Lieu de naissance

CANADA

Permanent Address — Résidence fixe

#114 - 11512 - 40th Ave - Edmonton, Alta. T6J 0R6

Title of Thesis — Titre de la thèse

ANNEALING EFFECTS IN TUNNEL JUNCTIONS

University — Université

University of Alberta — Edmonton

Degree for which thesis was presented — Grade pour lequel cette thèse fut présentée

Ph D.

Year this degree conferred — Année d'obtention de ce grade

1981

Name of Supervisor — Nom du directeur de thèse

John G. Adler

Permission is hereby granted to the NATIONAL LIBRARY OF CANADA to microfilm this thesis and to lend or sell copies of the film

The author reserves other publication rights, and neither the thesis nor extensive extracts from it may be printed or otherwise reproduced without the author's written permission.

L'autorisation est, par la présente, accordée à la BIBLIOTHÈQUE NATIONALE DU CANADA de microfilmer cette thèse et de prêter ou de vendre des exemplaires du film

L'auteur se réserve les autres droits de publication, ni la thèse ni de longs extraits de celle-ci ne doivent être imprimés ou autrement reproduits sans l'autorisation écrite de l'auteur

Date

July 30, 1981

Signature

Marilyn K. Konkinn

THE UNIVERSITY OF ALBERTA

ANNEALING EFFECTS IN TUNNEL JUNCTIONS

by



MARILYN KAY KONKIN

A THESIS

SUBMITTED TO THE FACULTY OF GRADUATE STUDIES AND RESEARCH  
IN PARTIAL FULFILMENT OF THE REQUIREMENTS FOR THE DEGREE  
OF DOCTOR OF PHILOSOPHY

IN

PHYSICS

DEPARTMENT OF PHYSICS

EDMONTON, ALBERTA

FALL 1981

THE UNIVERSITY OF ALBERTA

RELEASE FORM

NAME OF AUTHOR                    MARILYN KAY KONKIN  
TITLE OF THESIS                    ANNEALING EFFECTS IN TUNNEL  
  JUNCTIONS  
DEGREE FOR WHICH THESIS WAS PRESENTED            Ph.D.  
YEAR THIS DEGREE GRANTED                    1981

Permission is hereby granted to THE UNIVERSITY OF ALBERTA LIBRARY to reproduce single copies of this thesis and to lend or sell such copies for private, scholarly or scientific research purposes only.

The author reserves other publication rights, and neither the thesis nor extensive extracts from it may be printed or otherwise reproduced without the author's written permission.

(Signed) . . . *Marilyn K. Konkina*

PERMANENT ADDRESS:



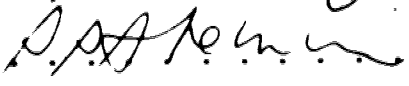


#114 - 11512 - 40 Avenue,  
Edmonton, Alberta T6J 0R6

Dated . . . June 16 . . . . 1981

THE UNIVERSITY OF ALBERTA

FACULTY OF GRADUATE STUDIES AND RESEARCH

The undersigned certify that they have read, and recommend to the Faculty of Graduate Studies and Research, for acceptance, a thesis entitled ANNEALING EFFECTS IN TUNNEL JUNCTIONS submitted by MARILYN KAY KONKIN in partial fulfilment of the requirements for the degree of Doctor of Philosophy in Physics.

  
.....  
Supervisor  
  
.....  
  
.....  
  
.....  
  
.....  
Robert C. Jaklevic  
External Examiner

Date . . June 16 . . 1981

TO

SAL

SARNATH

AND

THE OTHERS

## ABSTRACT

'Much work' has been done in recent years studying inelastic electron tunneling in metal-insulator-metal tunnel junctions. Inelastic Electron Tunneling Spectroscopy (IETS) has become a method for investigating various molecules within a tunnel junction's insulating layer. In particular, Al-insulator-Pb tunnel junctions, where the insulator is aluminum oxide deliberately doped with organic molecules, have become fairly popular. The IET spectra produced, however, are complex and decipherable primarily via knowledge of infrared and Raman spectroscopy. This thesis explores the undoped Al-Al oxide-Pb tunnel junction itself. By studying how the junction ages - or anneals - insight into the nature of the aluminum oxide insulator, and its interaction with the Al and Pb metal electrodes is gained. Also, by applying a voltage of either polarity (i.e. Al positive or negative) across the two electrodes during annealing, or by using a cover electrode metal other than Pb, one acquires additional knowledge about the junction.

## ACKNOWLEDGEMENTS

I wish to thank my supervisor, Dr. J.G. Adler for his guidance throughout the course of this thesis; I learned much about the world of the contemporary physicist. I also wish to thank him for supplying funds which allowed me to attend a number of conferences.

Thanks are due to Don Mullin for his technical assistance and help in many facets of work in the laboratory.

Special acknowledgement is given to D. Latta, S. Rogers, and R. Rogers for supplying liquid helium.

I wish to thank the Physics Department and the Natural Sciences and Engineering Research Council of Canada for financial support. I am also grateful to the French LT 15 committee for supplying financial support which aided my attending LT 15 in Grenoble.

The continuing interest in this project by friends and family has been greatly appreciated.

I wish to mention JRC who understood so much.

Finally, I wish to extend a very special thanks to Mrs. Ruth Nelson for her extra careful attention and excellence in the typing of this thesis.



## TABLE OF CONTENTS

	PAGE
CHAPTER 1	1
INTRODUCTION	
1.1 Preamble	1
CHAPTER 2	2
THEORETICAL CONSIDERATIONS	
2.1 Introduction	2
2.2 Elastic Tunneling	5
CHAPTER 3	11
INELASTIC ELECTRON TUNNELING THEORY	
3.1 Introduction	11
3.2 Vibrational Spectroscopy	12
3.3 Simple Models for Inelastic Electron Tunneling	28
3.4 More Complex Models for Inelastic Electron Tunneling	35
3.5 Transfer Hamiltonians since 1976	38
CHAPTER 4	44
EXPERIMENTAL TECHNIQUES	
4.1 Junction Preparation	44
4.2 Modulation Spectroscopy	55
4.3 Measurement of Tunneling Information	66
4.4 Annealing Procedure	70
CHAPTER 5	76
DATA ANALYSIS AND FUNDAMENTAL INFORMATION	
5.1 Introduction	76
5.2 Peak Assignments	76
5.3 Data from Tunneling Curves	86
CHAPTER 6	97
RESULTS AND DISCUSSION	
6.1 Introduction	97
6.2 Thermal Annealing	97
6.3 Voltage Annealing	116

## TABLE OF CONTENTS

	PAGE
CHAPTER 6	RESULTS AND DISCUSSION (continued)
6.4	Voltage Annealing with Alternating Polarity 142
6.5	Origin of the Intrinsic Electric Field 154
6.6	Annealing of Al-Al Oxide-Metal Junctions 158
CHAPTER 7	SUMMARY AND CONCLUSIONS 183
7.1	Conclusions 183
7.2	Afterthoughts 185
7.3	Suggestions for Further Work 187
BIBLIOGRAPHY	189
APPENDIX 1	INSTABILITY PAPERS 205
APPENDIX 2	IETS PAPERS 210

LIST OF TABLES

TABLE		PAGE
4.1	Evaporation materials	47
4.2	Plasma discharge characteristics	51
5.1	IET peak assignments	79
6.1	Ionic radii of metals	166

## LIST OF FIGURES

FIGURE		PAGE
2.1	Tunneling experiment.	3
2.2	Energy level diagram for M-I-M junction.	6
3.1	I vs V, $\sigma$ vs V, and $d\sigma/dV$ vs V.	13
3.2	Various molecular vibrations.	16
3.3	Excitation of N <sub>2</sub> and NO.	21
3.4	Vibrational modes of CO <sub>2</sub> .	26
3.5	Inelastic electron tunneling energy level diagram.	30
4.1	Tunnel junction layout.	45
4.2	Dipstick and junction holder.	53
4.3	Modulation spectroscopy.	56
4.4	General characteristic and response.	58
4.5	Idealized response.	60
4.6	Fourier decomposition.	62
4.7	Simple bridge circuit.	67
4.8	Layout of data acquisition system.	71
4.9	Voltage annealing.	74
5.1	Typical Al-Al oxide-Pb spectrum.	77
5.2	OH stretching peak at 450 meV.	82
5.3	Polynomial fit of oxide conductance curve.	87
5.4	3rd degree fit for 450 meV peak background.	90
5.5	1st degree fit for 118 meV peak background.	92
5.6	Limits for intensity calculation for 85 and 118 meV peaks.	94
6.1	$R_t/R_o$ vs t.	100

## LIST OF FIGURES

FIGURE	PAGE
6. 2 Al-Al oxide-Pb spectrum.	102
6. 3 Changes in the OH peak.	104
6. 4 $s$ vs $t$ for thermally annealed junction.	107
6. 5 Changes in $\Delta\phi$ , $\phi_1$ , $\phi_2$ , and $F(450)$ .	109
6. 6 Reorientation of OH groups.	112
6. 7 Intensities of 118 and 450 meV peaks.	114
6. 8 $R_t/R_b$ vs $t-t_b$ .	119
6. 9 $\Delta\phi - \Delta\phi_b$ vs $t-t_b$ .	121
6.10 $R_t/R_o$ vs $t$ .	124
6.11 $\phi_1$ behaviour for thermal and voltage annealed junctions.	126
6.12 Effect on $\Delta\phi$ and $R_t/R_o$ of FP bias removal.	129
6.13 Aging effect.	131
6.14 Spectra for virgin and voltage annealed sample.	134
6.15 Intensity behaviour for RP voltage annealed junction.	136
6.16 Interaction between Al ions and hydroxyl groups.	139
6.17 Resistance behaviour for alternating polarity voltage annealed junction.	144
6.18 $s$ vs $t$ .	147
6.19 Behaviour of $\phi_1$ and $\phi_2$ with respect to time for alternating polarity voltage annealing.	149
6.20 $\phi_1$ and $\phi_2$ behaviour including control junction.	152
6.21 Negative oxide ion layer.	156

## LIST OF FIGURES

FIGURE		PAGE
6.22	$R_t/R_o$ vs t for Al-Al oxide-metal junctions.	160
6.23	F(450) vs ionic radius.	163
6.24	$R_M A_M / R_{Pb} A_{Pb}$ vs ionic radius.	167
6.25	IET spectrum of Al-Al oxide-Al junction.	169
6.26	IET spectrum of Al-Al oxide-Mg junction.	171
6.27	$\phi_1$ and $\phi_2$ vs t for Al-Al oxide-Al junction.	174
6.28	$\phi_1$ and $\phi_2$ vs t for Al-Al oxide-Ag junction.	177
6.29	s vs t for Al-Al oxide-Ag junction.	181

# CHAPTER 1

## INTRODUCTION

### 1.1. Preamble

This thesis sets out to describe some of the effects which occur in aluminum-aluminum oxide-lead (Al-oxide-Pb) tunnel junctions when subjected to thermal and voltage annealing. Al-oxide-Pb tunnel junctions were chosen for several reasons: 1) they are the most commonly used type of junction for IETS - the oxide layer being doped with organic molecules, 2) ease of fabrication, and 3) they yield "nice" spectra.

The theory of tunneling, both elastic and inelastic, will be discussed. While the theory allows for the formulation of models which aid in the characterization of some of the changes occurring during annealing, no theory - from the tunneling point of view - has been advanced to really describe the time dependent effects which do occur in tunnel junctions.

Junction preparation and the instrumentation used for measurement of junction properties will be described. Following this, data analysis will be dealt with.

Finally, results of the annealing experiments will be presented along with models and conclusions derived from the experimental information.

Suggestions for further work and appendices will conclude the thesis.

## CHAPTER 2

### THEORETICAL CONSIDERATIONS

#### 2.1. Introduction

The concept of particle tunneling has been in existence almost as long as quantum mechanics itself. A particle, as represented by a wave function, may enter a classically forbidden region and if the potential barrier is sufficiently thin, has a certain probability of tunneling through. That is, according to quantum mechanics, the particle may pass through the barrier without having enough energy to go over the top.

Physically, this concept may be realized in the form of a tunnel junction in which electrons tunnel through an insulating barrier sandwiched between two metal electrodes. Fig. 2.1 shows the basic set-up of a tunneling experiment which allows one to measure the current-voltage characteristic of the junction. What happens if we attempt to pass electrons from one metal electrode to the other? Classically, one simply charges the electrodes as in a capacitor with no current flowing across the insulator. Quantum mechanically, however, one can get a current flow across this region provided that the insulating barrier is thin enough. This is electron tunneling.

In order to understand the tunneling process we start by examining the electron energy level diagram for



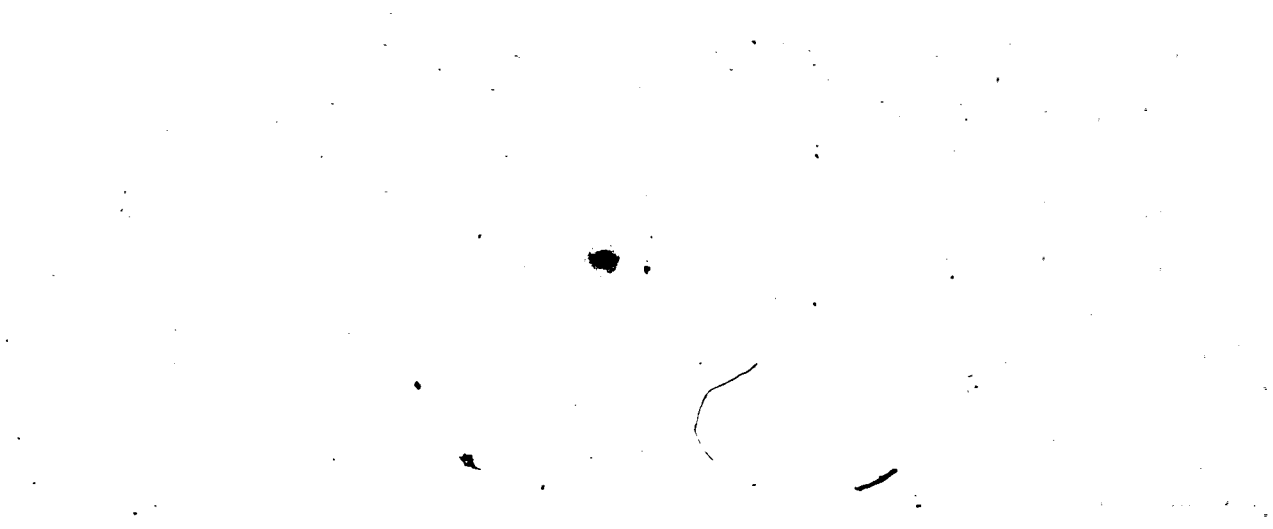
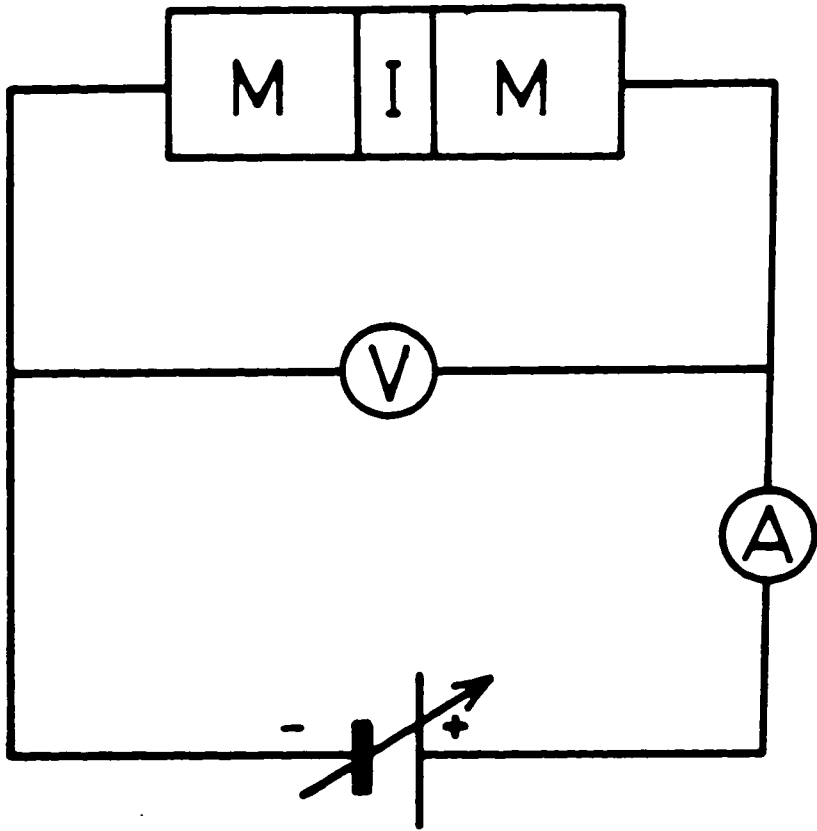


Fig. 2.1

This diagram shows the basic arrangement of a tunneling experiment. M is a metal electrode, I the insulator, V a voltmeter and A an ammeter.



a normal metal-insulator-normal metal junction as shown in Fig. 2.2.  $E_{F1}$  and  $E_{F2}$  are the Fermi energies of metal 1 and metal 2 respectively while  $eV$  is the applied bias energy. Tunneling occurs from left to right (as denoted by the arrow) across a barrier of thickness  $s$  and barrier heights  $\phi_1$  and  $\phi_2$  at the two electrodes.

At  $T = 0K$  all the electron states below  $E_{F1}$  and  $E_{F2}$  are filled, while those above are empty. The application of a voltage  $V$  across the junction (with the left hand metal biased negatively) causes the Fermi levels to become separated by an energy  $eV$ . Filled states of metal 1 are now aligned with available empty states of metal 2 and tunneling of electrons occurs from left to right. Most of this charge transfer occurs elastically (i.e. tunneling without electron energy change) although inelastic effects, which will be discussed later, do occur. As the voltage,  $V$ , is increased, more alignment of filled states with available states occurs and hence, the tunneling current is also increased. Thus, depending on the bias applied to the tunnel junction, one gets a certain current flow across the junction.

## 2.2. Elastic Tunneling

Most of the current flow across the tunnel junction is due to elastic tunneling in which the electron energy does not change when it passes through the barrier. The work of Harrison (59) which deals with tunneling from an


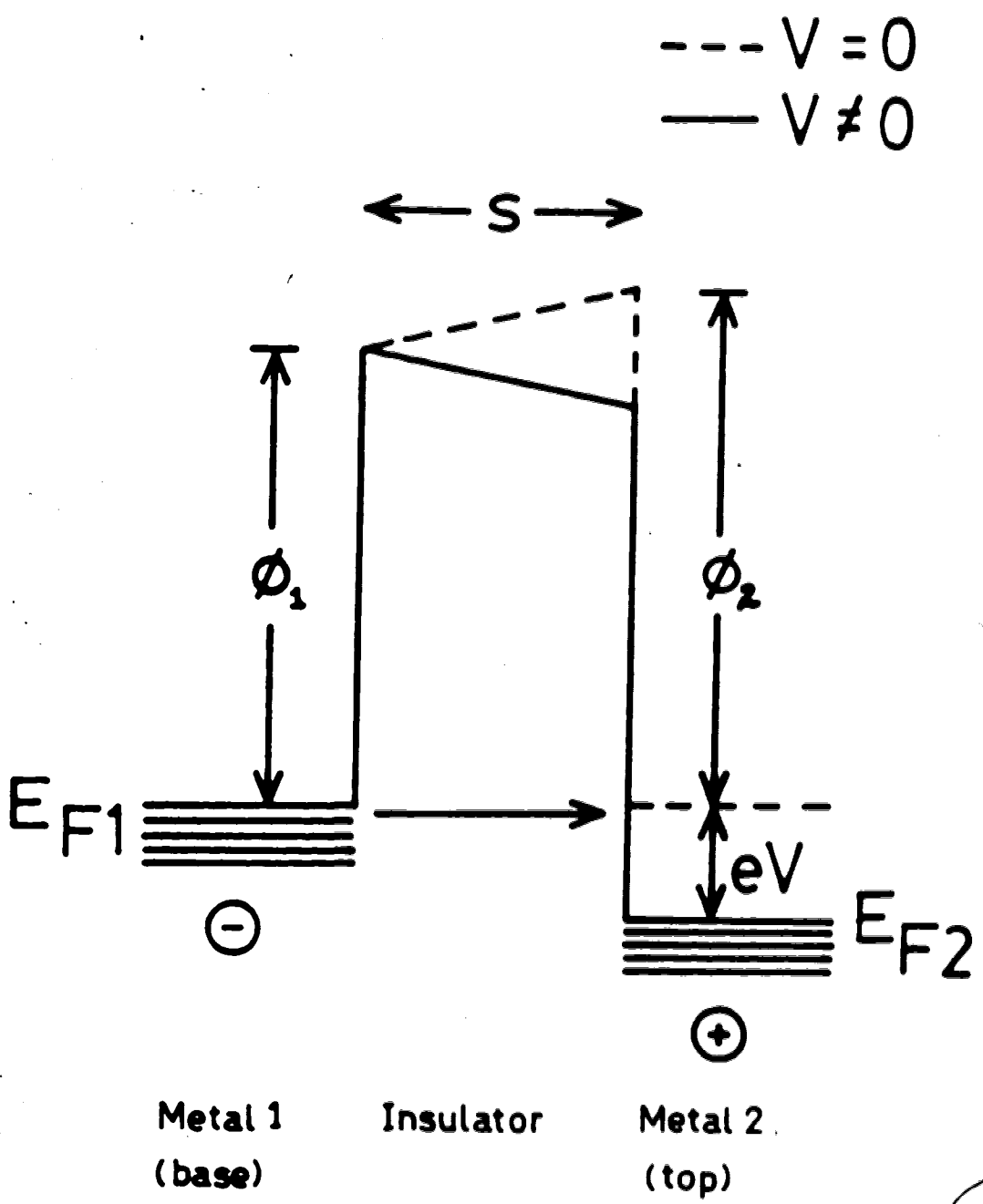


Fig. 2.2

The electron energy level diagram for a metal-insulator-metal junction is shown with and without an applied bias  $V$ . Here,  $s$  is the barrier thickness,  $\phi_1$  and  $\phi_2$  are the barrier heights at the base and top electrodes respectively, and  $E_{F1}$  and  $E_{F2}$  are the Fermi levels of the two metals. When a bias is applied, tunneling occurs in the direction indicated by the arrow.



independent-particle point of view gives a theoretical calculation of the elastic tunneling current which will be briefly shown. Using Bardeen's work (10), the probability per unit time for the transition of an electron from a state a in metal 1 to a state b in metal 2 on the other side of the potential barrier is given by

$$P_{ab} = \left( \frac{2\pi}{\hbar} \right) |M_{ab}|^2 \rho_b f_a (1-f_b) \quad (2.1)$$

where  $M_{ab}$  is the matrix element for the transition,  $\rho_b$  is the density of states at b, and  $f_a$  and  $f_b$  are the probabilities of occupation of states a and b respectively.

Unless the transverse wave number  $k_t$  is the same for the initial and final states the transition matrix element  $M_{ab}$  vanishes and thus  $\rho_b$  is a density of states for fixed  $k_t$ . By summing over all states a of fixed  $k_t$  to obtain  $\rho_a$ , summing over  $k_t$ , multiplying by 2 for spin and by e for electron charge, we obtain the total current from left to right. Subtracting the current in the opposite direction yields the current density

$$j = \frac{4\pi e}{\hbar} \sum_{k_t} \int_{-\infty}^{\infty} |M_{ab}|^2 \rho_a \rho_b (f_a - f_b) dE \quad (2.2)$$

with the integral over energy being taken at fixed transverse wave number.

In the evaluation of matrix elements, states are

constructed which are sinusoidal in a positive-energy region and drop exponentially in the adjacent negative-energy region. Assuming that the band structure is uniform, except near the transition region, and also that the band structure varies only slowly in the transition region allows us to make a WKB approximation. This results in the following expression for the current density

$$j = \frac{2e}{h} \sum_{k_t} \int_{-\infty}^{\infty} \exp \left\{ -2 \int_0^s |k_x| dx \right\} (f_a - f_b) dE \quad (2.3)$$

where  $s$  is the barrier width. We see that the density of states is absent from this expression; this is a consequence of the independent-particle model.

By rewriting the  $k_x$  wavevector within the barrier region as  $k_x = \frac{1}{\hbar} [2m(\phi(x, V) - E_x)]^{1/2}$  and substituting the appropriate Fermi-Dirac distribution functions for  $f_a$  and  $f_b$ , the current density may be written as

$$j = \frac{2e}{h} \sum_{k_t} \int_{-\infty}^{\infty} \exp \left\{ -\frac{2}{\hbar} \int_0^s [2m(\phi(x, V) - E_x)]^{1/2} dx \right\} \times \\ (f(E) - f(E+eV)) dE_x. \quad (2.4)$$

The  $f(E)$  can be expressed as

$$f(E) = \left( e^{(E-\mu)/k_B T} + 1 \right)^{-1}$$

where  $E$  is the total energy for the particular system and

$\mu$  its chemical potential, which at the low temperatures we are dealing with is equal to the Fermi energy.  $E_x$  is the total energy in the direction perpendicular to the potential barrier of thickness  $s$  and barrier height  $\phi(x,V)$  expressed at position  $x$  and applied voltage  $V$ .

Brinkman, Dynes, and Rowell (20) entered into this expression a trapezoidal model for the barrier

$$\phi(x,V) = \phi_1 + (x/s)(\phi_2 - eV - \phi_1)$$

denoting  $\phi_1$  and  $\phi_2$  as the barrier heights at metal 1 and metal 2 respectively with zero applied voltage. By expanding (2.4) in powers of voltage they obtained the following result for the conductance  $\sigma(V)$ . The expression, which is accurate to roughly 10% when the barrier thickness is greater than  $10\text{\AA}$  and  $\Delta\phi/\bar{\phi}$  is less than one, is given by

$$\frac{\sigma(V)}{\sigma(0)} = 1 - \left( \frac{A_0 \Delta\phi}{16\bar{\phi}^{3/2}} \right) eV + \left( \frac{9}{128} \frac{A_0^2}{\bar{\phi}} \right) (eV)^2 \quad (2.5)$$

where  $\Delta\phi = \phi_2 - \phi_1$ ,  $\bar{\phi} = \frac{1}{2}(\phi_1 + \phi_2)$ ,  $A_0 = 4(2m)^{1/2} s/3h$ , and  $\sigma(0) = (3.16 \times 10^{10} \bar{\phi}^{1/2} / s) \exp(-1.025 s \bar{\phi}^{1/2})$ . Expression (2.5) gives a means of obtaining the barrier parameters  $s$ ,  $\bar{\phi}$ , and  $\Delta\phi$  (and hence  $\phi_1$  and  $\phi_2$ ) from experimental data provided one knows the junction conductance with respect to applied voltage.



## CHAPTER 3

### INELASTIC ELECTRON TUNNELING THEORY

#### 3.1. Introduction

Thus far, the tunneling electron has been considered to tunnel across the barrier without any energy change (elastic tunneling), as indeed it would if the barrier were vacuum. But, as the barrier we are dealing with is not vacuum but rather a material insulator, there exists the possibility that a tunneling electron will interact with it in some manner. The questions are: does it, how, and to what extent?

Experimental evidence has shown that the tunneling electron does indeed interact with the barrier and alter its own energy. This occurrence is particularly evident in the derivative of the conductance with respect to voltage, ( $d\sigma/dV$ ) versus  $V$ , the applied bias, which indicates distinctly, changes in the behaviour of the conductance due to processes other than ~~elastic~~ tunneling. These processes alter the conductance by only a few percent at most, indicating that most tunneling still occurs elastically.

The tunneling electron may interact with the barrier in many ways: via phonons, magnons, molecular vibrations, etc. Of interest is the inelastic interaction of the tunneling electrons with molecules in the insulating barrier. Jaklevic and Lambe (62, 82) first saw evidence for this type of interaction when looking at  $d\sigma/dV$  versus

V spectra for chemically doped and undoped Al-Aluminum oxide-Pb tunnel junctions.

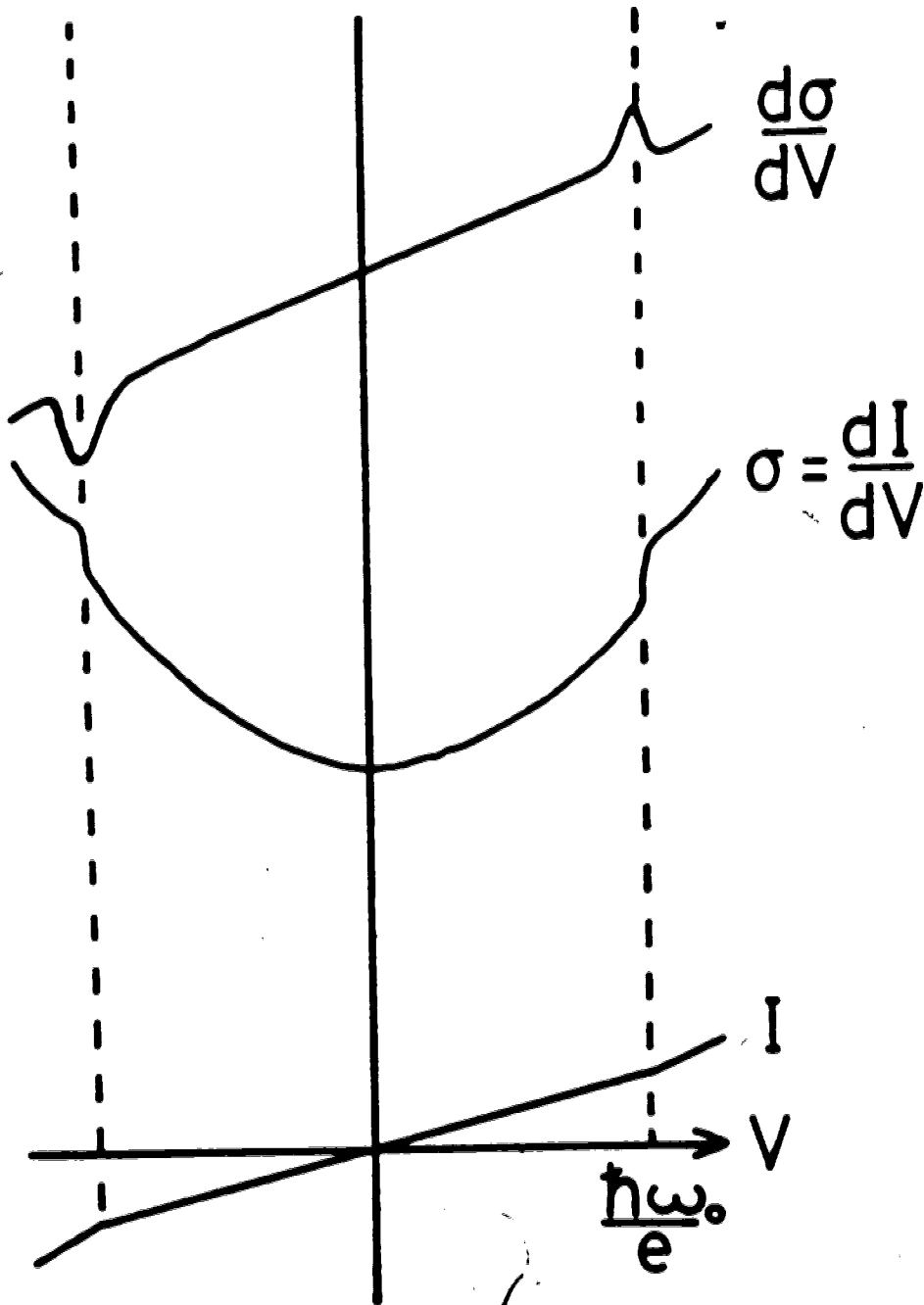
The loss of an amount of energy  $eV_0 = \hbar\omega_0$  to a vibrational mode with frequency  $\omega_0$  of a molecular species in the barrier opens up an additional channel for current flow. This results in a break (change of slope) in the tunnel junction current-voltage (I-V) characteristic, equivalent to a step in conductance versus voltage ( $\sigma$  vs V) or a peak in  $d\sigma/dV$  versus V as shown in Fig. 3.1. Because molecules can have many different vibrational frequencies, and various molecules can exist within the barrier, we will see many peaks in the  $d\sigma/dV$  versus V curve. We call this curve the Inelastic Electron Tunneling (IET) spectrum. Since the energies (0-500 meV) of the vibrational modes we study correspond to infrared frequencies ( $50-4000 \text{ cm}^{-1}$ ), we expect IET spectra to be related to the infrared (IR) and/or Raman spectra for the same molecular species.

### 3.2. Vibrational Spectroscopy

• Part of the information that we gain with Inelastic Electron Tunneling Spectroscopy (IETS) is that of the insulating barrier composition. By noting the energies at which peaks occur in the spectrum, we can, by the use of infrared and Raman data identify the types of molecular groups involved. For example, we may see a peak at 360 meV in our IET spectrum which corresponds to about  $2960 \text{ cm}^{-1}$  (wavenumbers). A table of IR identifications will tell us

Fig. 3.1

Here, an inelastic process for a vibrational mode of frequency  $\omega_0$  results in a break in  $I$  vs  $V$ , a step in  $\sigma$  vs  $V$ , and a peak in  $d\sigma/dV$  vs  $V$ .



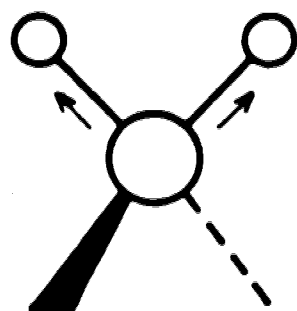
that a vibration of this energy belongs to the stretching mode of a C-H group. Because IR and Raman identifications are important to IETS for the determination of barrier composition, these spectroscopies will be discussed.

First we will consider the nature of molecular vibrations and the vibrational frequencies we expect to observe. There exist two types of molecular vibrations: stretching and bending (or deformation). The stretching vibration entails a rhythmical movement along the bond axis such that the interatomic distance is increasing or decreasing. A bending vibration, on the other hand, might consist of a change in bond angles between bonds with a common atom, or the movement of a group of atoms relative to the remainder of the molecule without motion of the atoms in the group with respect to one another. As examples, twisting, rocking, and torsional vibrations involve changes in bond angles with reference to a coordinate system arbitrarily set up within the molecules. Fig. 3.2 illustrates various types of vibrations.

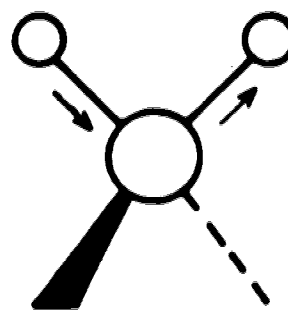
In the case of stretching frequencies, assignments can be approximated by using Hooke's law. In applying this law, two atoms and their connecting bond are treated as a simple harmonic oscillator composed of two masses joined by a spring. The relationship between the frequency of oscillation, atomic masses and the force constant of the bond is given by the following equation, derived from Hooke's law,

Fig. 3.2

Vibrations for a group of atoms ( $\odot$  and  $\ominus$  indicate motion perpendicular to the plane of the page).

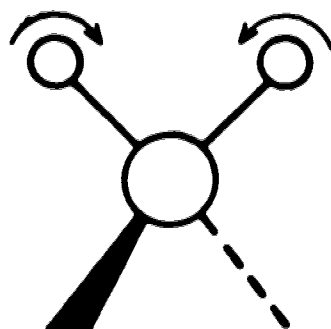


Symmetric

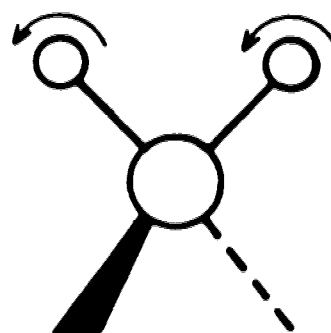


Asymmetric

## Stretching Vibrations

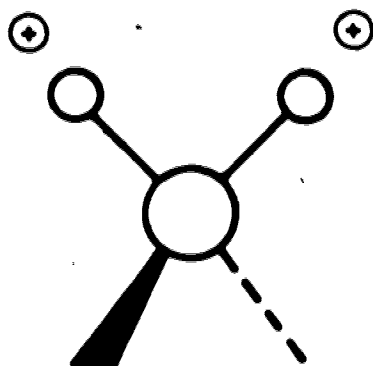


Scissoring

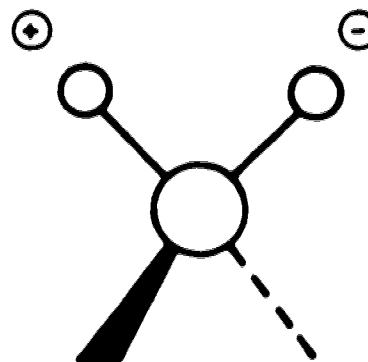


Rocking

## In-Plane Bending Vibrations



Wagging



Twisting

## Out-Of-Plane Bending Vibrations

$$\nu = \frac{1}{2\pi c} \left( f / \left( \frac{M_x M_y}{M_x + M_y} \right) \right)^{1/2} \quad (3.1)$$

where  $\nu$  is the vibrational frequency ( $\text{cm}^{-1}$ ),  $c$  is the velocity of light ( $\text{cm}/\text{sec}$ ),  $f$  is the force constant of the bond ( $\text{dynes}/\text{cm}$ ), and  $M_x$  and  $M_y$  are the masses of atoms  $x$  and  $y$ , respectively ( $g$ ). For single bonds,  $f$  is approximately  $5 \times 10^5$   $\text{dynes}/\text{cm}$ , while for double and triple bonds it is about two and three times this value. It should be noted that the frequency is expressed as  $\nu = f/c$  ( $f$  has units of  $\text{sec}^{-1}$ ) and thus has units of  $\text{cm}^{-1}$  (called wave-numbers) instead of  $\text{sec}^{-1}$ .

Applying (3.1) to C-H stretching, using  $19.8 \times 10^{-24}$   $g$  and  $1.64 \times 10^{-24}$   $g$  as mass values for C and H respectively, and  $5 \times 10^5$   $\text{dynes}/\text{cm}$  for the single bond, yields a value of  $3040 \text{ cm}^{-1}$  for the frequency of this C-H bond vibration. In actual practice, however, C-H stretching vibrations, associated with methyl ( $-\text{CH}_3$ ) and methylene ( $-\text{CH}_2-$ ) groups, are generally observed in the region between  $2850$ - $2960 \text{ cm}^{-1}$ . The calculation is not precise since effects arising from the environment of the C-H group within a molecule have not been accounted for. One often uses the frequency of infrared absorption to calculate the force constants of bonds.

To use Hooke's law for the calculation of vibrational frequencies of bond stretching, one must consider the relative contributions of bond strengths and atomic



masses. For example, a comparison of the C-H group with the F-H group, based on atomic masses, leads to the conclusion that the stretching frequency for the F-H bond occurs at a lower frequency than that of the C-H bond. The reverse is true. This is because the increase in the force constant from left to right across the first two rows of the periodic table has a greater effect than the mass increase. Hence, the F-H group has a higher vibrational frequency ( $4138 \text{ cm}^{-1}$ ) than does the C-H group ( $3040 \text{ cm}^{-1}$ ).

One way to study these vibrational modes is by passing infrared radiation through a sample of molecules and observing the frequencies at which the radiation is absorbed. This is called infrared spectroscopy.

If a molecule is to absorb infrared radiation, the radiation incident on the molecule must first be of the correct frequency to cause a quantum jump in its vibrational energy. Secondly, the vibrating molecule will interact with the oscillating electric field of incident electromagnetic radiation if an oscillating dipole moment accompanies the vibration. Such a change in dipole moment occurs for a molecule whenever a change in position of the centers of positive and negative charge resulting from atomic motion takes place. When all this happens, energy is absorbed and the amplitude of the particular vibration is increased. The absorbed energy is subsequently released

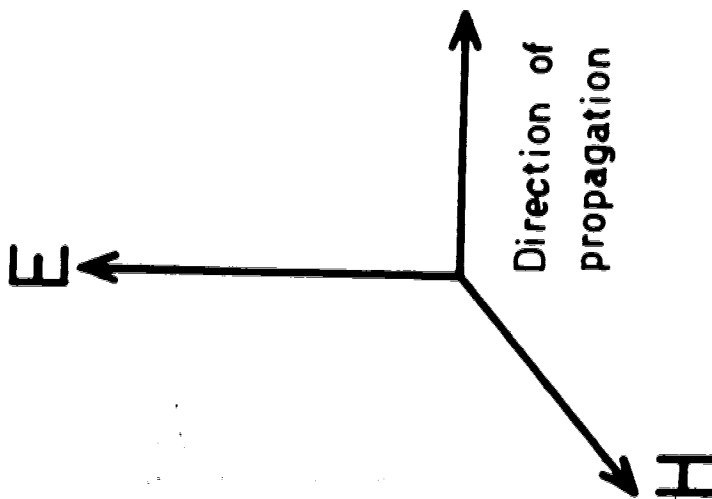
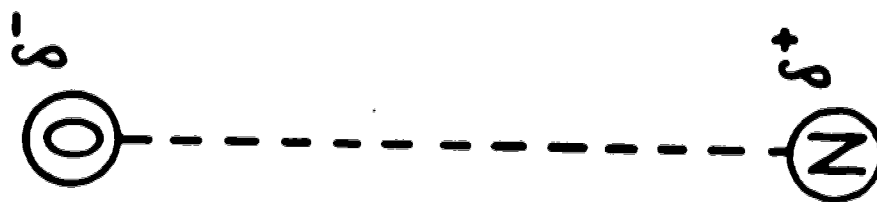
as heat as the molecule reverts from the excited state back to the original ground state.

One can use a simple explanation (119) as illustrated in Fig.3.3 to show how electromagnetic radiation can excite vibrational motion in a molecule. First, consider the  $N_2$  molecule which due to charge symmetry has no permanent dipole moment; it can be assumed that equal positive and negative charges are present on each nitrogen atom. Now, the electric field of incident electromagnetic radiation will cause positive charges to move in one direction and negative charges in the other. This type of interaction, for a symmetric molecule as  $N_2$ , produces no vibrational motion. On the other hand with an asymmetric molecule, such as NO, where the negative charge on the oxygen atom is greater than that on the nitrogen atom, electromagnetic radiation of the proper frequency (i.e. the frequency of the electromagnetic wave's oscillatory electric field matches the frequency of the particular molecular vibration) can produce a stretching of the bond between the atoms as the negative charge on the oxygen atom moves in an opposite direction to that of the positive charge on the nitrogen atom. This sort of interaction results in an enhanced stretching (resonance) of the bond between the nitrogen and the oxygen, and



Fig. 3.3

Interaction of electromagnetic energy with  $N_2$  and  
NO molecules.



consequently, the absorption of infrared radiation.

Thus, a variation in the dipole moment,  $\mu$ , accompanying atomic motion similar to that just described for NO allows the vibrational mode to become excited and to absorb infrared radiation; such a mode is then said to be "infrared active". The intensity of the absorption process is found to be greater for increased values of the change in dipole moment during a vibration. Quantitatively, the integrated absorption intensity for a particular infrared vibrational band may be expressed as

$$A = \frac{N}{3c^2} \left( \frac{\delta\mu}{\delta Q} \right)^2$$

where  $N$  is a constant,  $c$  is the velocity of light,  $\mu$  is the dipole moment and  $Q$  the normal coordinate associated with the vibrational mode. For example, the stretching vibration of a diatomic molecule has a normal coordinate proportional to  $r - r_e$ , where  $r_e$  is the equilibrium internuclear distance and  $r$  is the displaced value during the stretching motion. One can see that the larger the change of dipole moment with respect to position during vibration, the greater will be the intensity of infrared absorption.

We now turn to the Raman effect which can give information about vibrational modes lacking an oscillating dipole moment and hence complements infrared absorption data. When an electromagnetic wave passes through a

transparent material, a certain portion of the radiation is scattered by the molecules of the transmitting medium. The bulk of the scattered radiation has the same frequency as the incident radiation, in which case the phenomenon is called Rayleigh scattering. The magnitude of this scattering is proportional to the fourth power of the frequency, therefore radiation at the blue end of the visible spectrum is scattered more strongly than that at the red end. This fact, taken together with the spectral emission curve of the sun, and the human eye's wavelength dependent sensitivity, explains the blue color of the sky.

In addition to Rayleigh scattering, molecules in the medium can lose energy to or gain energy from the penetrating electromagnetic wave. The energy changes arise from specific transitions between states of the molecules, the excitation of a vibrational mode from the ground state to an excited state being an example. This is the Raman effect and it occurs as the result of the interaction between the optical electric field and the polarizability of the molecule.

To use this technique, one irradiates a sample with an intense monochromatic beam (e.g. laser light), usually of wavelength 4000-7000 Å (visible light). Photons of the beam may collide and interact with molecules of the sample, and in the process transmit energy to or acquire energy from the system (via inelastic collisions).

These inelastic collisions result in a modification of the photon energy to

$$h\nu_f = h(\nu_0 \pm \nu_i)$$

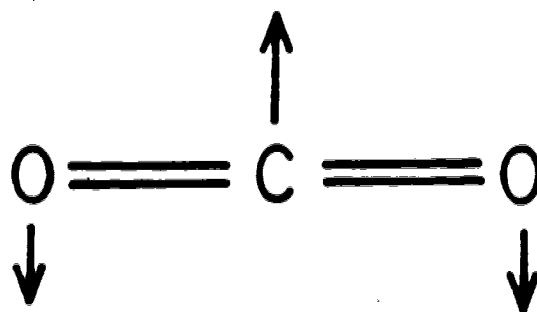
where  $\nu_0$  is the incident light frequency, and  $\pm h\nu_i$  is the energy change in the system where  $\nu_i$  may be the frequency of a vibrational mode. Generally, the total Raman modulated radiation (at frequencies  $\nu_0 \pm \nu_i$ ) is about 1% of the Rayleigh scattering (occurring at  $\nu_0$ ). Also, since the vibrational modes of a molecule are more likely to be in a ground state rather than an excited state at usual temperatures (as determined by the Boltzmann distribution) scattering involving energy changes  $h(\nu_0 - \nu_i)$  is more intense than that for  $h(\nu_0 + \nu_i)$ . In other words, the photon tends to lose energy to a molecule rather than gaining energy. In fact for  $\nu_i$  above  $700 \text{ cm}^{-1}$ , scattering corresponding to the energy change  $h(\nu_0 + \nu_i)$  is hardly ever observed.

As an example of how infrared and Raman spectroscopy complement each other, consider the  $\text{CO}_2$  molecule shown in Fig. 3.4. The mode shown in 3.4(a) gives rise to an oscillating dipole, and will thus be infrared-active but not Raman-active. The mode in 3.4(b), however, is Raman-active, since  $\alpha$ , the polarizability can change linearly with the displacement of the oxygens. Since 3.4(b) does not give rise to an oscillating dipole, it is

Fig. 3.4

Illustrated are two vibrational modes of the  $\text{CO}_2$  molecule. The scissoring (bending) mode in (a) is IR-active and the symmetrical stretching mode in (b) is Raman-active.





(a)



(b)

not infrared-active.

### 3.3. Simple Models for Inelastic Electron Tunneling

Having looked at infrared and Raman spectroscopy as a means of determining vibrational spectra, we now return to inelastic electron tunneling. It has been found that when a tunneling electron has sufficient energy  $eV \geq \hbar\omega_0$ , it may excite a vibrational mode (with angular frequency  $\omega_0$ ) of a molecule in the barrier. Also, since the tunneling electron can couple to the dipole moment or to the polarizability of the molecule, one may observe both infrared-active and Raman-active modes in the IET spectrum. The mechanism involved in the interaction is similar to that for infrared and Raman excitations (67). In the infrared case one views the dipole moment of a polar molecule as having several components - one along each bond. These dipoles interact with the transverse electric field of the infrared radiation and can absorb a quantum of incident radiation if the frequency is correct. In inelastic electron tunneling it is the longitudinal electric field of the electron which interacts with a dipole moment, and it is the electron which gives up the necessary energy ( $E = \hbar\omega_0$ ,  $\omega_0$  is the frequency to be excited) to excite the molecule. For the Raman case, the polarizability components of molecules are involved. The induced dipole moment due to polarizability interacts with the transverse electric field of the incident radiation

(UV or visible) to produce an excited state. Likewise in inelastic electron tunneling the electron's longitudinal electric field interacting with an induced dipole moment can excite the molecule to a higher vibrational state upon absorbing energy from the electron. Thus, the tunneling electron can excite both infrared- and Raman-like excitations.

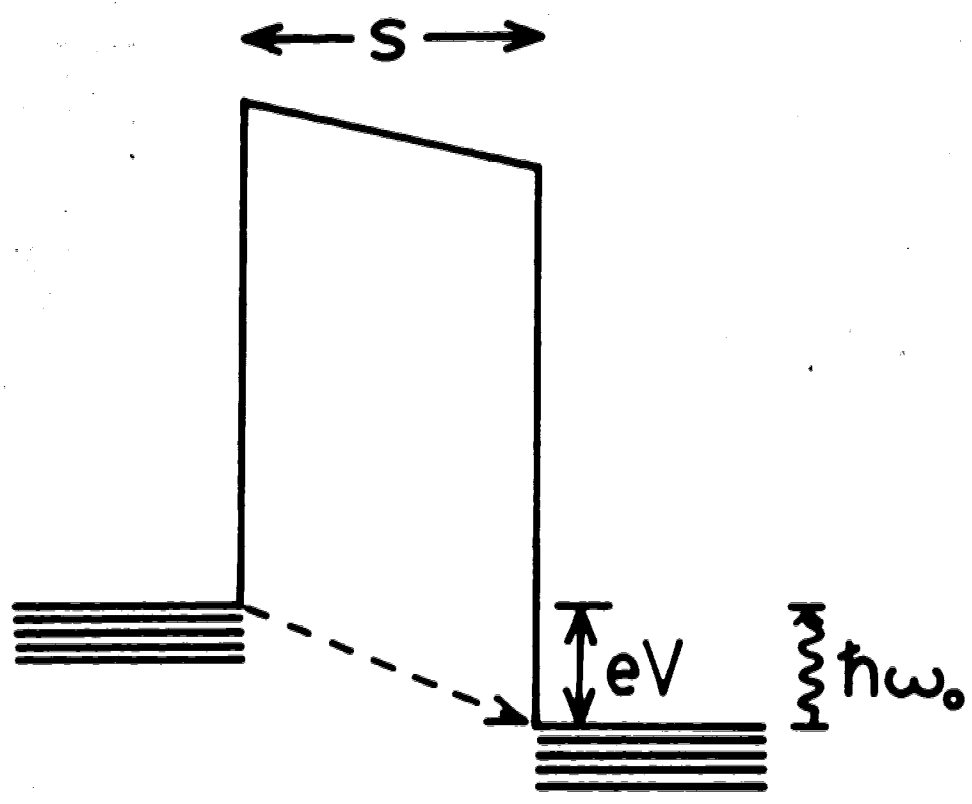
The energy level diagram for such an occurrence is represented in Fig. 3.5. This figure shows the excitation of a vibrational mode by an electron having the threshold energy  $eV = \hbar\omega_0$ . As the electron energy  $eV$  is increased, the excitation will still occur but will leave the electron some energy. At the temperatures of interest (i.e. 4.2 K) one can assume that all molecules are in their ground states and thus, only processes in which the electron gives up energy to excite a vibrational mode will occur - the electron will not receive energy from a vibrational mode.

The first explanation for the interaction of a tunneling electron with a molecular vibrational mode was given by Scalapino and Marcus (110). This was given in terms of a simple one-electron picture in which the tunneling electron interacted with the dipole field (plus its image) of a molecular group in the insulator, near to the insulator-metal interface.

Taking into account the nearest image of the dipole, the electron-dipole interaction energy is, using

Fig. 3.5

An electron energy level diagram for inelastic electron tunneling is shown. Here, a vibrational mode of frequency  $\omega_0$  is excited by an electron with threshold energy  $eV = \hbar\omega_0$ .



Metal 1

Insulator

Metal 2

the dipole approximation,

$$U_d = \frac{2\exp_x}{(x^2 + r_\perp^2)^{3/2}} \quad (3.2)$$

where  $x$  is the distance from the metal-insulator interface normal to the metal electrode to the tunneling electron,  $r_\perp$  is the component of distance between the electron and the dipole perpendicular to the electron's motion (i.e. the distance component parallel to the interface),  $p_x$  is the component of the dipole moment normal to the electrode, and  $e$  is the electron charge. Using a WKB approximation for the tunneling matrix element, some other approximations followed by the use of the "Golden Rule", and more approximations we get a value for the second derivative of current with respect to voltage due to the inelastic current as

$$\frac{d^2 I}{dV^2} = n \frac{4\pi e^2 m}{\phi} \ln \left| \frac{s}{r_0} \right| \left( \frac{dI}{dV} \right)_0 \sum_m | \langle m | p_x | 0 \rangle |^2 \delta(V - \omega_{m0}). \quad (3.3)$$

Integrating (3.3) over a voltage increment of a vibrational band yields an intensity or conductance change as

$$n \left( \frac{dI}{dV} \right)_0 \ln \left| \frac{s}{r_0} \right| \frac{4\pi e^2 m}{\phi} \frac{e^2 f_\nu}{2m\omega_\nu} A, \quad (3.4)$$

where  $A = \sin^2 \theta$  for a bending mode or  $A = \cos^2 \theta$  for a stretching mode. Here  $\omega_\nu$  and  $f_\nu$  are the frequency and oscillator strength of the  $\nu$ th band,  $\theta$  is the angle between the dipole and the normal to the surface,  $s$  is the thickness

of the insulating layer,  $n$  is the number of dipoles per unit area,  $\phi = U - \epsilon_F$  ( $\epsilon_F$  is the electron energy set to its value at the Fermi surface and  $U$  is the effective insulator potential ignoring the contribution of the molecular dipoles),  $r_0$  is a cutoff in the vicinity of the dipole where the approximation for the potential begins to fail - since  $r_0$  enters into a logarithm, its exact magnitude is not critical, and finally  $(dI/dV)_0$  is a zero bias conductance. Considering a hydroxyl group as the molecular dipole, and  $n$  as 10 OH groups per  $100 \text{ \AA}^2$ , for the bending mode  $\omega_v \sim 0.11 \text{ eV}$  and  $f_v \sim 10^{-5}$ . Taking  $s/r_0 = 30$ ,  $\phi = 2 \text{ eV}$ , and  $\sin^2 \theta = 1/2$  the use of Eq. (3.3) gives a conductance change on the order of 1% consistent with experimentally reported results.

Soon after, Jaklevic and Lambe (63, 82) generalized these results to include the interaction of the tunneling electron with the polarizability of the molecule. With the electron able to induce a dipole moment in the molecular species of value  $p = \alpha E$  ( $\alpha$  varying with molecular vibration), and taking into account nearest images, the interaction energy is

$$U_p = \frac{-4e^2 \alpha z^2}{(z^2 + r_0^2)^3} \quad (3.5)$$

Using similar approximation to those of Scalapino and Marcus, a value for the inelastic contribution is arrived at

$$\frac{d^2 I}{dV^2} = N \left( \frac{dI}{dV} \right)_0 B \sum_m |\langle m | \alpha | 0 \rangle|^2 \delta(eV - \hbar\omega_m) \quad (3.6)$$

where  $N$  is the total number molecules,  $B$  is a constant, and  $(dI/dV)_0$  the zero bias conductance. Integrating to obtain the intensity or conductance change one arrives at

$$N \left( \frac{dI}{dV} \right)_0 B \sum_m |\langle m | \alpha | 0 \rangle|^2 \quad (3.7)$$

with  $\sum_m |\langle m | \alpha | 0 \rangle|^2$  directly proportional to the intensity of scattered light as in the Raman effect. Using  $\sum_m |\langle m | \alpha | 0 \rangle|^2 \approx 10^{-50} \text{ cm}^6$  (from optical Raman data) one gets a conductance change of (0.1-0.5)% as compared to 1% for the dipole interaction described previously.

Jaklevic and Lambe also consider the resolution of peaks in the IET spectrum, the overall linewidths of which are determined by natural widths of molecular excitation lines, temperature broadening, and density of states due to the metal electrodes (such as superconductors). For normal metals, one may express the peak shape in the IET spectrum of a single sharp molecular excitation that is thermally broadened as

$$\frac{d^2 I}{dV^2} = c \left( \frac{e^2}{kT} \right) \left[ e^u \frac{(u-2)e^u + (u+2)}{(e^u - 1)^3} \right], \quad u \equiv \frac{eV - \hbar\omega_0}{kT}, \quad (3.8)$$

where  $T$  is the temperature and  $\omega_0$  the angular frequency of the molecular excitation. This equation describes a



symmetrical bell-shaped peak of width  $5.4 kT$ , the height of which is proportional to  $(kT)^{-1}$ , and the total area (intensity) of which is independent of temperature. At room temperature, in agreement with experiment, the broadening is so great - a peak width of 150 meV for modes occurring in a 0-500 meV range - that peak observation is practically impossible. For this reason IET spectra are taken at low temperatures, such as liquid helium temperature of 4.2 K, where the broadening is only about 2 meV.

The other mentioned factor of importance in resolution is the use of superconducting electrodes. In this case, one must consider the superconducting density of states. Doing this, one finds that the IET peak sharpens up, and also for a peak with a sharp natural linewidth an "undershoot" is observed on the high energy side of the peak (74, 82, 93). Finally, it should be noted that the energy at which a peak occurs is shifted from  $\hbar\omega_0$  to  $(\hbar\omega_0 + 2\Delta)$  when two identical superconducting electrodes are used, where  $2\Delta$  is the temperature dependent magnitude of the superconducting energy gap.

#### 3.4. More Complex Models for Inelastic Electron Tunneling

After the initial works of Scalapino and Marcus, and Jaklevic and Lambe, more complex theoretical treatments of inelastic tunneling began to appear in the literature. Bennett et al. (13), and Duke (39) considered inelastic electron tunneling using the transfer Hamiltonian

formalism. In this formulation, each metal electrode is considered separately, with each described by a distinct many-body Hamiltonian, the eigenfunctions of which are supposedly known. A third term, known as the transfer Hamiltonian, is then added to describe the interaction of the tunneling electrons with the molecules or impurities composing the barrier. The total Hamiltonian may be written as

$$H = H_L + H_R + H_T$$

with terms for the left- and right-hand electrons as well as the "transfer" term. One then views the inelastic tunneling process as a transition from a state at one metal electrode to another state on the other side via interaction with barrier molecules. For the case of molecular vibrations, the dipole or polarizability potentials previously described may be incorporated into the transfer Hamiltonian term, the predicted results being in approximate agreement with experimental observations.

Considering the previous approaches to be unnecessarily approximate in nature, Brailsford and Davis (19) proposed a stationary-state formulation of the problem in which the entire noninteracting one-electron system, consisting of an arbitrary interaction potential (molecular vibrator, etc.) and a square-barrier potential is considered. They consider in detail the special case

of a one dimensional square barrier with the vibrator interaction within the barrier. In the limit of the first Born approximation, the eigenfunctions of the metal-insulator-metal system are derived. Since Fermi statistics play an important role in the inelastic tunneling process, Davis (33) subsequently extended the results to a many-electron system. His theory was formally derived for an arbitrary tunneling barrier with an arbitrary interaction potential between the electrons and a vibrator (e.g. molecular impurity, phonon, etc.). The results for the inelastic current indicated agreement with the transfer Hamiltonian method. In addition, for molecular impurities sufficiently close to the barrier boundary, the shape of peaks in the IET spectrum are predicted to be fundamentally different from those of molecules further inside the barrier. For molecules very close to the interface, one would see an "anti-peak" or a dip in  $d^2I/dV^2$  versus  $V$ .

Schattke and Birkner (16, 112) proposed an alternate theoretical approach to explain inelastic electron tunneling which, like Davis does not employ the transfer Hamiltonian approach. Whereas the calculations of Davis are restricted to  $T = 0K$ , and complications can arise in the case of many-body interactions for  $T > 0K$ , the model of Schattke and Birkner attempts to avoid these difficulties. Their results also predict the same type of lineshapes in the IET spectrum for a molecular impurity close to the boundary of the barrier, as did Davis.

However, they see even more; a distinct asymmetry in peak shape and size is predicted for opposite voltage polarities. Although dips or "anti-peaks" have not been confirmed in IET spectroscopy, asymmetry in the "usual" peak sizes for opposite polarities has been observed (75, 129).

Other approaches to the tunneling problem have been devised by Caroli et al. (23, 24, 25, 26), Combescot et al. (30, 31), and Feuchtwang (46); however, their results are not directly applicable to experimental verification.

### 3.5. Transfer Hamiltonians since 1976

In 1976 Kirtley, Scalapino, and Hansma (70) revived the transfer Hamiltonian formalism to develop a theory for the intensities of vibrational modes in the inelastic electron tunneling spectroscopy of organic molecules in metal-insulator-metal tunnel junctions. At the outset, they bypass the use of a dipole approximation for the tunneling electron-molecular interaction, and assume instead that the charge distribution within the molecule can be broken up into partial charges, with each partial charge localized on a particular atom. These partial charges originate from the uneven sharing of bonding electrons and can be obtained from the dipole derivatives of infrared theory. The partial charge analysis allows for the description of the interaction at distances comparable to interatomic lengths within which the dipole approximation breaks down. One can write the total

tunneling electron-molecular interaction as

$$V(\vec{r}) = \sum_j \frac{-e^2 z_j}{|\vec{r} - \vec{R}_j|} \quad (3.9)$$

where  $e z_j$  and  $R_j$  are the partial charge and position, respectively, of the  $j$ th atom.

The inelastic tunneling matrix element,  $M_{KK'}$ , is then calculated using WKB wave functions for the incoming and outgoing states,  $K$  and  $K'$ . The scattering process is treated in three dimensions and it can be shown that the inclusion of off-axis scattering results in conclusions different not only quantitatively but also qualitatively from purely one-dimensional calculations. Since the electron-molecule interaction is used as a first-order perturbation on WKB-approximation wave functions, the distortion of the incoming and outgoing wavefunctions due to the molecular impurity cannot be taken into account. However, the relatively-long-range structure of the interaction decreases the importance of this distortion for vibrational-mode couplings.

The final expression obtained for the second derivative of current with respect to electron energy is given as

$$\begin{aligned} \frac{d^2 i}{d(eV)^2} = & \frac{8\pi n e}{\hbar} \left(\frac{L}{\pi}\right)^6 \left(\frac{m}{\hbar^2}\right)^3 (\epsilon_F)^{\frac{1}{2}} (\epsilon'_F - eV)^{\frac{1}{2}} \int_0^{2\pi} d\phi \int_0^{2\pi} d\phi' \\ & \times \int_0^1 d(\cos\theta) \int_0^1 d(\cos\theta') |M_{KK'}|^2 \delta(\hbar\omega - eV). \end{aligned} \quad (3.10)$$

Here,  $i$  is the current per unit area through the junction,  $n$  is the surface density per unit area of organic molecules,  $\epsilon_F(\epsilon_{F'})$  is the Fermi energy in the initial (final) electrode,  $V$  is the voltage bias of the junction,  $\hbar\omega$  is the energy of the vibrational mode of interest, and  $L$  is an arbitrary normalization length. Also, it is assumed that the vibrational mode has a  $\delta$ -function response in frequency to the tunneling electron excitation. The results obtained for the peak intensity or change in conductance (obtained by numerical integration of Eq. (3.10)) due to inelastic tunneling are in good agreement with experimentally observed results. One may also predict ratios of peak intensities for peaks at opposite bias polarity.

The theory of Scalapino and Marcus (110) predicted that there would be no IETS intensity for a vibrational mode which gave rise to an oscillating dipole moment parallel to the metal electrode surface. Off-axis scattering weakens this orientation rule somewhat. A numerical calculation based on Eq. (3.10) for the hydroxide ion predicts that the IETS peak intensity for the OH stretch mode should be 8.8 times stronger when the molecule is oriented perpendicular to the metal electrode surface than when it is oriented parallel to the metal surface. A similar calculation for the infrared-active mode of  $\text{CO}_2$  predicts the ratio of intensities for the two orientations as 16.4. Thus, although the theory predicts a general weakening, the selection rule is still quite strong.

Finally, it should be noted that the above theoretical formulation does not take into account the polarizability of the molecule. The extra interaction due to polarizability may be great enough to be of importance and should be calculated.

The above work calculated the contribution to IETS intensities due to a model potential essentially long range in nature. A later work by Kirtley and Soven (72) presents calculations of contributions to the intensities due to the short range part of the molecular potential. In this, the scattering molecular potential is calculated using the  $X\alpha$  approximation to the exchange correlation potential, and the transfer Hamiltonian approach is used to calculate inelastic electron tunneling cross sections.

It is found that predicted short range cross sections are strongly energy dependent and could be quite large for tunneling electrons at a molecular bound state energy. A comparison, however, of long range and short range model predictions for higher harmonic amplitudes and opposite bias voltage peak intensity asymmetries indicate that the long range interactions dominate in IETS. As an example, they consider an Al-AlO<sub>x</sub>-Rh-CO-Pb tunnel junction in which the CO molecule is localized near the Pb electrode. The intensity of the CO stretch mode is smaller for Al biased positive than for Al biased negative, the ratio being  $\sim 0.68$ . For Al negative, the electron tunnels through the oxide before losing energy to the CO but for

At positive bias the electron loses energy first and then has to tunnel. The asymmetry results since electrons with diminished energy are less likely to penetrate the barrier (75, 129). The short range interaction might be expected to predict a large asymmetry, since the interaction is localized close to one electrode, while a long range interaction would give less asymmetry. This is just what happens: the current short range model calculation described here predicts an asymmetry ratio of 0.23 while the previous long range theory of Kirtley, Scalapino, and Hansma gives 0.59, in better agreement with the experimental value of 0.68. The experimental observations thus indicate that long range interactions dominate in IETS.

Further work using the transfer Hamiltonian method for inelastic electron tunneling deals with the orientation of adsorbed molecules on a surface. In particular, Kirtley and Hall (73) used a dipole-potential in a transfer Hamiltonian theory of intensities to study the tunneling spectrum of methanesulfonate ( $\text{CH}_3\text{SO}_3^-$ ) chemisorbed on alumina. Comparison of theoretical predictions with experiment supports an orientation of methanesulfonate adsorbed on alumina such that the C-S bond is perpendicular to the surface. Also, dipole derivatives generated from tunneling spectrum intensities compare well with those obtained from infrared measurements for similar species.

In this first attempt to unravel the information



contained in all the intensities of the spectrum of a simple molecule, Kirtley and Hall attempted to compare the dipole derivatives of ethane and propane to  $\text{CH}_3\text{SO}_3^-$ . They found quite good agreement considering the following problems: (1) different molecules in different environments are compared, (2) polarizability interactions are ignored in the theory, and (3) positions of dipoles in the molecule may be different from those assumed.

## CHAPTER 4

### EXPERIMENTAL TECHNIQUES

#### 4.1. Junction Preparation

Tunnel junctions were formed by first evaporating a set of circular indium contacts onto a clean glass substrate (see Fig. 4.1). Following this, an aluminum base film (2000 Å thick) was evaporated, and then oxidized in an oxygen-helium plasma discharge to grow an aluminum oxide (alumina) insulating layer. Fabrication was then completed by evaporating two desired top metal electrodes (2000 Å thick).

The substrate was prepared by cutting a piece of pyrex microscope slide 1×1 cm square, scrubbing with detergent (Alconox), rinsing with copious amounts of hot water followed briefly by methanol to quickly remove water. Visual inspection of the substrate for freedom from dirt and small specks of material followed. A clean substrate was then flame polished over a bunsen burner for two to three minutes until the corners started to melt and a slight yellowish tinge appeared in the glass. It was then placed in a substrate holder within the evaporator system.

Various metals and types of evaporation filaments were used as shown in Table 4.1. The metals were loaded onto the filaments directly except for the aluminum and copper wires. These were first cleaned with a methanol rinse and wiped dry with kimwipe tissues. The copper wire

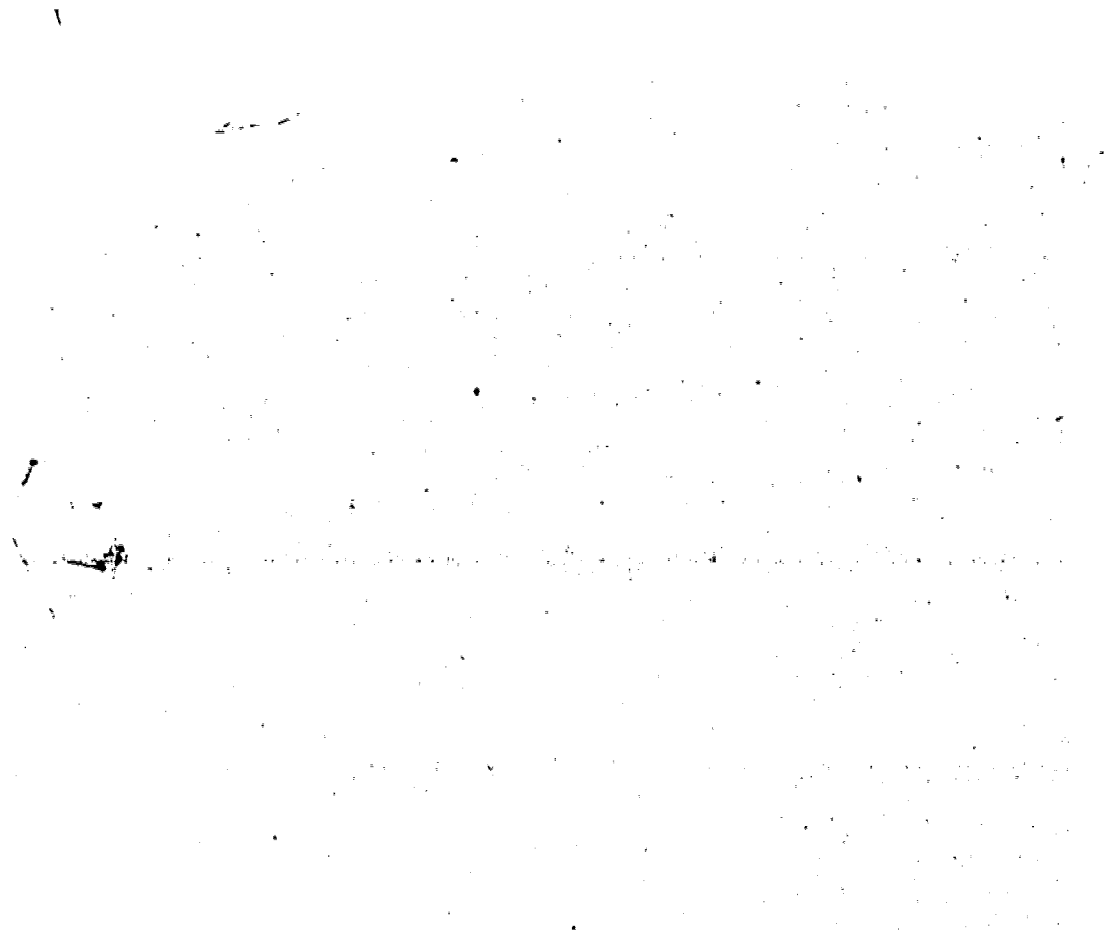


Fig. 4.1

Tunnel junction layout.

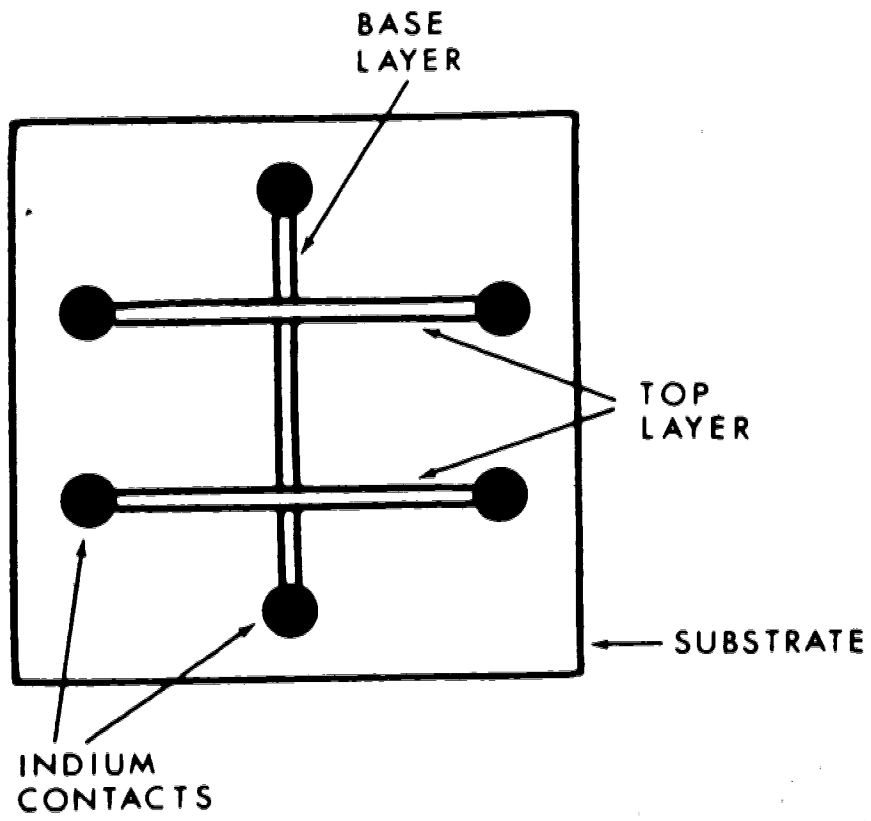


Table 4.1  
Evaporation Materials

Metal	Purity	Supplier	Evaporation Source
Al	59	A.D. Mackay	F6-4X.030 W coil
Ag	69	Cominco	S39-.005 Ta boat
Au	69	Cominco	S39-.005 Mo S9A-.005 W boat
Cu		electrolytic tough pitch wire	S39-.005 Ta boat
In	69	Cominco	S39-.005 Mo boat
Mg	59	Johnson Matthey	S17B-.005 Ta covered boat
Pb	69	Cominco	S39-.005 Mo boat
Sn	59	Cominco	S39-.005 Mo S39-.005 Ta

Evaporation sources supplied by R.D. Mathis Company.

(2 mm diameter) was then cut into ~ 4 mm pieces and loaded onto a boat filament. The aluminum wire was cut into longer pieces which were then bent into the shape of staples and loaded onto a helical tungsten filament.

Resistive heating of a filament evaporated metal onto a substrate into a film shape determined by a mask placed right beneath the substrate. The different filaments, which were mounted on a carousel that could be rotated with respect to any particular substrate, had cylindrical glass chimneys placed around them to prevent mutual cross-contamination of metals during evaporation. It should be noted that the substrate holder could be rotated if desired and could also be moved upward or downward.

Once the metals were loaded and the desired masks were chosen for junction preparation, the evaporator system vacuum chamber (enclosed in an 18 inch bell jar) was pumped out by a mechanical pump. The lower pressures ( $\sim 10^{-5}$  torr) used during actual metal evaporation were achieved using an oil diffusion pump with a liquid nitrogen cold trap backed by the above mentioned mechanical pump. During the initial pumping down procedure, the lines of the manifold allowing for the controlled entry of gases into the vacuum chamber, were flushed several times with new gas.

Some pure oxygen was then let into the bell jar to a pressure of 200 microns, and a plasma discharge with a current of ~ 11mA and a voltage of ~ 420 V was run for

5 minutes. To create the plasma, two circular concentric copper electrodes were used, the outer one being a circular band of copper sheet and the inner one a circular piece of copper rod. The voltage was applied such that the outer electrode was positive and the inner one negative. This five minute oxygen discharge was the first part of a "cleaning" procedure for the system which had been exposed to room atmosphere. Oxygen, being reactive is expected to combine with stray contaminant molecules which could subsequently be pumped out of the system. Following the oxygen discharge a longer discharge with argon gas was carried out for ~ 15 minutes with ~ 150 microns pressure, and 11 mA current with ~ 400 volts. The purpose of this was to clean the system by using the relatively large argon atoms to dislodge any "dirt" atoms or molecules adhering to various parts of the evaporator system within the vacuum chamber. The effectiveness of this was reflected by increases in gas pressure (above 150 microns) and in current during the course of the plasma discharge. Repeating the argon cleaning procedure three times during the fifteen minutes allowed for the pumping away of "sputtered" molecules and the reintroduction of fresh gas.

Once the cleaning procedures were completed the system was pumped down to a pressure of approximately  $1 \times 10^{-5}$  torr. Indium contacts were then evaporated followed by the evaporation of a 2000 Å aluminum base layer. The film thickness during deposition was monitored using a

Sloan DTM-3 quartz crystal monitor. For the aluminum base film a deposition rate of 70 Å/sec was used. A shutter system allowed one to establish a desired evaporation rate prior to actual deposition onto the glass substrate.

After the base film was completed the substrate was raised to a position 5 cm below the level of the inner copper electrode. A plasma discharge technique similar to that described by Miles and Smith (98) was used for preparation of the oxide insulating barrier. The gas mixture used consisted of 80 microns of oxygen to which was added 120 microns of helium for a total pressure of 200 microns (40% O<sub>2</sub>, 60% He). Matheson research-grade oxygen (99.99% purity) and helium (99.9999% purity) were used. At full output of the power supply (Heathkit PS-3 regulated power supply) currents of 2 to 6 mA with voltages of the order of 375-430 V were produced. Oxidation times ranged from 15-30 minutes depending upon the thickness of oxide desired. The plasma itself took on a pale ghostly green appearance and covered an extensive area whereas a discharge in pure oxygen was purple pink in color with an extent closely confined to the inner copper electrode. As shown in Table 4.2 plasma discharge characteristics vary as the oxygen-helium ratio is altered. The origin of these colors probably lies in the "forbidden" transitions responsible for auroral colors due to oxygen (27, 95, 96).

Once the oxidation was complete the system was again pumped down to  $\sim 1 \times 10^{-5}$  torr and top electrodes of



Table 4.2  
 Plasma Discharge Characteristics of Various  
 $O_2/He$  Gas Mixtures

Method - obtain desired  $O_2$  pressure, then fill to ~ 200  
 microns with He.

Pressure ( $\mu$ )		Discharge Color	Maximum Voltage (V)	Maximum Current (mA)
$O_2$	$O_2+He$			
0	200	very diffuse pale blue	410	~ 0.9
50	230	green	~ 420	~ 3.0
80	210	green	420	3.0
100	200	ghostly green bluish pink	415	4.0
130 <sup>i</sup>	200	gentle purplish pink	415	5.5
150	200	purplish pink	415	~ 6.5
185	185	purple pink	415	~ 10.0

2000 Å were evaporated. The first 200 Å were evaporated very slowly - in order to disturb the oxide layer as little as possible - at a rate of  $\sim 7 \text{ Å/sec}$  with an increasing rate for the remaining 1800 Å.

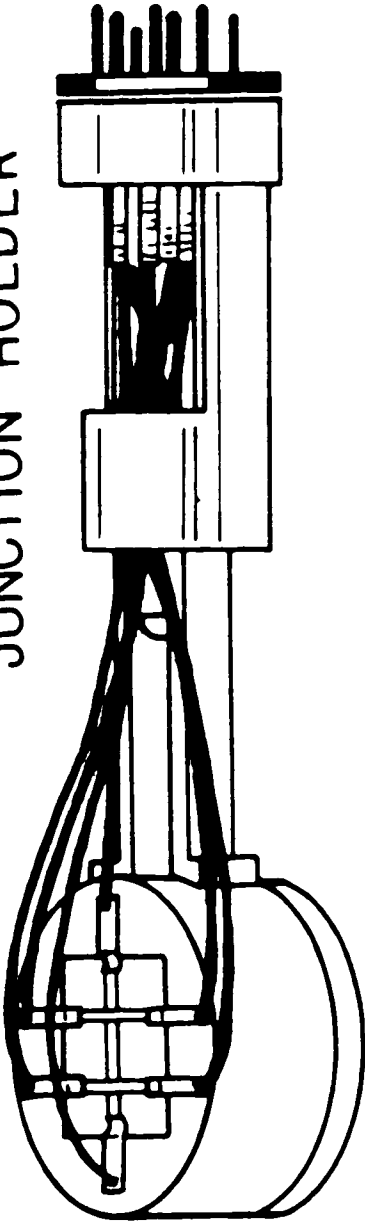
Once the junctions were completed, the evaporator system was vented to room air and the substrate was placed in a holder bearing springy, gold coated pressure contacts which provided for electrical connection to the junctions. Between each springy contact, and evaporated contact of a junction, a small flat piece of indium was placed. This was done to insure against contact failure in the course of annealing studies during which junctions were thermally cycled many times and studied for long periods of time (i.e. months). After this was done, the electrical continuity of each metal film was checked; the holder with the junctions was then attached to a "dipstick" (see Fig. 4.2) and placed in liquid nitrogen. The time elapsed between junction completion and immersion in liquid nitrogen was about 10 minutes, during which annealing could occur.

This method of junction fabrication was done without exposing the system to the outside atmosphere at any time during sample preparation, thus cutting down on contamination. Furthermore, once the plasma discharge parameters (gas mixture, pressure, discharge current and voltage, time, and substrate positioning) were known, a very high degree of reproducibility and control of oxidation was had. The failure rate of aluminum-aluminum oxide-lead junctions,

Fig. 4.2

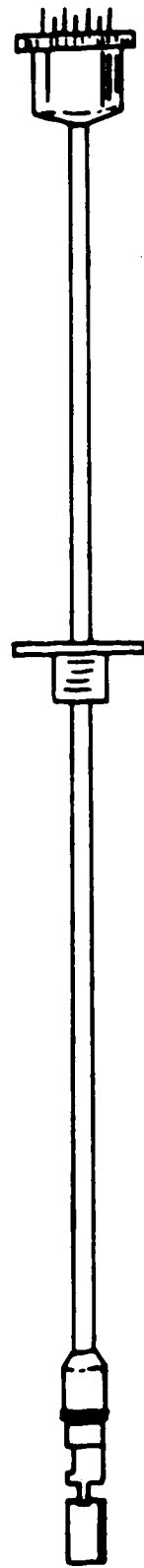
Dipstick and junction holder.

JUNCTION HOLDER



7 cm

~1.3 m



DIPSTICK

for example, was nil.

#### 4.2. Modulation Spectroscopy

Measurements of quantities proportional to the junction conductance  $\sigma$  ( $=dI/dV$ ) and its derivative  $d\sigma/dV$  ( $=d^2I/dV^2$ ) both with respect to voltage ( $I$  is the junction current) were made using a technique called modulation spectroscopy. In this, one perturbs a sample with a periodic signal (modulation signal) of a certain frequency and measures the sample's response (108).

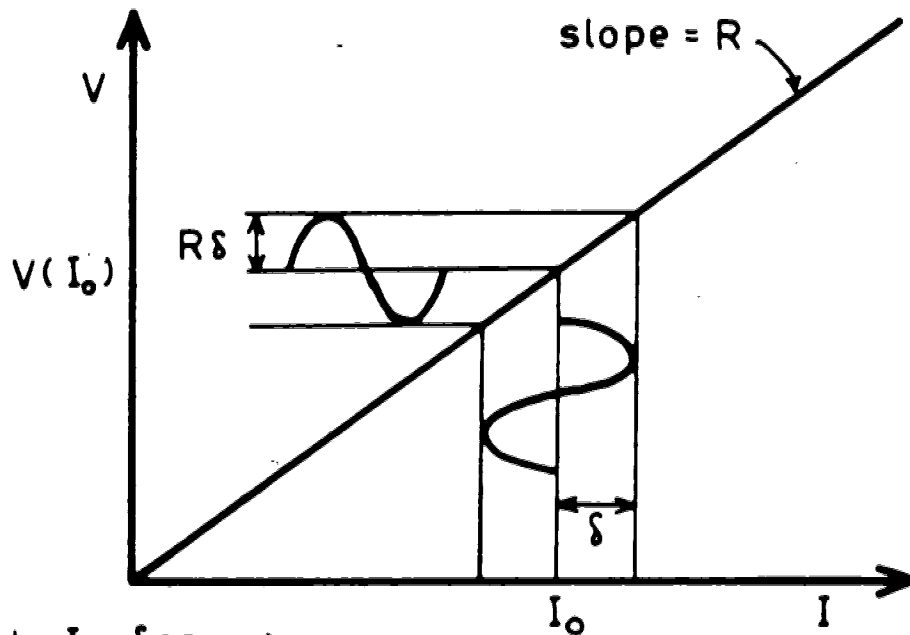
For example, one may apply a sinusoidally varying current (perturbation) of frequency  $\omega$  and amplitude  $\delta$  through a resistor (a linear device). The measured response would be a sinusoidally varying voltage of frequency  $\omega$  and amplitude  $R\delta$  where  $R$  is the resistance of the resistor. This is shown diagrammatically on the I-V characteristic of a resistor in Fig. 4.3(a). Moving one step further, consider the characteristic of a device shown in Fig. 4.3(b). A voltage response with the frequency  $\omega$  of the modulation current still occurs but the amplitude depends upon the slope of the I-V curve.

If one now takes a more general curve one may obtain the type of responses shown in Fig. 4.4. Approximating the above with idealized straight lines one obtains signals as shown in Fig. 4.5. These resulting signals can be easily Fourier analyzed with the aid of the formulas depicted in Fig. 4.6. Hence, the signal in each

Fig. 4.3

Basics of modulation spectroscopy.

(a)



$$\text{Signal} = I_0 + \delta \cos \omega t$$

$$\text{Response} = V(I_0) + R\delta \cos \omega t$$

(b)

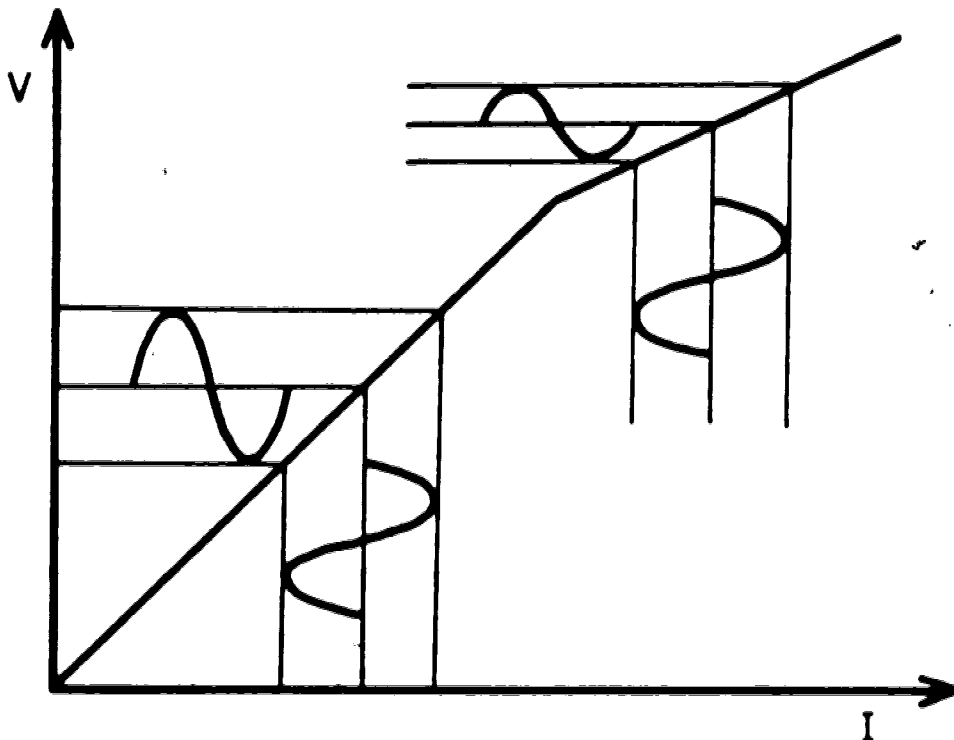


Fig. 4.4

General characteristic and response to modulation signal.



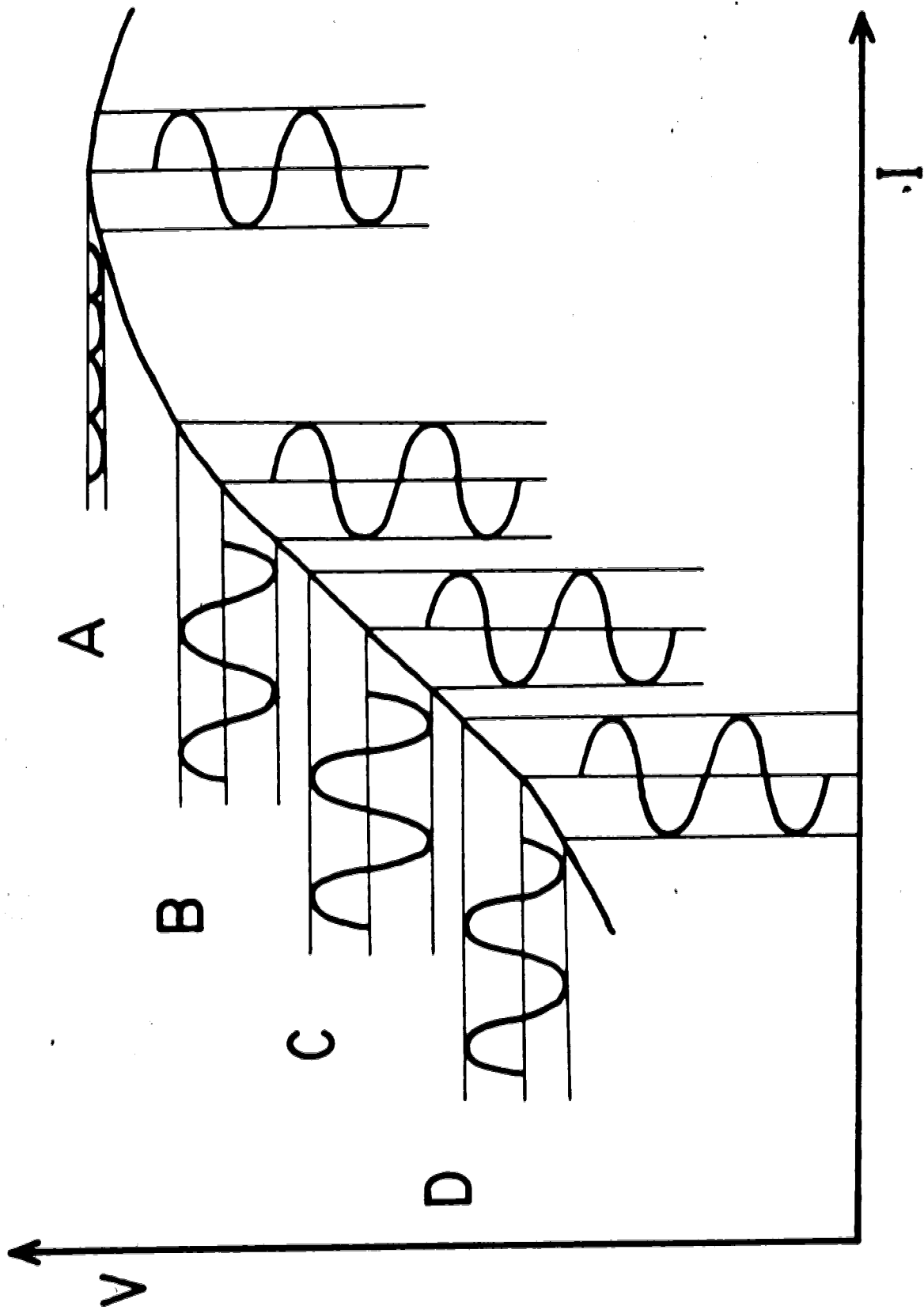


Fig. 4.5

Idealized response.

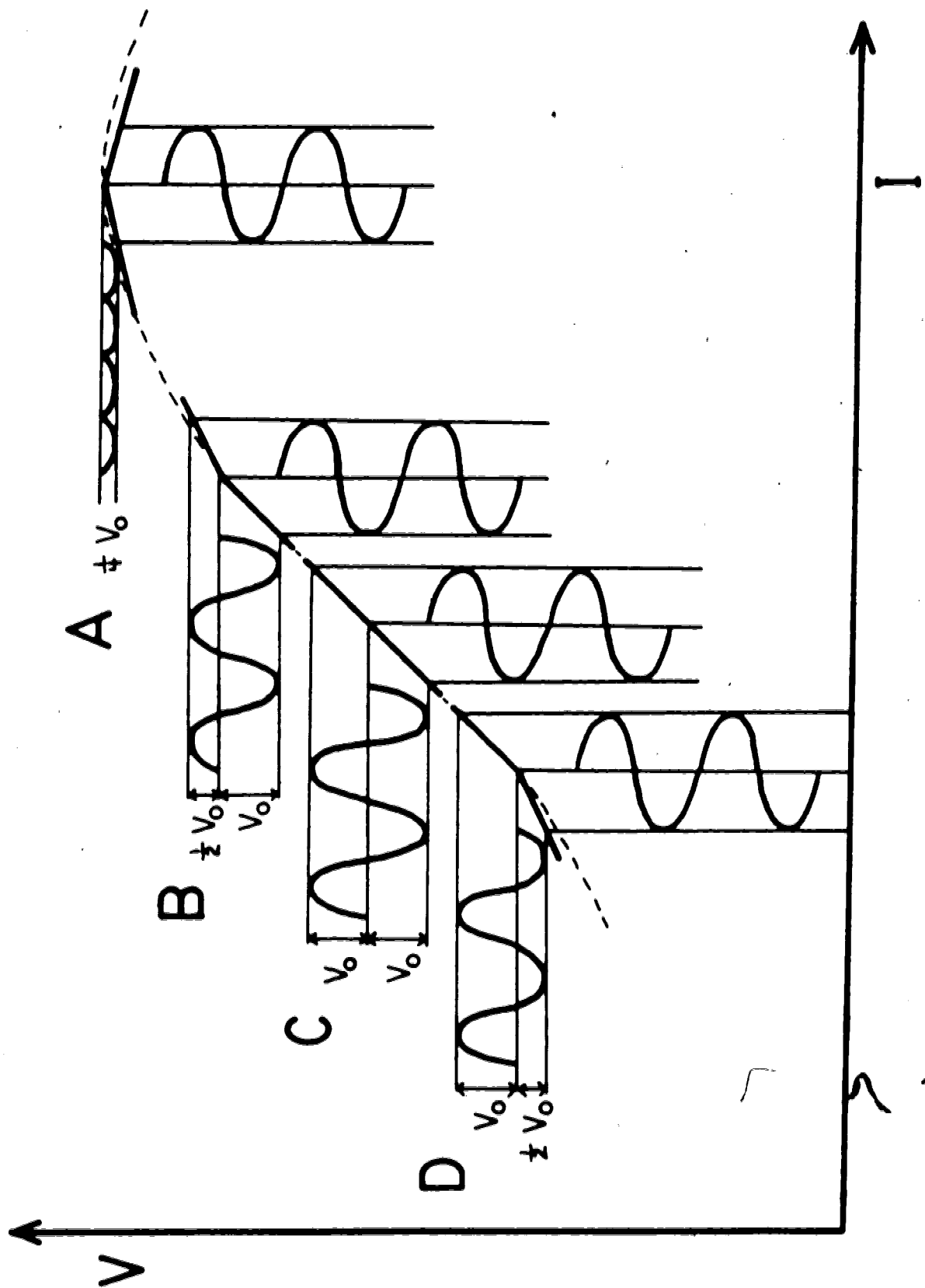
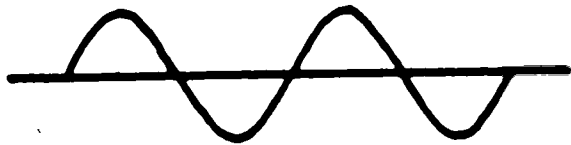


Fig. 4.6

Several signals to be used in the Fourier analysis of the idealized response signal are shown.

a



$$v_o \sin \omega t$$

b



$$v_o \left[ \frac{1}{\pi} + \frac{1}{2} \sin \omega t - \right.$$

$$\left. \frac{2}{\pi} \sum_{k=2,4,6}^{\infty} \frac{\cos(k\omega t)}{(k+1)(k-1)} \right]$$

c



$$v_o \left[ -\frac{1}{\pi} + \frac{1}{2} \sin \omega t + \right.$$

$$\left. \frac{2}{\pi} \sum_{k=2,4,6}^{\infty} \frac{\cos(k\omega t)}{(k+1)(k-1)} \right]$$

d



$$v_o \left[ \frac{2}{\pi} - \frac{4}{\pi} \sum_{k=2,4,6}^{\infty} \frac{\cos(k\omega t)}{(k+1)(k-1)} \right]$$

part of the curve of Fig. 4.5 may be written as

$$\begin{aligned} \text{A } v &= \frac{V_0}{\pi} \left[ -\frac{1}{2} + \frac{1}{3} \cos 2\omega t + \frac{1}{15} \cos 4\omega t + \dots \right] \\ &\equiv \left[ -\frac{1}{4} \text{ eq. (d)} \right]. \end{aligned}$$

$$\begin{aligned} \text{B } v &= \frac{V_0}{\pi} \left[ -\frac{1}{2} + \frac{3\pi}{4} \sin \omega t + \frac{1}{3} \cos 2\omega t + \frac{1}{15} \cos 4\omega t + \dots \right] \\ &\equiv \left[ \frac{1}{2} \text{ eq. (b)} + \text{eq. (c)} \right]. \end{aligned}$$

$$\text{C } v = V_0 \sin \omega t \equiv [\text{eq. (a)}].$$

$$\begin{aligned} \text{D } v &= \frac{V_0}{\pi} \left[ \frac{1}{2} + \frac{3\pi}{4} \sin \omega t - \frac{1}{3} \cos 2\omega t - \frac{1}{15} \cos 4\omega t - \dots \right] \\ &\equiv \left[ \frac{1}{2} \text{ eq. (c)} + \text{eq. (b)} \right]. \end{aligned}$$

One thus sees that higher harmonics of the fundamental frequency exist when one applies a modulated current signal to a device with a non-linear I-V characteristic curve. It should be noted that the above Fourier analysis merely approximates a real situation, but nonetheless gives a mathematical insight into the actual physical situation.

It is seen that in regions of non-linearity the response signal is distorted. Fourier analysis tells us that this signal can be represented as a superposition of sinusoids of various amplitudes and multiples of the

fundamental frequency. A tunnel junction is a non-linear device, and so if a current modulation of certain frequency is applied, the response voltage will be a distorted signal containing frequency and amplitude components dependent upon the position along the I-V curve of the junction.

Mathematically, given a modulation current  $\delta \cos \omega t$  of constant amplitude  $\delta$ , the voltage  $V$  developed across the tunnel junction may be written in terms of a Taylor series,

$$V(I) = V(I_0) + \left( \frac{dV}{dI} \right)_{I_0} \delta \cos \omega t + \frac{1}{2} \left( \frac{d^2V}{dI^2} \right)_{I_0} \delta^2 \cos^2 \omega t + \dots \quad (4.1)$$

where  $V(I_0)$  is the DC bias of the junction and  $\omega$  is  $2\pi$  times the modulating frequency. One notes that with a linear element,  $(d^2V/dI^2)_{I_0}$  and higher derivatives vanish, whereas with the non-linear tunnel junction, they are non-zero. Equation (4.1) can be rewritten as

$$V(I) = V(I_0) + \left( \frac{dV}{dI} \right)_{I_0} \delta \cos \omega t + \frac{1}{4} \left( \frac{d^2V}{dI^2} \right)_{I_0} \delta^2 (1 + \cos 2\omega t) + \dots \quad (4.2)$$

From Eq. (4.2) one sees that if  $\delta$  is constant then the component of voltage across the junction at angular frequency  $\omega$  is proportional to  $(dV/dI)_{I_0}$  and the component at  $2\omega$  is proportional to  $(d^2V/dI^2)_{I_0}$ . Thus, by using a modulation technique, one is able to produce voltage

signals proportional to the desired first and second derivatives of the tunnel junction I-V characteristic.

#### 4.3. Measurement of Tunneling Information

The dynamical conductance  $\sigma = dI/dV$  and its derivative,  $d\sigma/dV$ , with respect to voltage comprise the desired information about the tunnel junction. This information was obtained by a system using a combination of modulation and bridge techniques with harmonic detection, suitably interfaced to a minicomputer facility to record and store digital data.

To understand the principle of harmonic detection (1), consider the simplified bridge circuit shown in Fig. 4.7. Here, a junction of resistance  $R_t$ , serves in one arm of an AC Wheatstone bridge while the other arm contains the variable resistor  $R_d$  set so that  $R_d = R_t$  in order to balance the bridge; we also set  $R \gg R_d$  and  $R_t$ . With the bridge thus close to balance, the current through each arm is practically the same. With  $\delta \cos \omega t$  being the AC (modulation) current in each arm, we have

$$V_1 = R_d \delta \cos \omega t$$

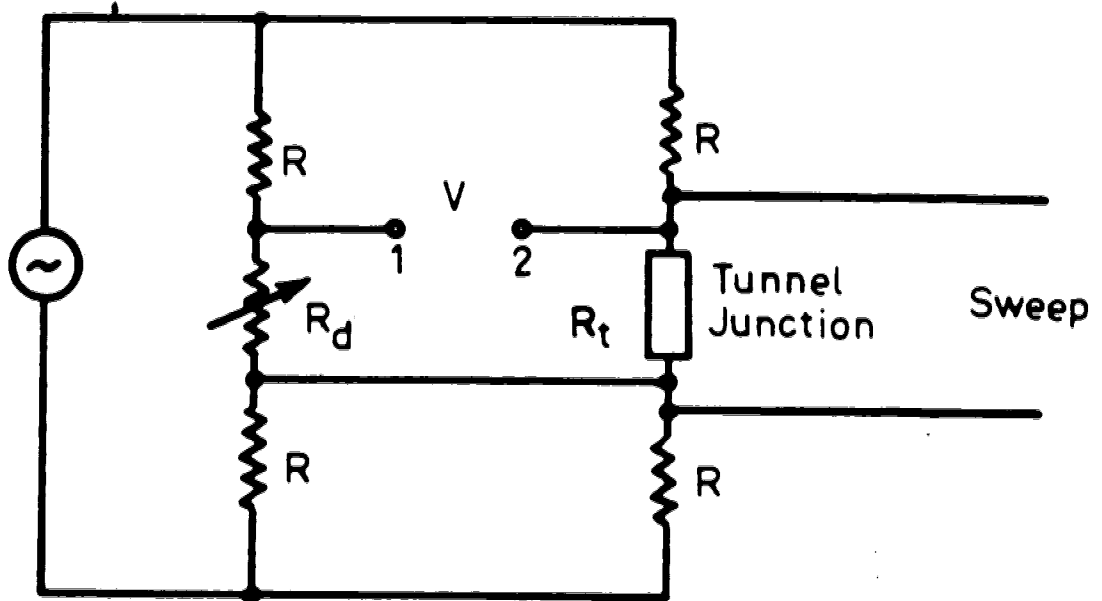
$$V_2 = I_0 R_d + (dV/dI)_{I_0} \delta \cos \omega t + \frac{1}{4} (d^2V/dI^2)_{I_0} \delta^2 (1 + \cos 2\omega t) + \dots$$

where  $I_0$  is the DC bias current flowing through the junction, and  $R_t = R_d$  at bridge balance. The difference in potential between points 1 and 2,  $V_{12}$ , has components at the modulating frequency  $\omega$  and at higher harmonics. We



Fig. 4.7

This figure shows a simple bridge circuit.



see that the signal at the fundamental frequency,  $V_{12}(\omega)$ , is proportional to the difference between the dynamic resistance  $(dV/dI)_{I_0}$  and  $R_d$

$$V_{12}(\omega) = \delta [R_d - (dV/dI)_{I_0}] \cos \omega t.$$

The second harmonic component,  $V_{12}(2\omega)$  is proportional to  $(d^2V/dI^2)_{I_0}$

$$V_{12}(2\omega) = \frac{1}{4} \delta^2 (d^2V/dI^2)_{I_0} \cos 2\omega t.$$

These two signals are measured by use of lock-in amplifiers.

Direct calibration of  $dV/dI$  by the use of a decade resistance box, enables the computation of the dynamical conductance  $\sigma = dI/dV$ . In the ideal case, the second derivative  $(d^2I/dV^2) = d\sigma/dV$  is then calculated from the second harmonic signal ( $V_{12}(2\omega)$ ) using the identity:

$$\frac{d^2I}{dV^2} = -\sigma^3 \cdot \frac{d^2V}{dI^2}$$

derived as follows:

$$\begin{aligned} \frac{d^2I}{dV^2} &= \left( \frac{d}{dV} \right) \left( \frac{dI}{dV} \right) = \left( \frac{dI}{dV} \right) \left( \frac{d}{dI} \right) \left[ 1 / \left( \frac{dV}{dI} \right) \right] = \\ &= - \left[ \left( \frac{dI}{dV} \right) \left( 1 / \left( \frac{dV}{dI} \right)^2 \right) \right] \left( \frac{d^2V}{dI^2} \right) = -\sigma^3 \cdot \frac{d^2V}{dI^2}. \end{aligned}$$

The presence of second harmonic distortion in the measurement system complicates the above relation and necessitates the use of a somewhat different numerical method to calibrate  $d\sigma/dV$ . The details of this are described elsewhere (4, 5). We are thus able to have calibrated values of the conductance  $\sigma$ , and its derivative  $d\sigma/dV$ , both with respect to bias voltage. The use of a minicomputer based system allows for easy manipulation of increasing data as well as speedy data analysis. Capabilities of the system are described by Adler and co-workers (4, 5). Fig. 4.8 shows a current layout of the data acquisition and handling system.

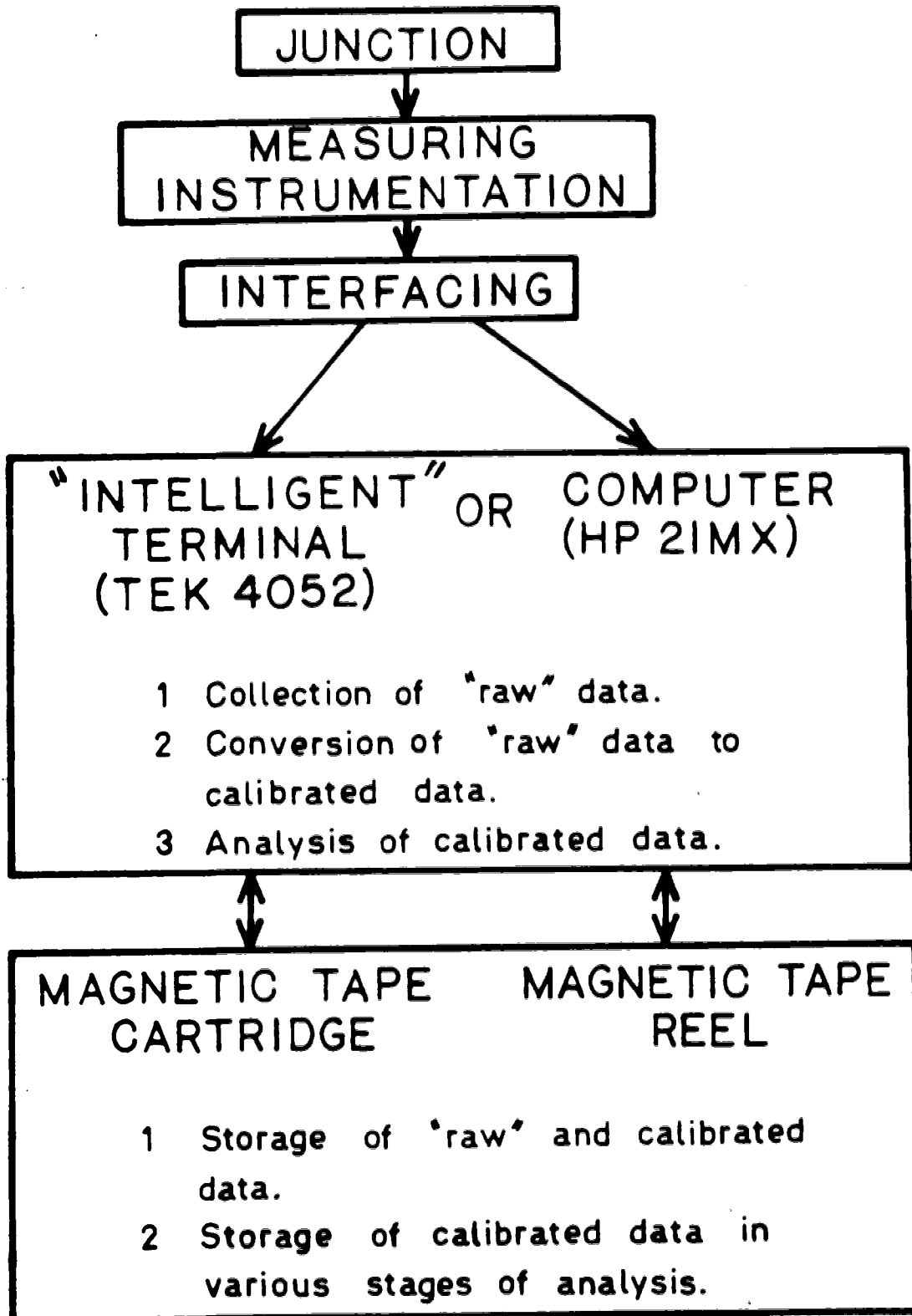
#### 4.4. Annealing Procedure

The thermal annealing experiments were carried out by removing a junction from liquid nitrogen temperature and placing it at room temperature, about 20°C, for the desired length of time. To prevent the ice which formed on the tunnel junction electrodes (when removed from liquid nitrogen to room air) from melting and subsequently damaging the junction, annealing was carried out in a vacuum. After annealing, the junction was again put into liquid nitrogen until ready for measurement at 4.2 K in liquid helium.

The voltage annealing experiments were also carried out at room temperature in a vacuum. The control junction was allowed to undergo thermal annealing (open circuit)

Fig. 4.8

Layout of data acquisition system.



while the other junction of the pair was biased at the desired voltage and polarity as depicted in Fig. 4.9.

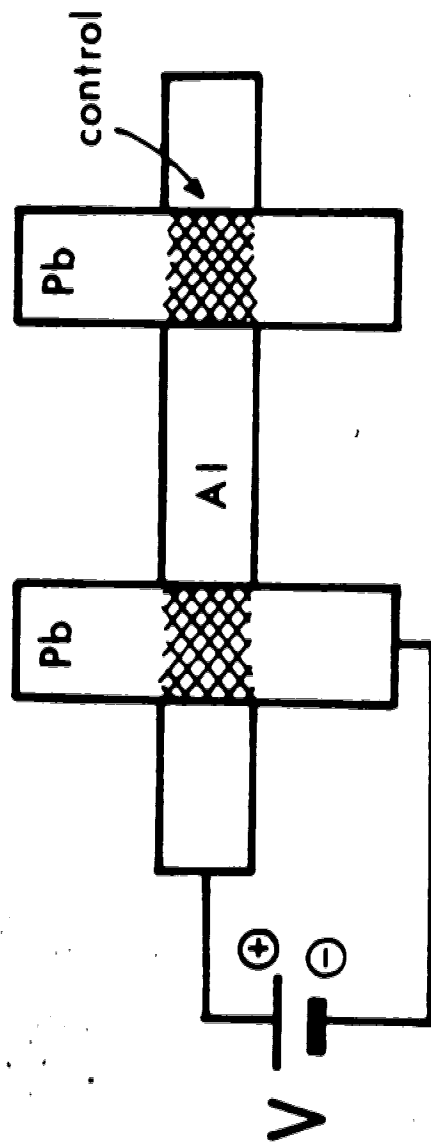
Since the nature of the annealing study involved many measurements on the same junction (i.e. at 0, 2, 4, 8 hours, etc.) the instrumental settings of the measuring system were kept as similar as possible from one measurement to the next.

Fig. 4.9

In this set-up, one junction of a pair is voltage annealed while the other serves as a control and is thermally annealed.



Al-Al oxide - Pb



## CHAPTER 5

### DATA ANALYSIS AND FUNDAMENTAL INFORMATION

#### 5.1. Introduction

In this chapter, the extraction of basic information from tunneling data will be discussed. Topics include peak identification in  $d\sigma/dV$ , the IET (inelastic electron tunneling) spectrum, determination of barrier parameters from conductance curves, and the intensities of IET peaks.

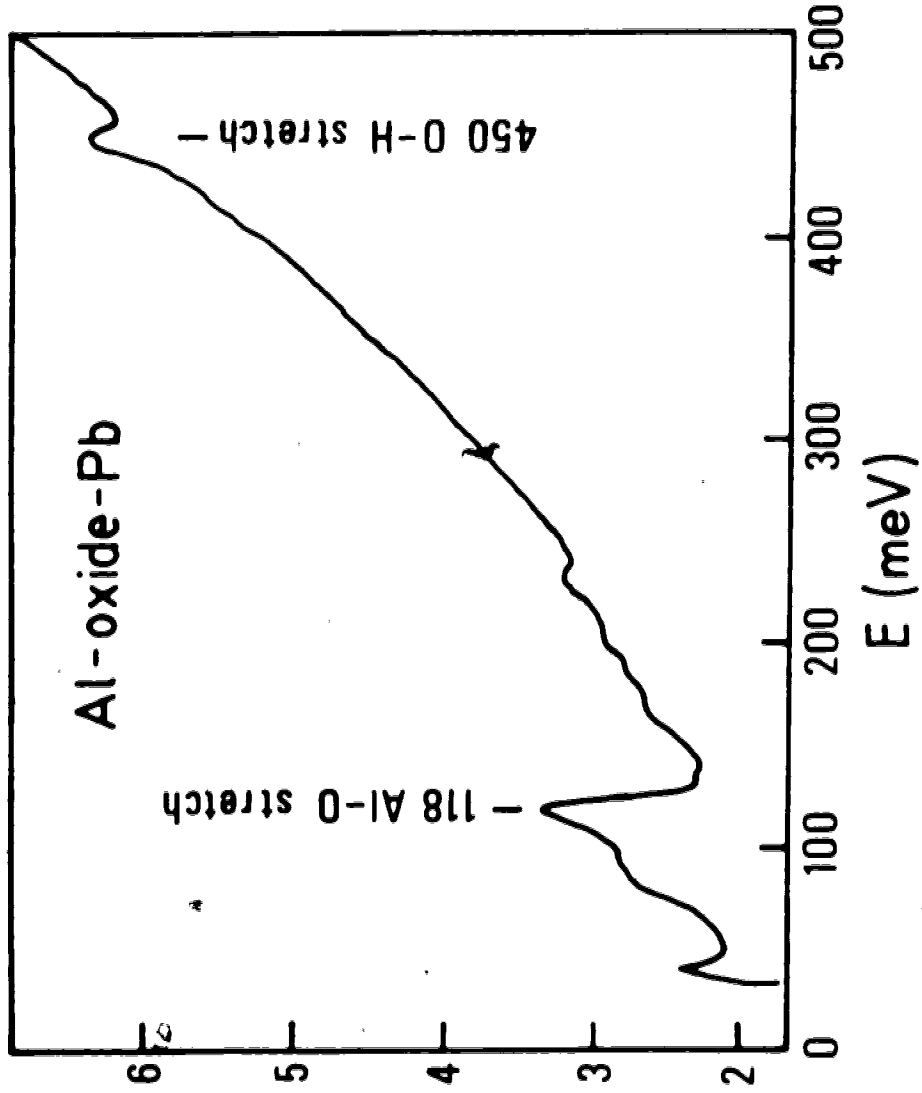
#### 5.2. Peak Assignments

The assignment of vibrational modes due to certain molecular groups, on the basis of the energy at which peaks occur in the IET spectrum will now be discussed. Fig. 5.1 shows a typical spectrum of an Al-aluminum oxide-Pb tunnel junction. Based on infrared and Raman spectroscopic studies, as well as the knowledge of what was used in making the barrier, one can identify the peaks which occur. Using the work of Geiger, Chandrasekhar, and Adler (51), plus that of Bowser and Weinberg (17), one gets the following assignments for peak positions in a relatively clean Al-oxide-Pb junction as compiled in Table 5.1.

The peak which occurs near 450 meV is assigned to the O-H stretching of hydroxyl groups located on the surface of the aluminum oxide. Since hydrogen was not

Fig. 5.1

This figure shows the IET spectrum of an Al-Al oxide-Pb junction.



$$10^6 \frac{dI}{dV} (\Omega^{-1} \text{mV}^{-1})$$

Table 5.1

## IET Peak Assignments for Al-Al oxide-Pb Junction

Peak Position (meV)	Identification
37	Al phonon
75	surface OH bend
90	surface OH bend
118	Al-O stretch (aluminum oxide)
118	Al-OH bend (of alumina hydrate)
165	combination and overtone peaks from 75 and 90 meV fundamental peaks
235	overtone of 118 meV peak
450	surface OH stretch

deliberately added to the oxygen-helium mixture used in producing the oxide barrier, the hydrogen was probably due to residual water vapor in the evaporator system. Values for OH stretching via infrared data (114) for alcohols and phenols are given as 1)  $3584-3650 \text{ cm}^{-1}$  (437-445 meV) for the "free" hydroxyl group and 2)  $3200-3550 \text{ cm}^{-1}$  (389-432 meV) when intermolecular hydrogen bonding - the interaction via hydrogen bonding between OH groups - comes into play. Positions for OH bending are given as 1)  $1330-1420 \text{ cm}^{-1}$  (162-173 meV) for OH in-plane bending, and 2)  $650-769 \text{ cm}^{-1}$  (79-94 meV), a broad absorption band shown in the spectra of alcohols and phenols determined in the liquid state due to out-of-plane bending of the bonded OH group.

According to Bowser and Weinberg, the absence of a peak near 198 meV ( $1600 \text{ cm}^{-1}$ ) excludes the possibility of the OH being associated with molecularly adsorbed water (87). They conclude that the hydroxyl groups responsible for the 450 meV stretching, and the 75 and 90 meV bending modes are located on the surface of the aluminum oxide insulator (as opposed to being incorporated in the bulk as aluminum hydroxide).

The assignment of the small peak at about 235 meV as the overtone of the 118 meV peak is generally accepted, however, the identification of the 118 meV peak itself still arouses some controversy. Based on the IR work of Dorsey (36, 37) with anodic aluminum oxides, Geiger,

Chandrasekhar, and Adler (51) attributed this peak as being due to the alumina hydrate Al-OH bending mode of an aluminum trihydroxide (or trihydrate) even though the expected OH stretching mode for alumina hydrate at about 420 meV was absent. Dorsey suggested that the absence of this stretching band could be due to the existence of strong hydrogen bonding present within the alumina which would reduce the intensity of such a band by broadening it.

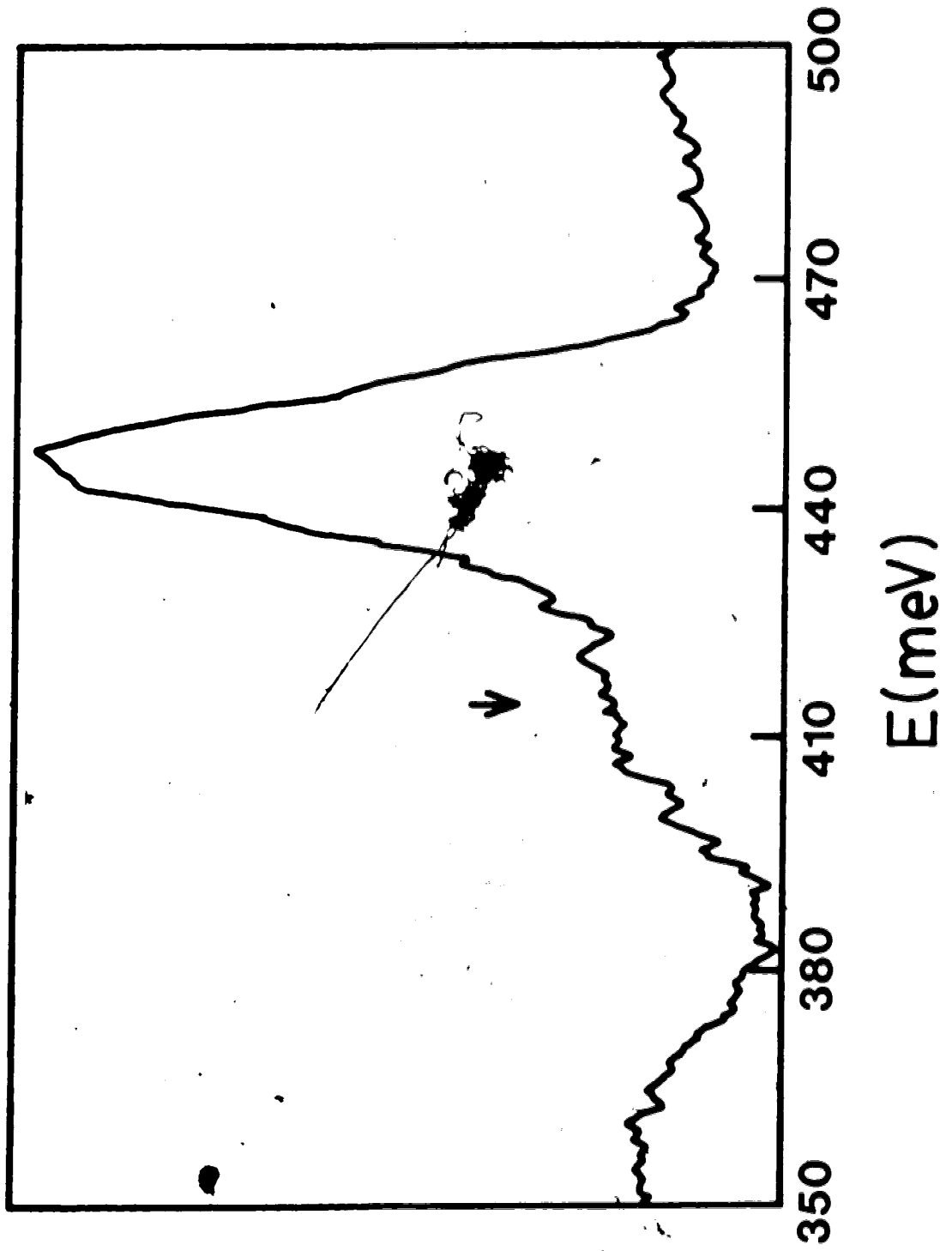
Lewis, Mosesman, and Weinberg (85), on the other hand, suggests that this peak is due to the Al-O stretching mode of an aluminum oxide. The more recent work of Bowser and Weinberg (17) strongly supports the idea of the 118 meV peak as being due mainly to the Al-O stretching mode of aluminum oxide. They do, in addition, find some evidence for the existence of some aluminum hydroxide (monitored by the proposed 118 meV bending mode) within the bulk aluminum oxide based on work with deuterated samples (as did Geiger et al.). Again, they too see no evidence for the AlO-H stretching mode.

If one looks closely at the region of the surface OH stretching peak (Fig. 5.2), one does see a small bump at about 415 meV which could be due to the missing AlOH stretching peak. The weakness in intensity of this peak as well as that contributing to the bending mode would suggest that very little aluminum hydroxide exists, and that the insulator is composed primarily of aluminum oxide.

Fig. 5.2

The surface OH stretching peak at 450 meV is shown along with the small peak at ~ 415 meV.





$$\left( \frac{d\sigma}{d\Omega} \right) \text{ (mb}^{-1}\text{)}$$

It should be noted that the peak at  $\sim 415$  meV could also be due to hydrogen bonding of the surface OH groups, or due to N-H stretching modes (114). Even so, this does not change the conclusion that the barrier is composed primarily of aluminum oxide with some aluminum hydroxide within the insulator and "free" OH on the aluminum oxide surface.

Other work on aluminum oxide using infrared methods reveal some interesting points. Takamura, Kihara-Morishita, and Moriyama (120), using anodic aluminum oxide films, observed a peak at  $955 \text{ cm}^{-1}$  (116 meV) in the infrared reflectance spectrum of this material. They proposed that this was due to an Al-O stretching mode. Slightly earlier work of Vedder and Vermilyea (125) observed a band at  $960 \text{ cm}^{-1}$  (117 meV) and one at  $660 \text{ cm}^{-1}$  (80 meV) (transmission spectrum). Both bands were associated with Al-O stretching, the  $960 \text{ cm}^{-1}$  band corresponding to longitudinal modes.

More recently, Maeland, Rittenhouse, Lahar, and Romano (90) studied the infrared reflection and transmission spectra of anodic aluminum oxide films. Their reflection spectrum showed a band at  $960 \text{ cm}^{-1}$  (117 meV) which they assigned to the longitudinal mode of the Al-O vibration. The transmission spectrum showed a band at  $650 \text{ cm}^{-1}$  (79 meV) which was assigned to the transverse mode of the Al-O vibration. These assignments were based on the work of Berreman (14) who suggested that in thin films, one should

be able to observe both longitudinal and transverse optic modes depending upon sample geometry and whether reflection or transmission infrared spectroscopy is used.

These works further support the idea of the 118 meV peak as being due mainly to Al-O stretching (longitudinal mode), and also open up the possibility that one may expect to see some contribution from the 79 meV band (transverse mode of Al-O stretching). Thus, one has the following: 1) the 118 meV peak due mainly to Al-O longitudinal modes and some alumina hydrate (Al-OH) bend, and 2) the broad shoulder by the 118 meV peak due to a superposition of Al-O transverse modes of the aluminum oxide with bending modes at 75 and 90 meV due to surface hydroxyl groups. Resolving the contribution due to each mode is no simple problem.

The last region of interest lies between 160 and 240 meV, and is made up of relatively low intensity bands. These bands are ascribed to overtone and combination bands of modes present at 75-118 meV. Bowser and Weinberg suggest that the 165 meV peak would correspond to a combination of the 75 and 90 meV surface OH bending with possible contributions from the first overtones of these fundamental modes. As previously mentioned, the 235 meV peak is thought to be the first overtone of the 118 meV peak.

### 5.3. Data from Tunneling Curves

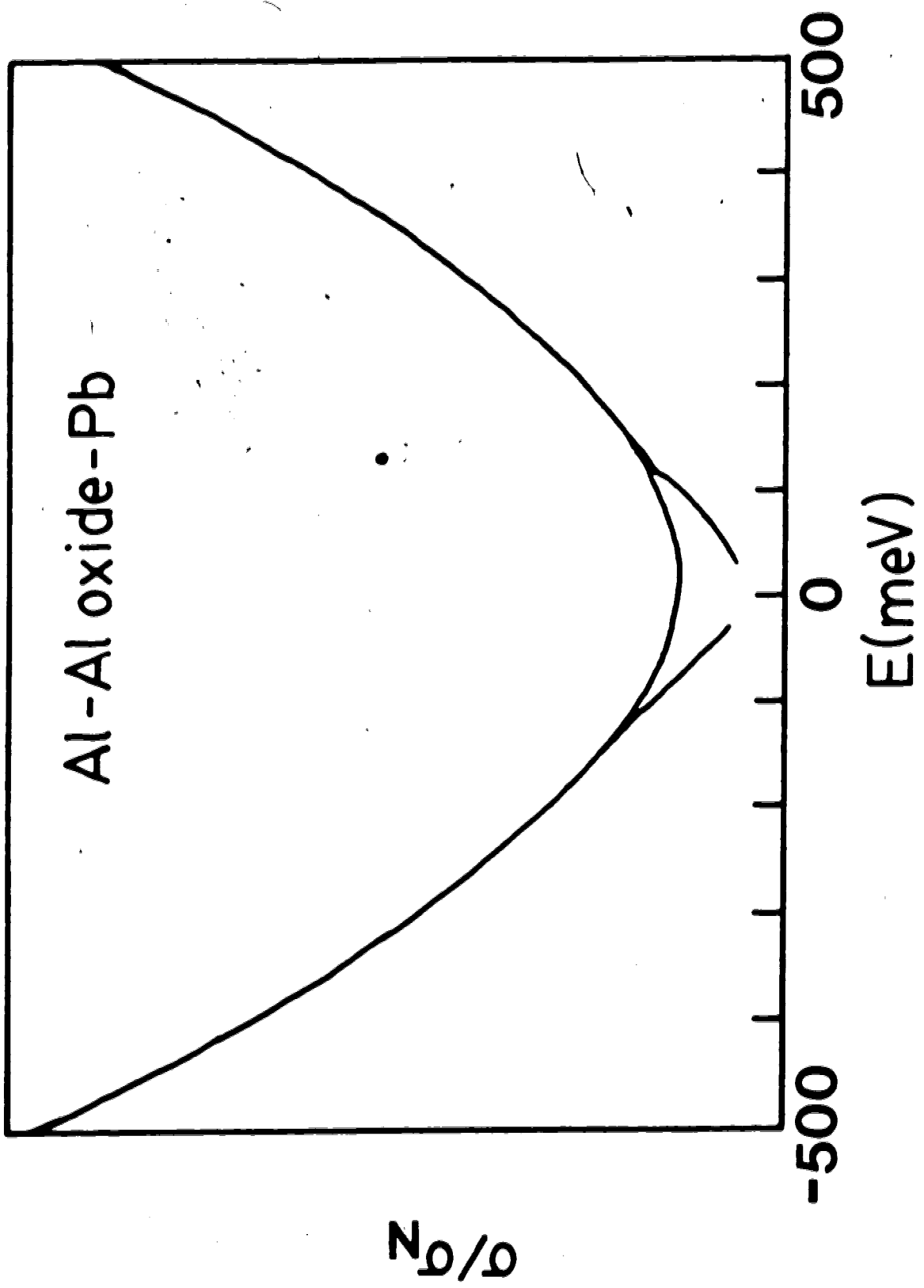
Several pieces of information are taken from the tunneling curves. From the conductance curve,  $\sigma(V)$  versus  $V$ , the junction resistance at  $-30$  mV,  $R(-30 \text{ mV}) = 1/\sigma(-30 \text{ mV})$ , is obtained. The region between  $-30$  and  $+30$  mV was avoided on account of the large structure due to the superconducting lead-electrode energy gap and phonons.

The conductance curve was also fitted with a sixth-order polynomial in the energy regions of  $-500$  to  $-150$  meV and  $150$  to  $500$  meV (Fig. 5.3); the conductance in this region is due primarily to elastic tunneling whereas between  $-150$  and  $150$  meV pronounced inelastic tunneling due to aluminum oxide modes occurs. Using the Brinkman, Dynes, and Rowell (BDR) equation 7 (20) for elastic conductance along with our resistance  $R(-30 \text{ meV})$  plus the linear and quadratic coefficients of the polynomial fit, junction barrier parameters were calculated (77). These are  $s$ : the junction thickness,  $\bar{\phi}$ , the average barrier height ( $\bar{\phi} = \frac{1}{2} [\phi_1 + \phi_2]$  at zero bias), and  $\Delta\phi = \phi_2 - \phi_1$ , the difference of the barrier heights at the two electrodes. Values for the parameters  $\phi_1$  and  $\phi_2$  can be easily determined from the already calculated  $\bar{\phi}$  and  $\Delta\phi$ . The BDR model is not taken literally but rather as an indicator of the qualitative changes taking place within the barrier.

Finally, the last quantities of interest are the areas under peaks of interest in the IET spectrum ( $d\sigma/dV$

Fig. 5.3

Polynomial fit of an Al-Al oxide-Pb junction  
}conductance curve.



versus  $V$ ), referred to as peak intensities. From the calibrated data, the integrated peak intensity  $F$  is calculated by

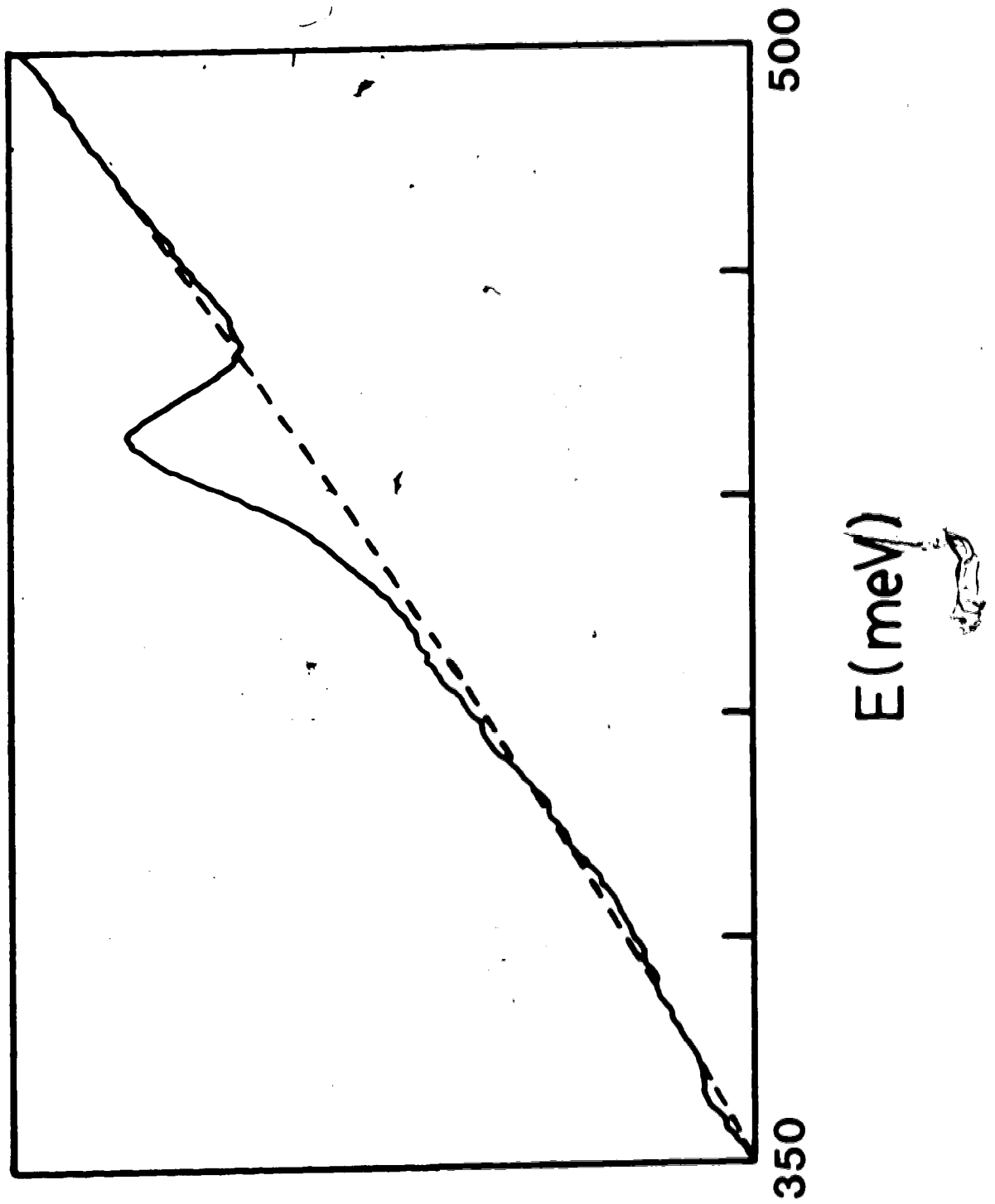
$$F = \int \left[ \frac{1}{\sigma_N} \frac{d\sigma}{dV} - g(V) \right] dV, \quad (5.1)$$

where  $\sigma_N$  is the conductance used to normalize  $d\sigma/dV$  (in this case  $\sigma_N = \sigma(-30 \text{ meV})$ ) and  $g(V)$  is the smooth background under the inelastic peak. The peaks of interest were those at 450 meV due to OH stretching as well as that at 118 meV due to Al-O stretching (the intensity of the shoulder centered at about 85 meV was also found). The background for the 450 meV peak was determined in the region between -500 to -350 or +350 to +500 (depending upon the polarity of the sweep bias which is called negative when the Al base electrode is negative) using a 3rd order polynomial as shown in Fig. 5.4. Since the choice of a background for the 118 peak was less straightforward, a linear fit using the regions depicted in Fig. 5.5 was chosen. The peak intensities were obtained by numerically integrating the area under the peak (with the background  $g(V)$  already subtracted). For the 450 meV peak the integration limits are roughly between 385-480 meV, while the limits for the 118 and 85 meV peaks are shown in Fig. 5.6. A crude estimate of the contribution due to each of the 118 and 85 meV peaks is made since they are not separately resolved peaks. However, considering

Fig. 5.4

3rd degree fit for 450 meV peak background.








Fig. 5.5

1st degree fit for 118 meV peak background.

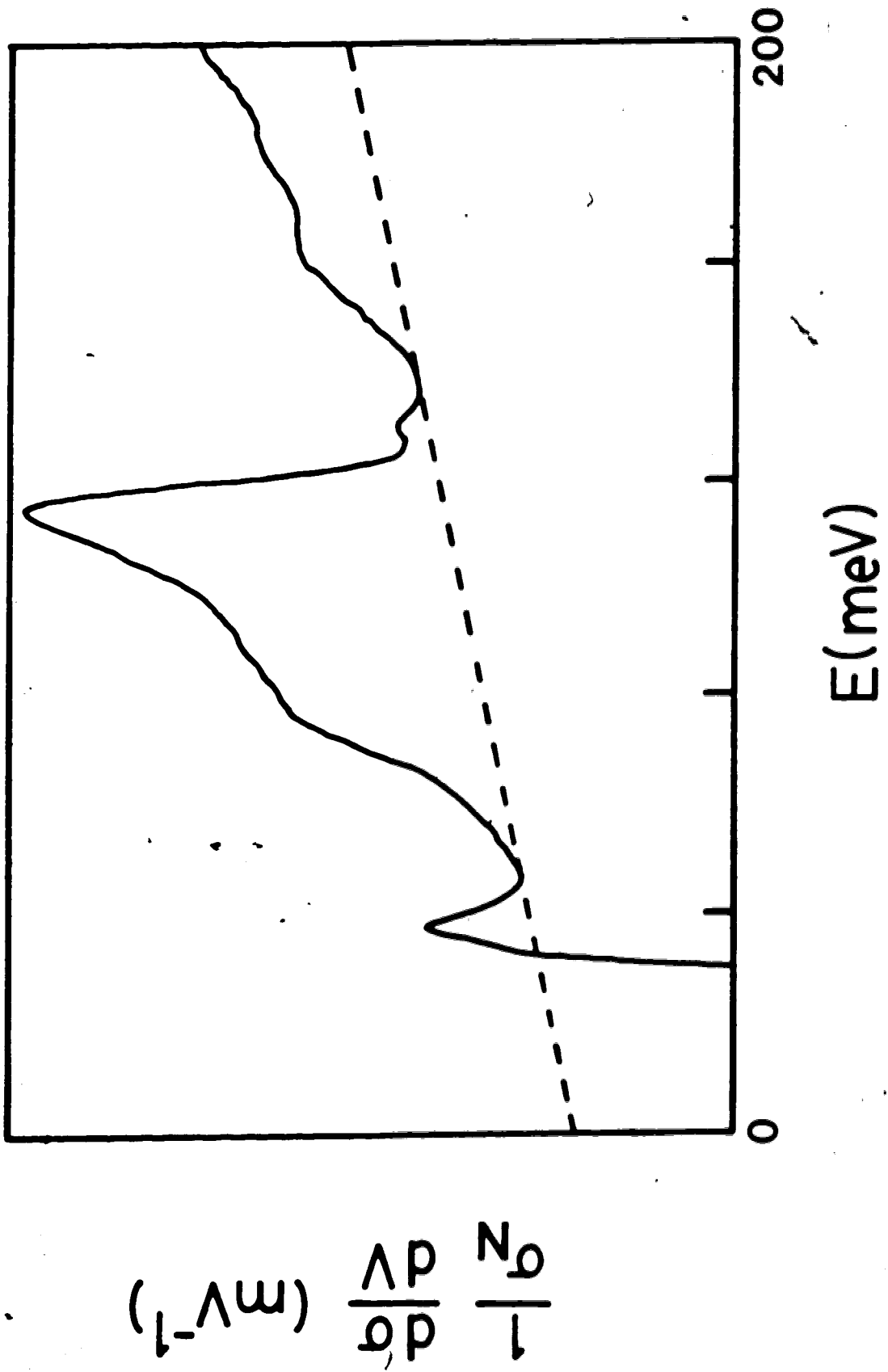
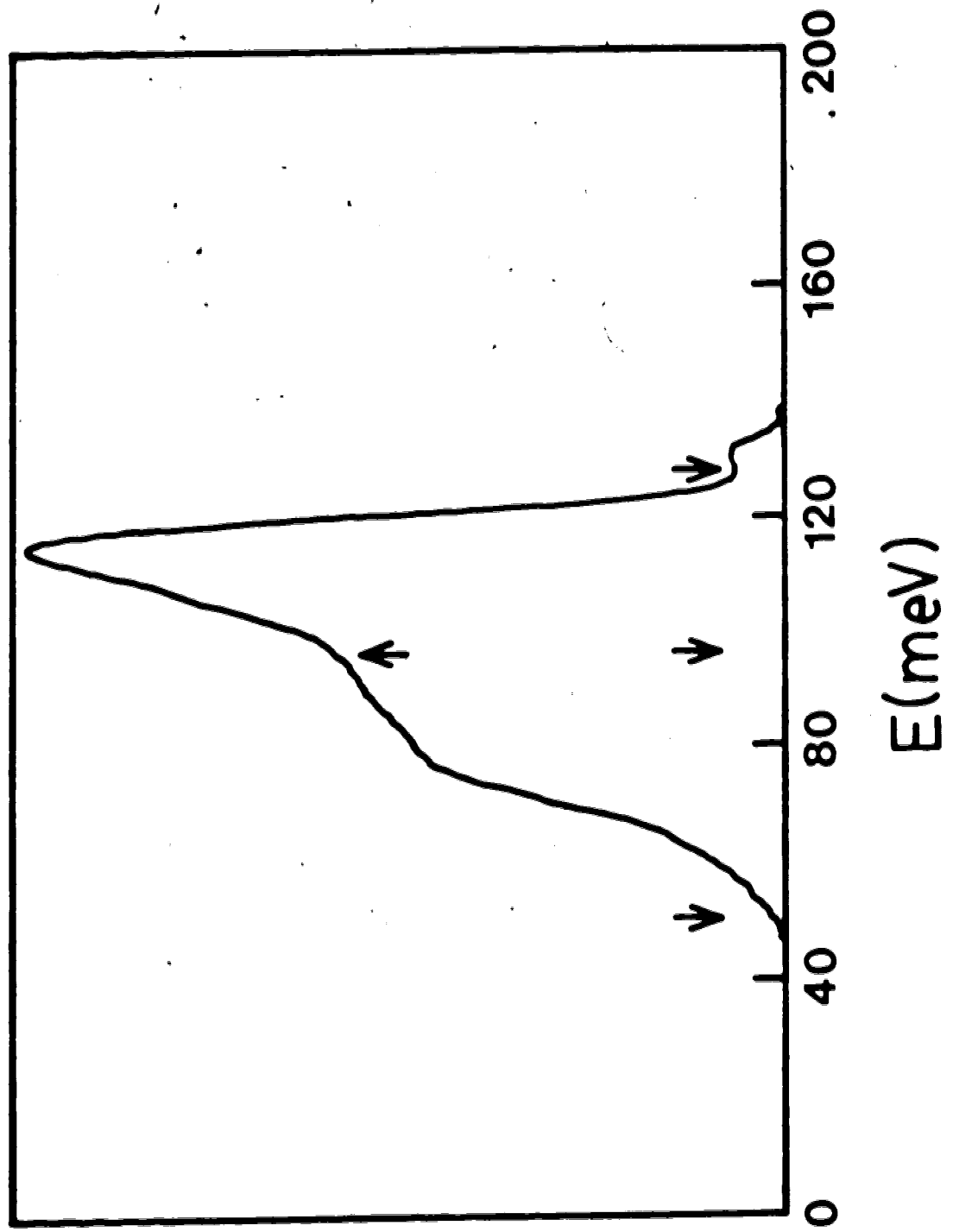


Fig. 5.6

Limits for intensity calculation for 85 and 118 meV peaks.  
For the 85 meV peak the limits are from ~ 50 - 95 meV and  
for the 118 peak from ~ 95 - 128 meV.



$$\left( \frac{\partial \rho}{\partial p} \right)_{\rho} - \frac{\Lambda p}{\rho} \left( \frac{\partial \rho}{\partial p} \right)_{\rho}$$

the estimates as to background and integration limits made for the 118 meV peak, the intensity results changed fairly smoothly with annealing and were comparable for different junctions, as will be seen later.

## CHAPTER 6

### RESULTS AND DISCUSSION

#### 6.1. Introduction

It is known that tunnel junctions left at room temperature for any length of time undergo changes in resistance (56). In order to prevent this, the junctions are stored at a low temperature (i.e. liquid nitrogen at 77 K). To carry out useful studies of phenomena such as chemisorption of organic molecules on oxide surfaces, it is necessary to have some knowledge of the temporal behaviour of the oxide barrier in junctions prior to chemisorption. This is particularly applicable to cases in which one is studying chemical changes occurring within the barrier (e.g., chemical reactions of molecules infused into oxide junctions (64)).

#### 6.2. Thermal Annealing

This section describes what happens to Al-oxide-Pb tunnel junctions during thermal annealing (79). By looking at junction resistance, barrier parameters (thickness, average barrier height, and the difference between the barrier heights at the Al and Pb electrodes), and inelastic electron tunneling (IET) peak intensities, one can study time-dependent effects occurring in the junction. One observes changes in the tunneling barrier and IET spectra indicating that surface hydroxyl groups (-OH) experience

reorientation.

The Al-oxide-Pb junctions used were prepared as described in Chapter 4.1. One should note that the insulating barrier formed in a plasma is not likely to be stoichiometric alumina, and may also contain other molecular species (such as -OH due to the presence of residual water in the bell jar system) besides pure aluminum oxide. The covering metal electrode (Pb) will perturb the barrier in at least two ways: the electrode may penetrate into the barrier (51, 92) or it may alter the orientation of surface groups, canting them somewhat. Also, due to the work functions of the two metal electrodes, a strong electric field will arise across the barrier (115). For an idea of field strength, a potential difference of 0.5 V (similar to differences in work functions) across a 10-Å junction (these are typical barrier thicknesses found using ellipsometry (80)) gives a field of  $5 \times 10^8$  V/m. This field can aid in group reorientation and ionic diffusion.

The thermal annealing experiments were carried out by removing a junction from liquid nitrogen temperature and keeping it at room temperature, about 20°C, for the desired length of time. To prevent the ice which formed on the tunnel junction electrodes (when removed from liquid nitrogen to room air) from melting and subsequently damaging the junction, annealing was carried out in a vacuum. All annealing times referred to are cumulative times (i.e., the total time for which the junction has been annealed).



The most obvious parameter which changes with annealing is the junction resistance  $R$ . Fig. 6.1 shows a plot of the resistance ratio  $R_t/R_0$  versus  $t$  (total annealing time) for a series of thermally annealed (open circuit) oxide junctions where  $R_0$  is the initial resistance (within a few minutes of junction formation), and  $R_t$  the resistance at time  $t$  (at  $-30$  mV). The curves suggest three regions: (1) an initial decrease (some curves drop below  $R_t/R_0 = 1.00$ ) in resistance (or none at all), (2) a rapid resistance increase which becomes (3) a more gentle increase.

Other noticeable changes occur in the conductance  $\sigma$  versus applied bias  $V$ , and in the IET spectrum  $d\sigma/dV$  versus  $V$ . The spectrum of an oxide (Fig. 6.2) shows two main peaks of interest, the 450 meV peak due to surface OH stretching, and an Al-O stretching mode at 118 meV due to the aluminum oxide (all peak positions referred to are for the polarities Al negative and Pb positive). Upon thermal annealing one sees noticeable changes in the spectrum of a particular junction: for example (Fig. 6.3), the OH peak at 450 meV increases in size and sharpens up slightly.

Changes also occur in the shape of the conductance curves. These curves are characterized by the barrier parameters (see Chapter 5.3)  $s$ , the average barrier thickness,  $\bar{\phi}$ , the average barrier height [ $\bar{\phi} = \frac{1}{2}(\phi_1 + \phi_2)$  at zero bias], and  $\Delta\phi = \phi_2 - \phi_1$ , the difference of the barrier heights at the two electrodes. For thermally annealed

Fig. 6.1

This figure shows a plot of  $R_t/R_0$  vs  $t$  for several junctions, where  $R_t$  is the junction resistance at time  $t$ ,  $R_0$  is the initial resistance and  $t$  is the total annealing time.

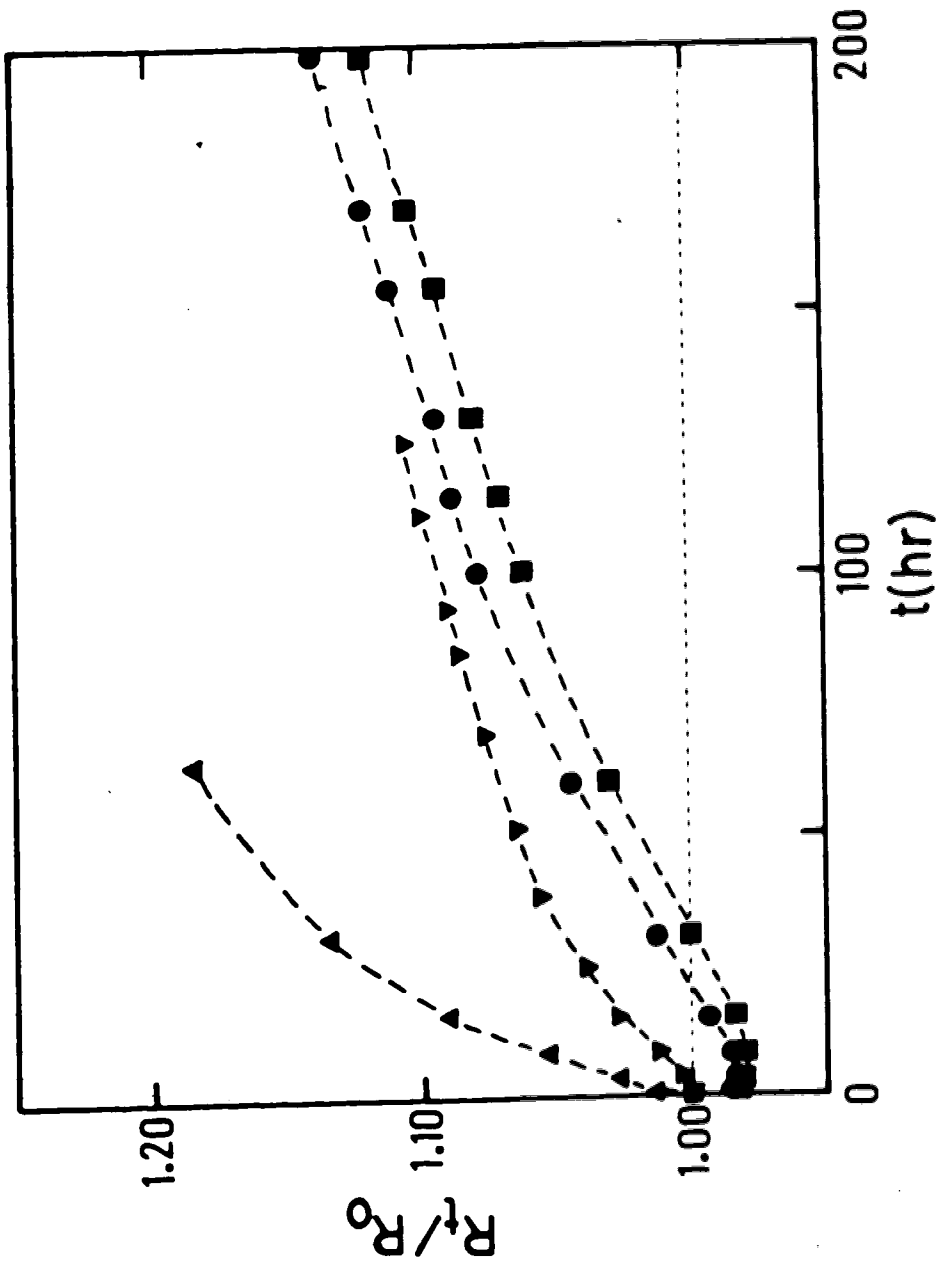


Fig. 6.2

A typical IET spectrum for an Al-Al oxide-Pb tunnel junction is shown. Peaks of interest occur at 118 meV and 450 meV.

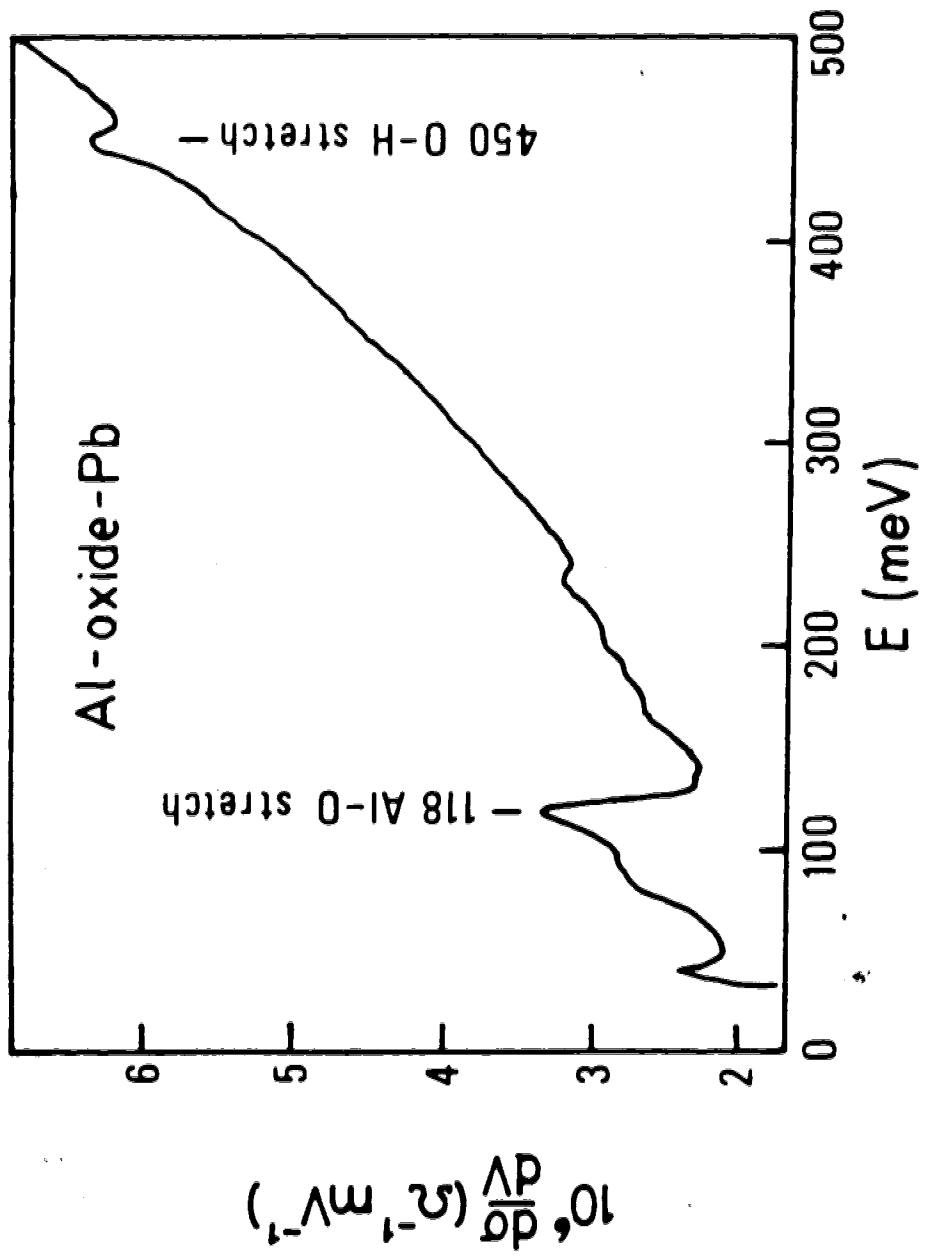
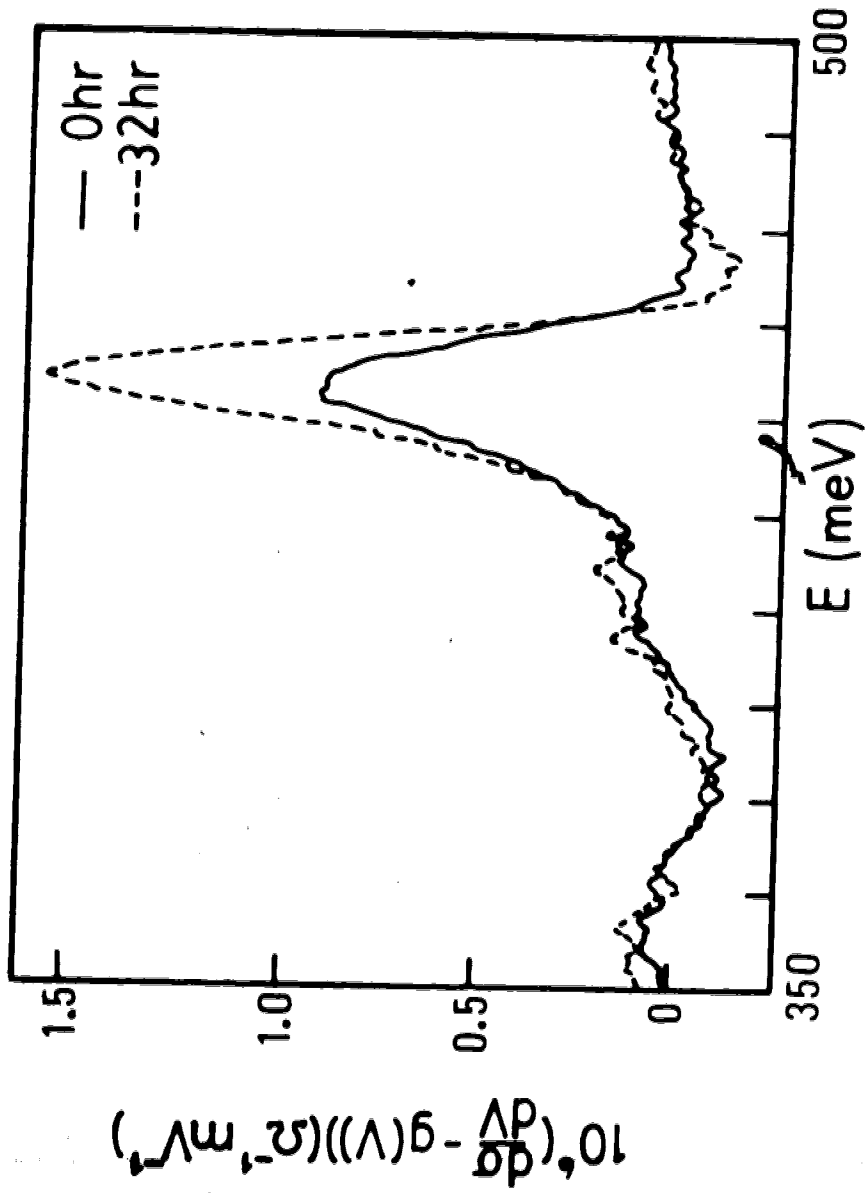


Fig. 6.3

The change in the 450 meV OH peak with annealing is shown here for two different times - 0 hour and 32 hours.



junctions, one finds that  $s$ , the effective barrier thickness, increases with time as shown in Fig. 6.4 (this does not mean the barrier is necessarily becoming physically wider but rather the tunneling resistivity is becoming greater), and that  $\bar{\phi}$ , the average barrier height, decreases with time. The most interesting results involve the barrier heights at the Al and Pb electrodes,  $\phi_1$  and  $\phi_2$  respectively. Figure 6.5(a) shows a decrease in  $\Delta\phi$  which levels off within 40 hours. In Fig. 6.5(b) one sees that  $\phi_1$ , the barrier height at the aluminum electrode, decreases and then levels off. This suggests that there has been an increase in positive charge density near the lead electrode. In conjunction with this barrier height behaviour, one finds that the intensity  $F(450)$  of the 450 meV surface OH stretching peak for this junction increases with time and tends to saturate.

Looking back over the results we find

- (1) a rapid 450 meV peak intensity increase to saturation,
- (2) a decrease in  $\Delta\phi$ ,
- (3) a decrease in  $\phi_2$  (the lead side of the junction becoming more positive),
- (4)  $\phi_1$  remains fairly constant for the aluminum electrode,
- (5) a slight sharpening of the 450 meV peak.

Since a large electric field may exist across the barrier ( $\sim 10^8$  V/m) a possible interpretation can be



Fig. 6.4

A plot of  $s$  vs  $t$  is shown for a thermally annealed junction, where  $s$  is the barrier thickness. These values of  $s$  should not be taken too literally as they are influenced by  $\bar{\phi}$  for their calculation as indicated in Eq. (2.5).

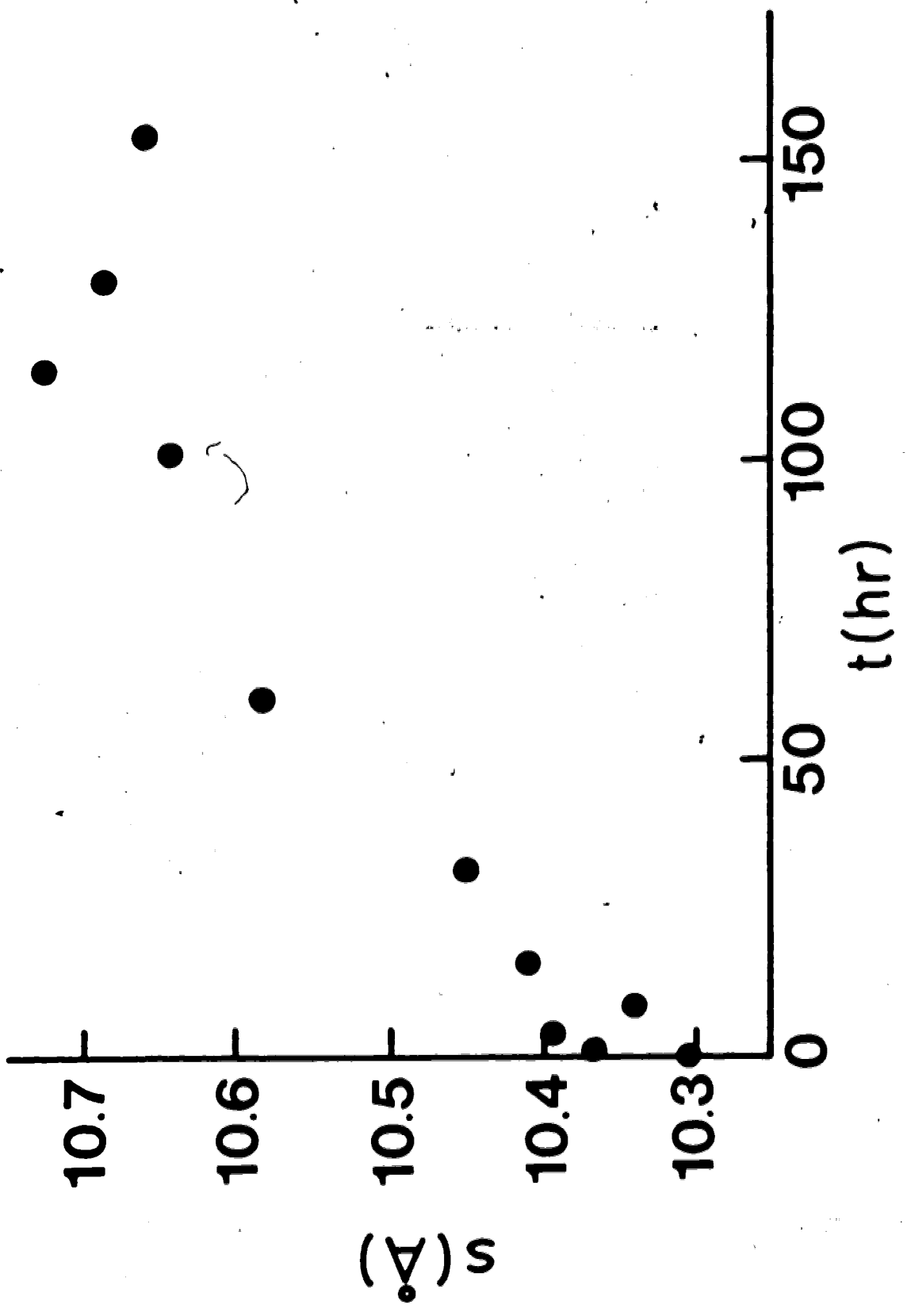
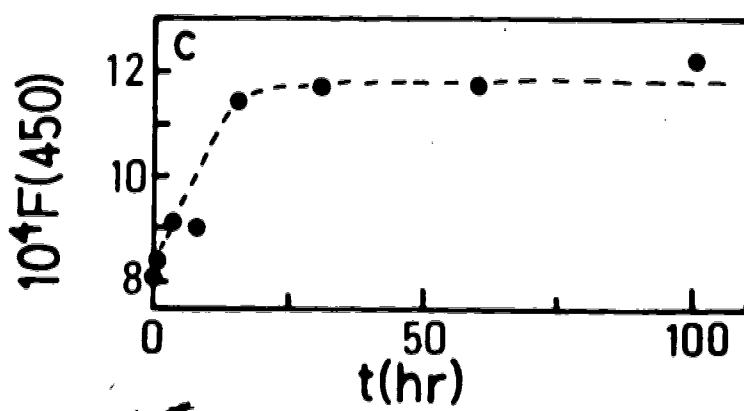
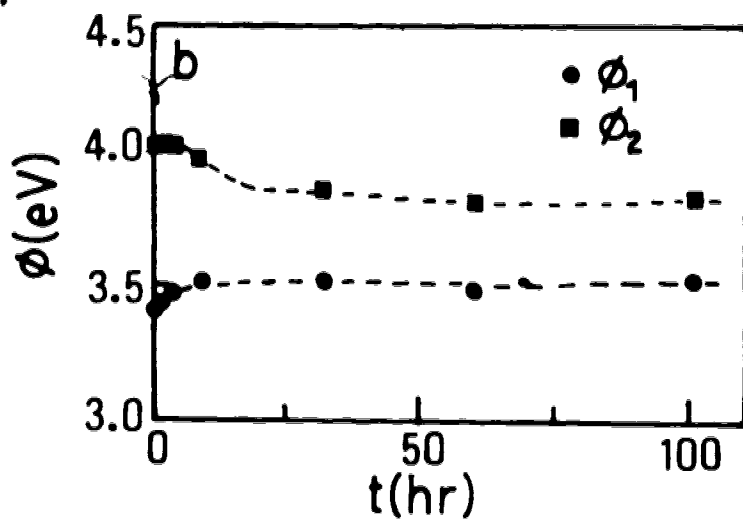
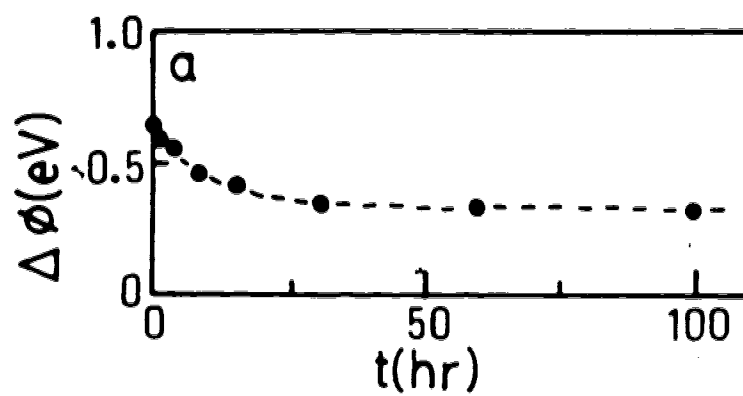


Fig. 6.5

Changes in  $\Delta\phi$ ,  $\phi_1$ ,  $\phi_2$ , and  $F(450)$  are shown. (a) A plot of the separation between barrier heights at the two electrodes,  $\Delta\phi$  vs total annealing time  $t$  shows the decrease of  $\Delta\phi$  with time. (b) This plot of the barrier heights at the two electrodes vs time shows a decrease at the Pb side ( $\phi_2$ ) but little change at the Al side ( $\phi_1$ ). (c) This graph shows how the 450 meV peak intensity,  $F(450)$  increases with annealing time and finally levels off.



given by considering the reorientation of the surface hydroxyl groups on the aluminum oxide. The above mechanism is shown schematically in Fig. 6.6(a) where the originally quite randomly aligned OH groups reorient themselves under the influence of the electric field.

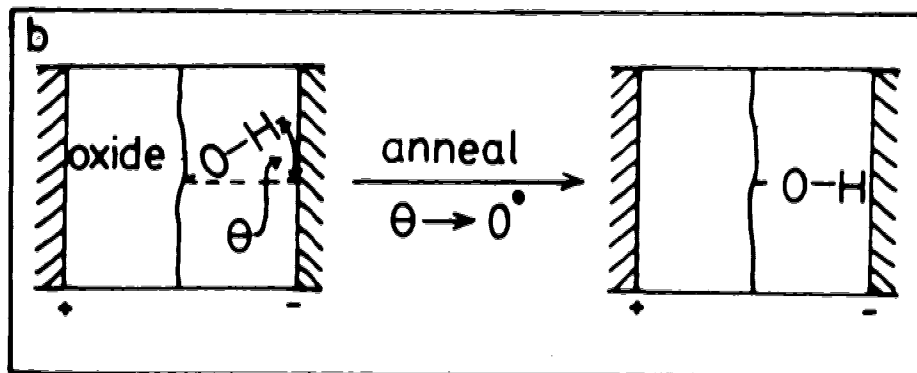
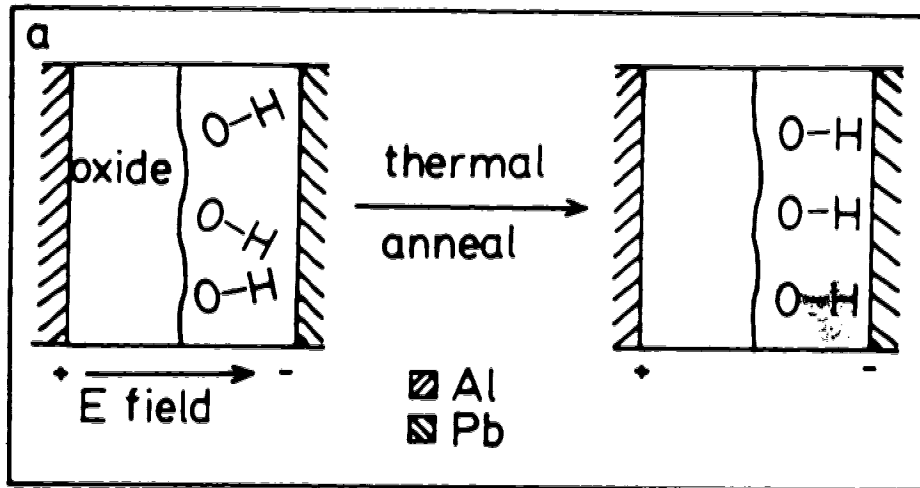
Fig. 6.6(b) shows that, in realigning the OH dipole,  $\theta$  (the average angle of an OH group from the normal to the plane of the Pb electrode) tends to  $0^\circ$ , i.e. the OH stretch motion is more perpendicular to the Pb electrode. This will result in an intensity increase for this mode proportional to  $\cos^2\theta$  for a stretching mode (110).

Secondly, Fig. 6.6(b) shows that with reorientation the positive hydrogen of the OH moves closer to the lead electrode, increasing the positive charge density near it; therefore  $\phi_2$  decreases while practically no effect is exerted on  $\phi_1$  at the Al side.

One also finds that upon annealing, the intensity of the 118 meV peak due to Al-O stretching increases in a manner similar to the 450 meV peak increase. By looking at the intensity-vs-annealing time curves (Fig. 6.7(a) for a few junctions, one can see that the lower the initial 118 meV intensity the greater the annealing effect. Whereas the 118 meV peak intensities tend to saturate at different values, the 450 meV intensities all tend to saturate at approximately the same value [Fig. 6.7(b)]. This suggests that there is a certain "monolayer" coverage of surface OH for all junctions (each of which has its own

Fig. 6.6

- (a) A schematic representation of the tunnel barrier shows how the OH groups reorient under the influence of an electric field during thermal annealing.
- (b) Here, a close-up view shows how  $\theta$  decreases with reorientation and results in the hydrogen side of the OH group moving closer to the Pb electrode.



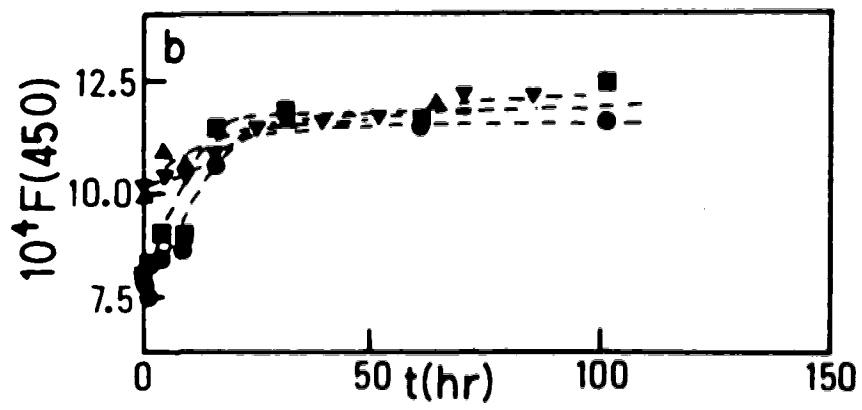
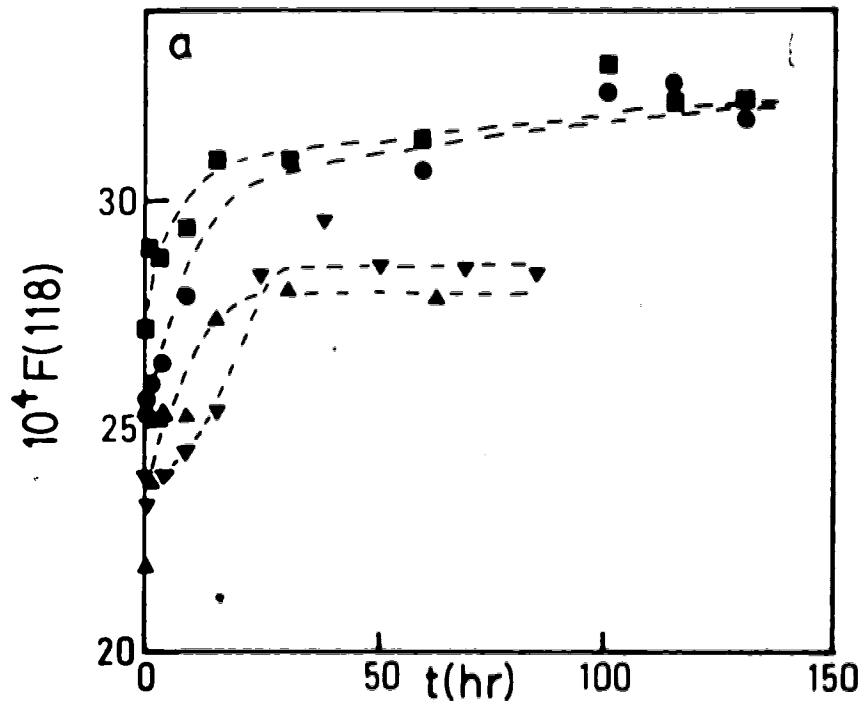
6

Fig. 6.7

(a) A plot of the 118 meV (Al-O) intensity vs annealing time for several tunnel junctions.

(b) This graph of the 450 meV (O-H) intensity vs annealing time for several tunnel junctions shows that for all the samples the same saturation intensity is reached.





particular initial orientation) while the amount of aluminum oxide can vary [Fig. 6.7(a)].

To summarize, it is found that Al-oxide-Pb tunnel junctions subjected to thermal annealing undergo resistance changes (up and down) as well as changes in barrier parameters and IET peak intensities with time. This suggests a reorientation of the surface hydroxyl groups under the influence of an inherent electric field of polarity such that the Al side is positive and the Pb side is effectively negative. Also, by looking at the values at which the IET peak intensities saturate, one deduces that there is a certain monolayer coverage of surface OH for all the junctions while the amount of aluminum oxide varies.

### 6.3. Voltage Annealing

Chapter 6.2 has described some of the effects which occur in Al-oxide-Pb tunnel junctions when they are thermally annealed (at room temperature). This section describes the results of voltage annealing (80). In this, a constant voltage is applied across the junction electrodes to produce an electric field which adds to or subtracts from the junction's intrinsic electric field. This intrinsic field is responsible for some of the changes observed in thermal annealing; thus, altering the field with an applied bias should help to clarify our knowledge of the annealing process. Information about junction resistance, barrier parameters, and inelastic electron

tunneling (IET) peak intensities indicates that positive charge at the Al-oxide interface can be increased or decreased, depending upon the polarity of the applied bias. Also, by proper choice of bias polarity, junction aging (i.e. any changes occurring within the junction after its completion) can be retarded.

The Al-oxide-Pb junctions used were prepared as previously described such that two "identical" junctions were made on each substrate. In this way, one junction of the pair served as a control (thermally annealed only) while the other junction was subjected to voltage annealing. The voltage annealing experiments were carried out at room temperature in a vacuum. The control junction was allowed to undergo thermal annealing (open circuit) while the other junction of the pair was biased at the desired voltage and polarity. The biasing arrangement with the Al electrode positive, Pb negative shall be referred to as forward polarity (FP) and Al negative, Pb positive as reverse polarity (RP). Previous thermal annealing experiments showed that the intrinsic field of a junction was of forward polarity.

Again, interpretation of the annealing results is carried out by examining changes in junction resistance, barrier parameters, and inelastic electron tunneling peak intensities with respect to total annealing time. In addition to those exhibited by thermally annealed junctions, voltage annealed junctions showed several new effects.

Junctions biased at 0.5 V with forward polarity (Al positive, Pb negative) show an increase in the slope of the resistance versus annealing time curves shortly after the desired voltage is applied. In Fig. 6.8 a graph of  $R_t/R_b$  versus time  $t-t_b$  (where  $R_t$  is the junction resistance at time  $t$ ,  $R_b$  is the resistance at the time of bias application  $t_b$ , and  $t$  is the total annealing time) illustrates this resistance increase for several junctions of different ages when initially biased. One sees that the increase soon slows down again and that the net resistance ratio increase after, say 50 hours of application of the bias, diminishes the older the junction was to start with.

Another noticeable change is that which occurs in  $\phi_1$  and  $\phi_2$ , the barrier heights at the Al and Pb electrodes, respectively (depending on the nature of the sample,  $\phi_1$  can be greater or smaller than  $\phi_2$ ). Following application of an annealing bias, it is found that  $\Delta\phi = \phi_2 - \phi_1$  increases in time and finally levels off as shown in Fig. 6.9 by  $\Delta\phi - \Delta\phi_b$  versus  $t-t_b$  ( $\Delta\phi_b$  refers to the value of  $\Delta\phi$  at time  $t_b$ ). It is seen that an age dependence is also exhibited by the magnitude of the effect. One should note that it is  $\phi_1$  which decreases markedly while  $\phi_2$  changes only a little. This implies that the insulating barrier at the aluminum electrode acquires positive charge with time which eventually saturates as long as the biasing voltage is maintained. This charge, moreover is trapped

Fig. 6.8

This figure shows a plot of  $R_t/R_b$  vs  $t-t_b$  for three junctions biased at 0.5 V FP.  $R_t$  is the junction resistance at time  $t$ ,  $R_b$  is the resistance at the time of bias application  $t_b$ , and  $t$  is the total annealing time. For the circles, squares, and triangles  $t_b = 0, 212, \text{ and } 324 \text{ hr. respectively.}$

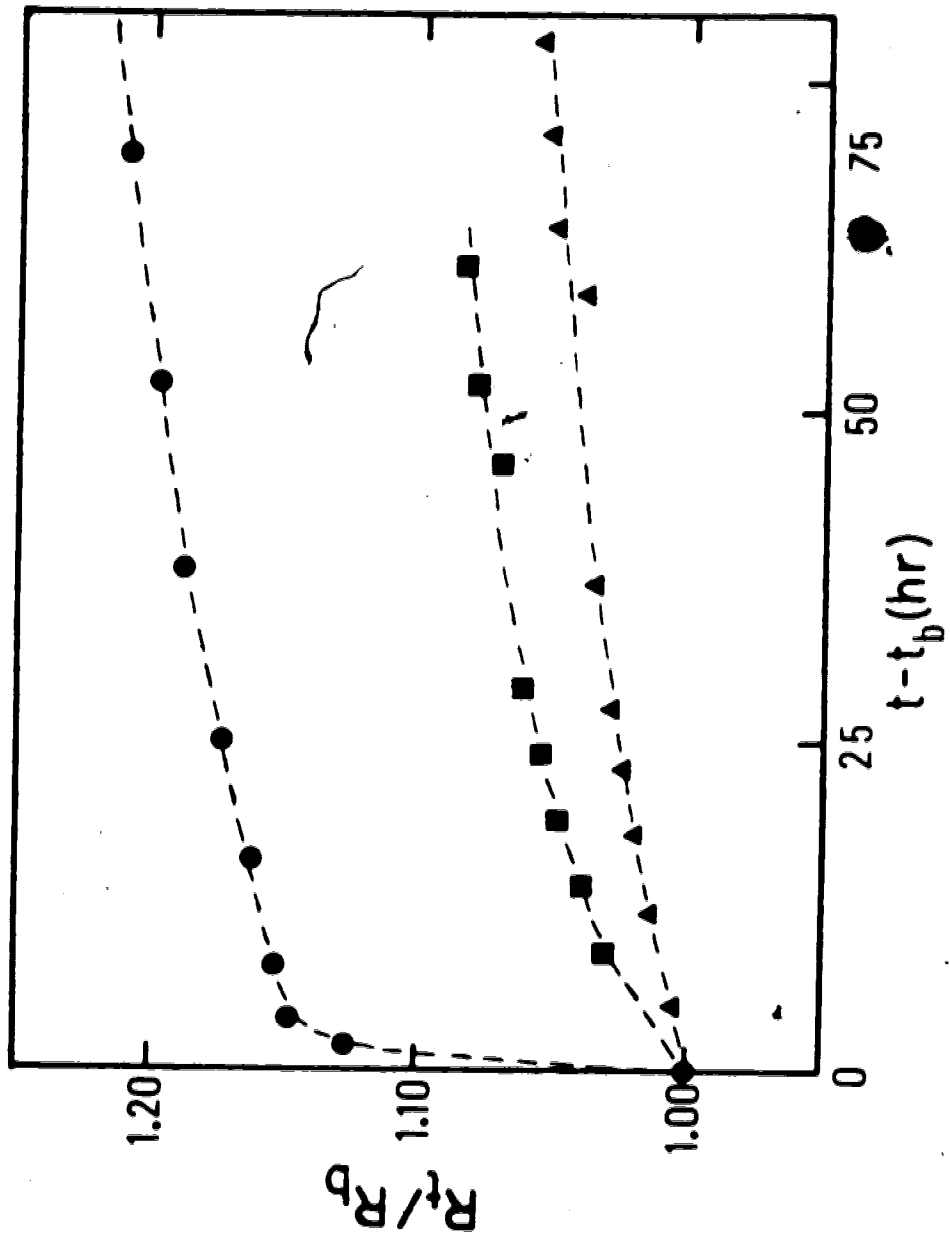
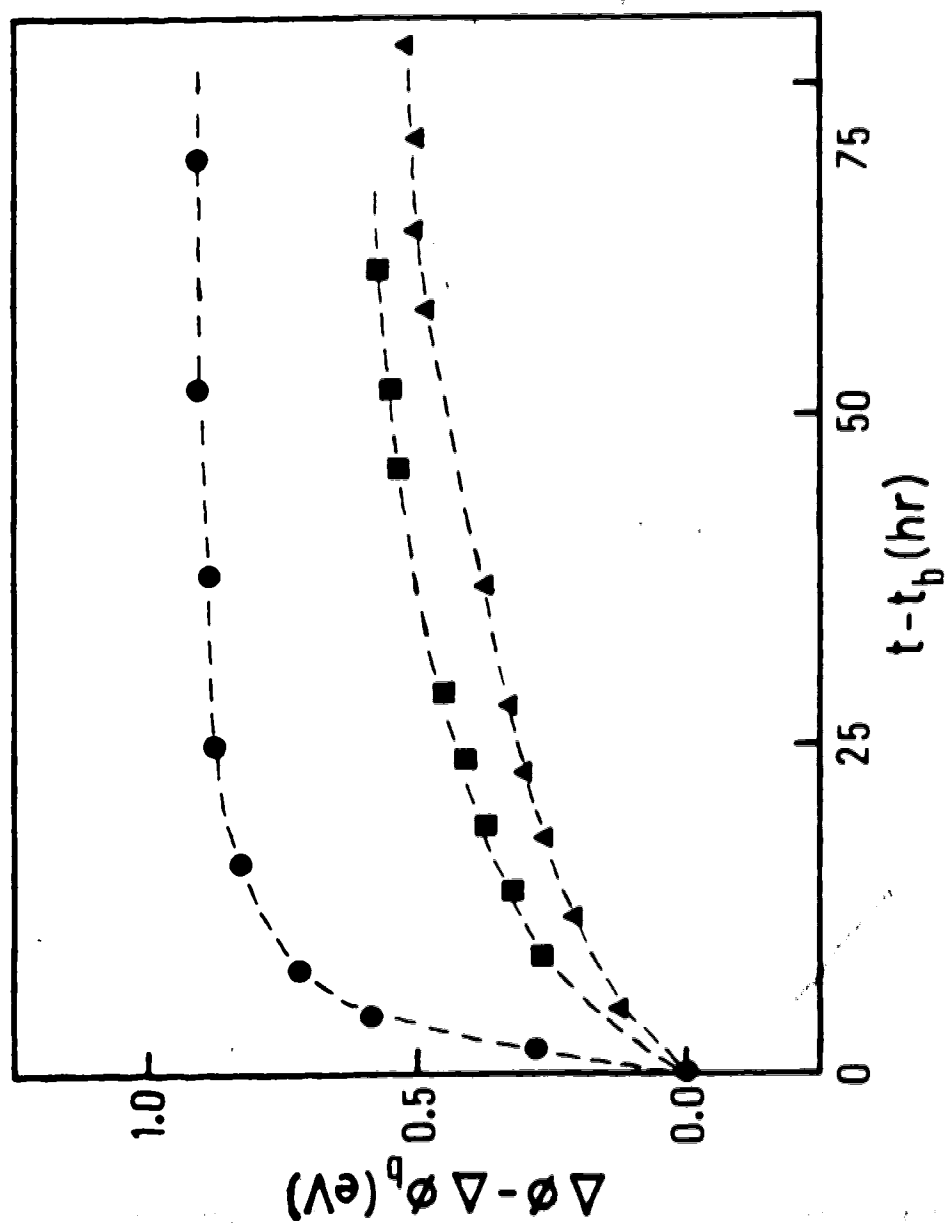


Fig. 6.9

A plot of  $\Delta\phi - \Delta\phi_b$  versus  $t - t_b$  for three junctions shows the effect of a 0.5 V FP bias on  $\Delta\phi$ , the difference of the barrier heights at the two electrodes. The junction age when biased,  $t_b$ , equals 0, 212, and 324 hr. for circles, squares, and triangles respectively.  $\Delta\phi_b$  is the value of  $\Delta\phi$  at time  $t_b$ .





just within the barrier otherwise, like a capacitor, it would drain off as the annealing voltage was reduced to zero.

If junctions are annealed using reverse polarity (Al negative, Pb positive) at 0.5 V, the results are different. Looking at  $R_t/R_0$  versus  $t$  ( $R_0$  is the resistance at  $t = 0$ ), one finds an initial decrease in resistance which eventually increases slowly (Fig. 6.10). In addition, the barrier height,  $\phi_1$ , at the Al electrode goes up (implying that the Al side has become less positive) while that at the Pb electrode,  $\phi_2$ , remains constant.

These resistance changes as well as the behaviour of  $\phi_1$  (Fig. 6.11) and  $\phi_2$  for a biased junction suggest movement of positive Al ions into and out of the barrier at the Al-oxide interface. When forward polarity is utilized, aluminum ions may be created at the aluminum electrode and drift a short way into the oxide barrier under the influence of the applied field. Such an occurrence raises the amount of positive charge near the Al electrode ( $\phi_1$  thus decreases) and increases junction resistance since the inclusion of Al ions within the oxide makes the barrier denser near the Al-oxide interface. On the other hand, application of a reverse polarity bias causes an initial resistance decrease and an increase in  $\phi_1$ . This indicates that some already existing positive charge is moved out of the barrier, which is reasonable since a negative potential has now been applied at the Al side.

Fig. 5.10

The resistance behaviour,  $R_t/R_0$  versus  $t$  is shown here for a junction biased at 0.5 V RP (circles), and a thermally annealed control junction (squares).

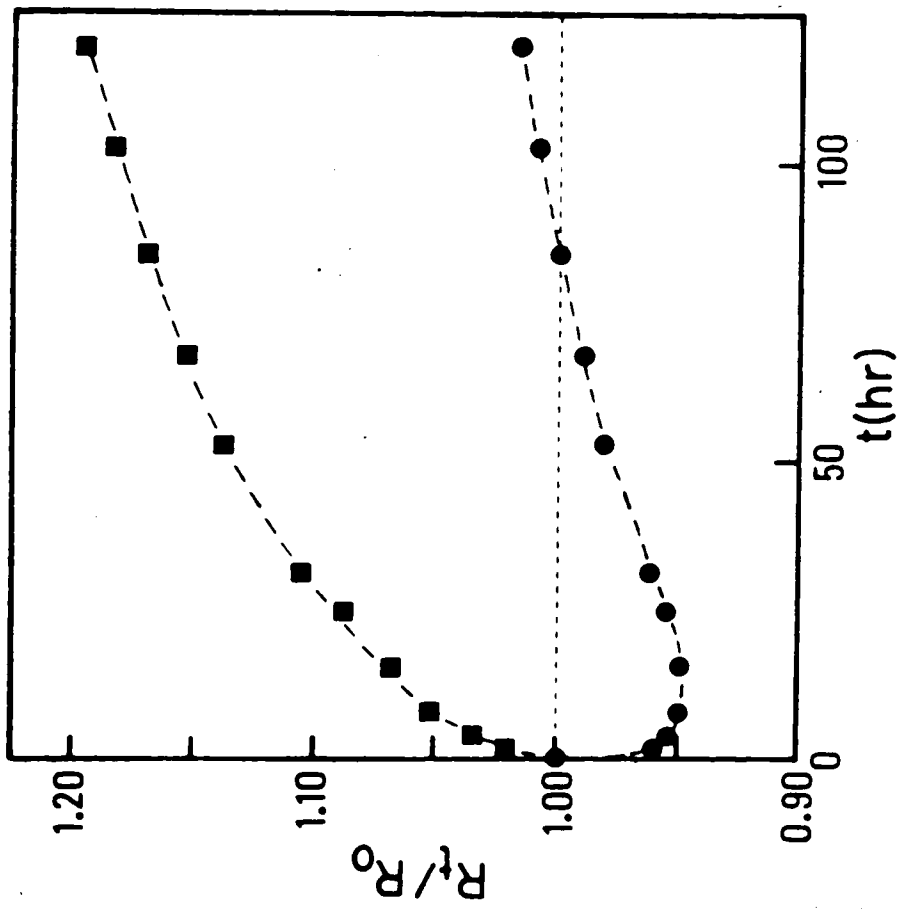
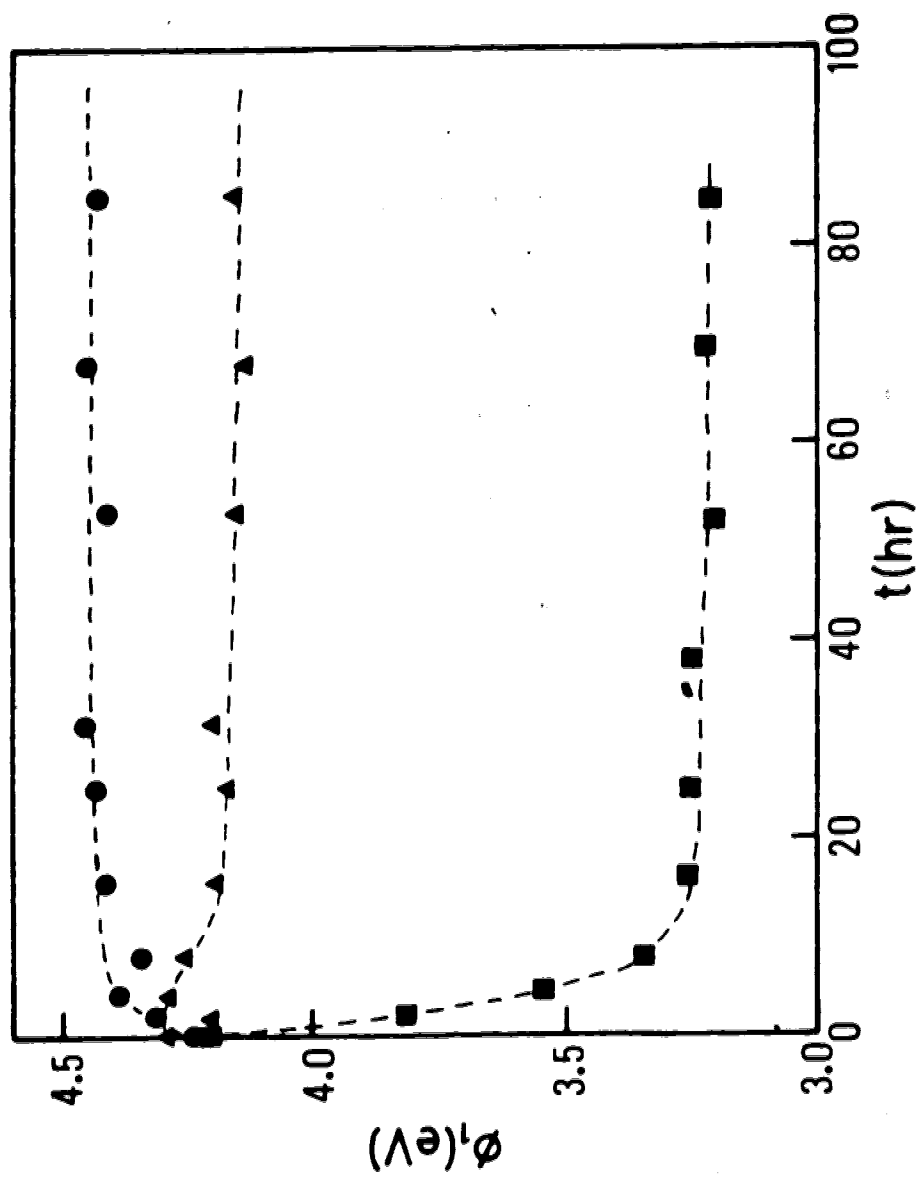


Fig. 6.11

This figure illustrates the behaviour of the barrier height at the Al electrode,  $\phi_1$  vs time for junctions subjected to 0.5 V RP (circles), 0.5 V FP (squares), or thermal annealing only (triangles).



One can account for the age dependence of the amount of change in  $R_t/R_p$ , and in  $\Delta\phi$  by noting the behaviour of a voltage annealed (FP) junction once the annealing bias is removed. Fig. 6.12 shows what happens. A decrease in  $\Delta\phi$  [Fig. 6.12(a)] occurs and  $\phi_1$  increases suggesting that the amount of positive charge near the Al electrode is being depleted. Looking now at the junction's resistance curve [Fig. 6.12(b)], it is seen that as charge depletion occurs, resistance increases. This leads one to believe that Al ions are being neutralized, and remain within the barrier as opposed to drifting back out to the Al electrode. The age effect can now be explained as follows. As a junction anneals, Al ions are created and drift into the junction due to its intrinsic field or under the influence of an externally applied field. The ions, once having entered the barrier are eventually neutralized and new ions can be formed (maintaining a type of dynamic charge equilibrium). As a junction ages, vacancies for new ions to occupy within the insulator are diminished since some have already been filled. Thus, when an external bias is applied to an old junction as opposed to a newer one, its response is not as great simply because there are not as many vacancies in the barrier for new Al ions to fill and produce their effects. This is illustrated in Fig. 6.13. On the subject of aging, one finds that junction aging can be suppressed by the application of a reverse polarity bias. This will be discussed later.

Fig. 6.12

(a) Here we see the decrease in  $\Delta\phi$  after the removal of a 0.5 V FP bias. The arrow indicates the beginning of thermal annealing.

(b) The resistance ratio behaviour,  $R_t/R_o$ , of a junction during voltage annealing (0.5 V FP) and then thermal annealing (starting at the arrow) is shown.

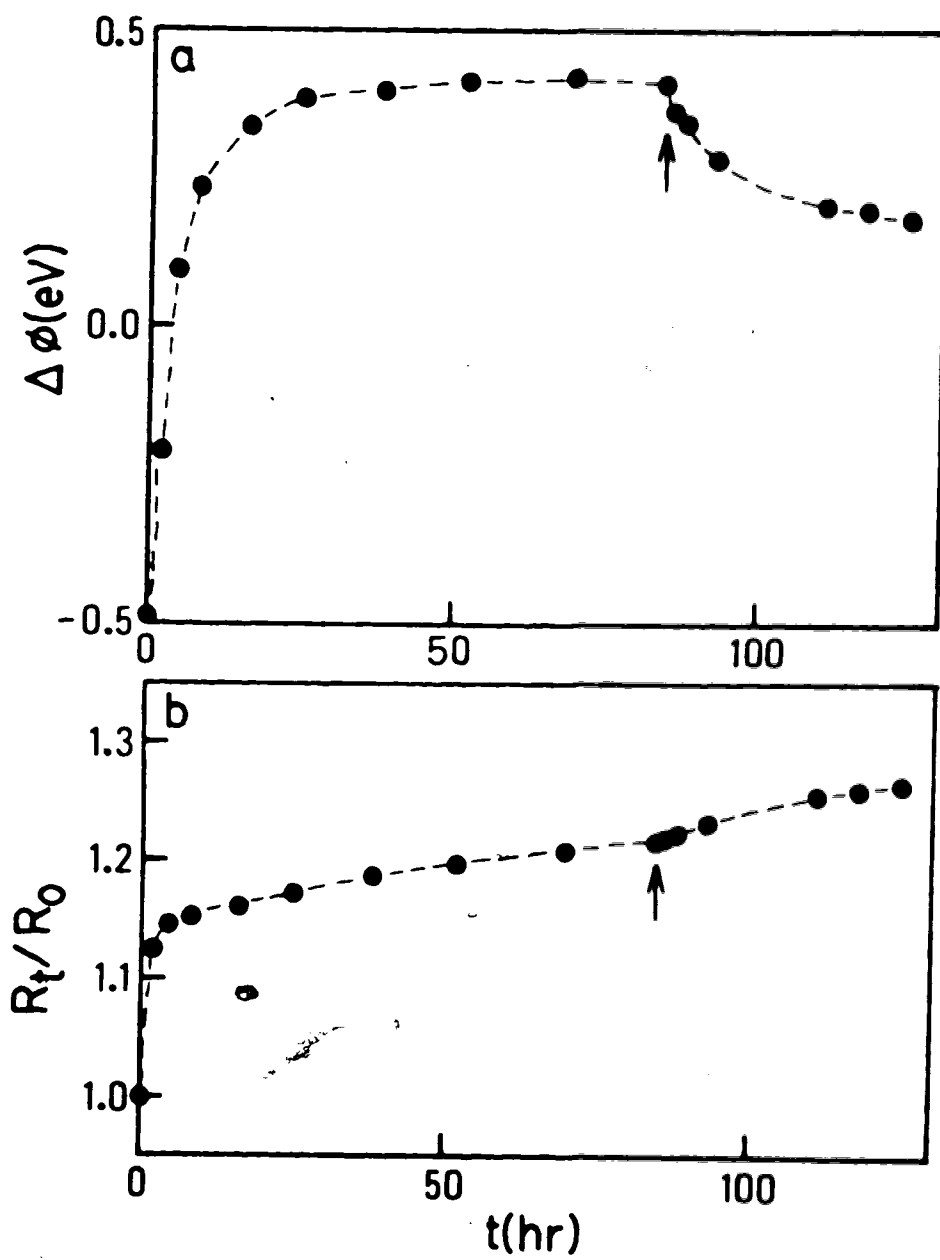
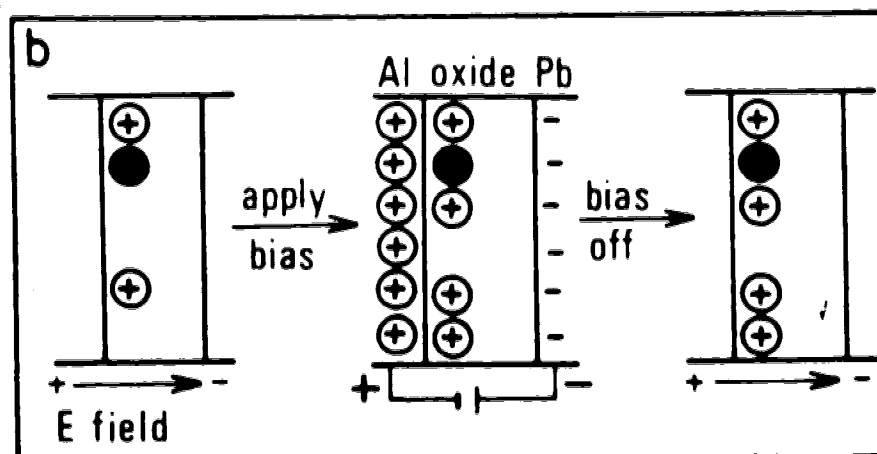
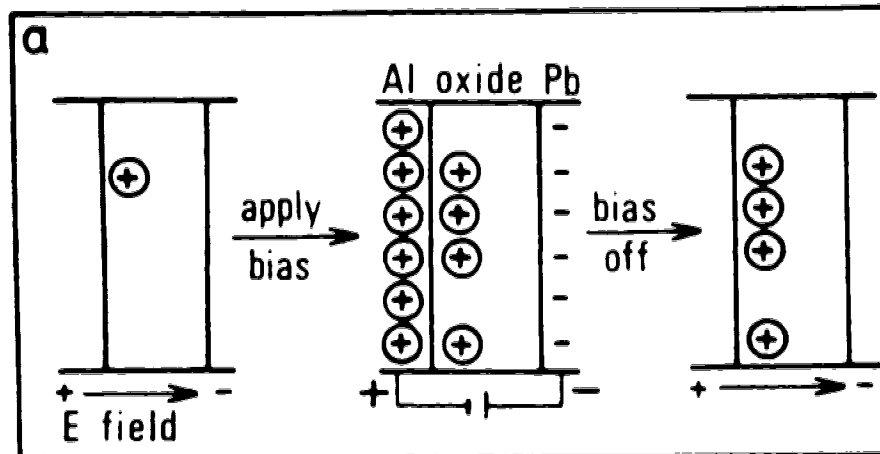




Fig. 6A13

(a) This figure shows the response of a "young" junction to FP biasing. In the first picture many vacancies exist at the Al-Al oxide interface. When a bias is applied (second picture) ions are created and can drift into the barrier to fill the vacancies. They remain trapped here after the bias is removed (picture three). (b) Here, the response of an "old" junction to FP biasing is shown. Vacancies are filled in the same way as described in (a) except that there are fewer vacancies to begin with. Circles with + signs represent Al ions, and shaded-in circles denote Al atoms.

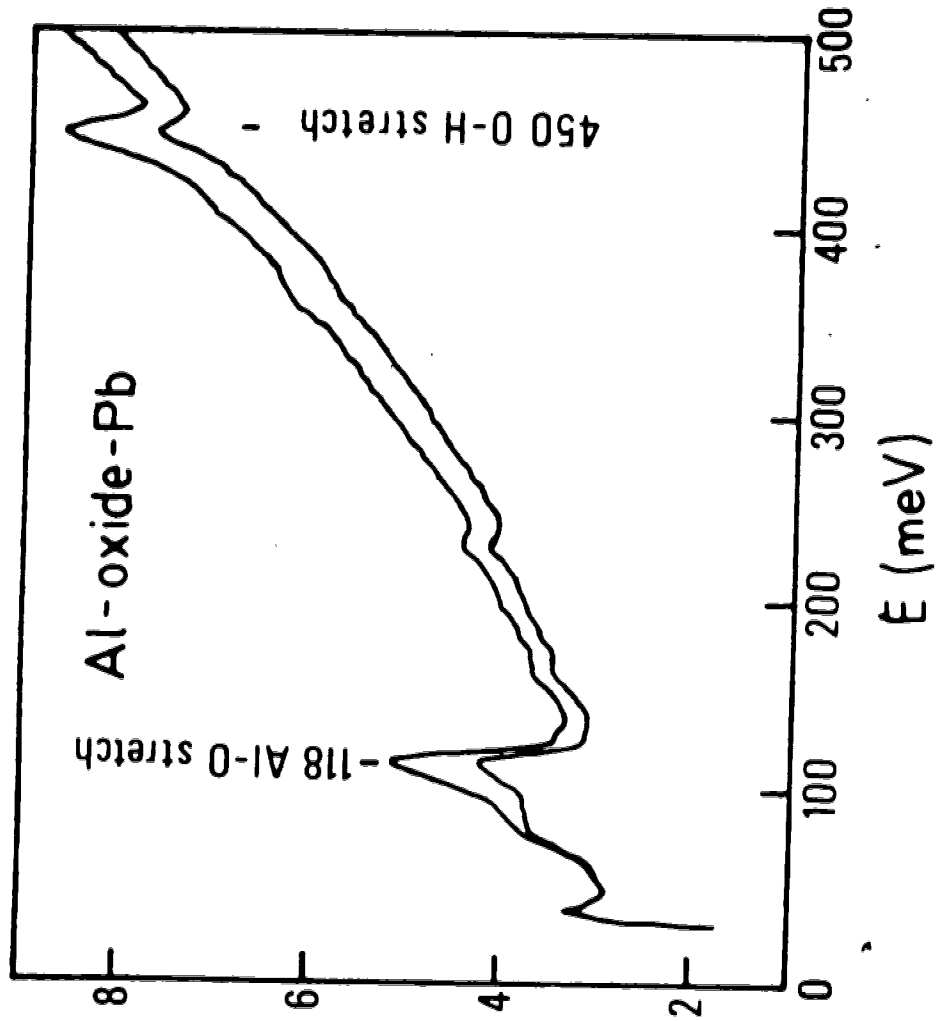


Now, one turns to see what effects voltage annealing has on IET peak intensities. Looking at an aluminum oxide spectrum (Fig. 6.14) one notes the usual peaks of interest at  $\sim 118$  and  $450$  meV due to Al-O and O-H stretching respectively. When voltage annealing is carried out with a  $0.5$  V FP bias, one finds the  $118$  and  $450$  meV peak intensities increase with time to values greater than those in the thermal annealing case. This suggests that with an electric field greater than the intrinsic field alone, the surface hydroxyl and aluminum oxide may experience further reorientation. On the other hand, the application of a field of  $0.5$  V RP is found to inhibit the change in peak intensities which normally occurs in virgin junctions under the influence of their intrinsic field (Fig. 6.15). This implies that the intrinsic field of the junction is neutralized by the  $0.5$  V RP bias, thereby leaving no electric field across the junction to reorient the molecular groups within. If the bias is now removed, the junction thermally anneals as before; resistance and peak intensities increase. By applying such a reverse field to neutralize the intrinsic field, one can thus delay the aging of a tunnel junction.

Having looked at the voltage annealing behaviour, one can now use it to aid in explaining some results observed in the thermal annealing experiments. A number of thermally annealed junctions initially showed an unexplained drop in junction resistance similar to the one

Fig. 6. 14

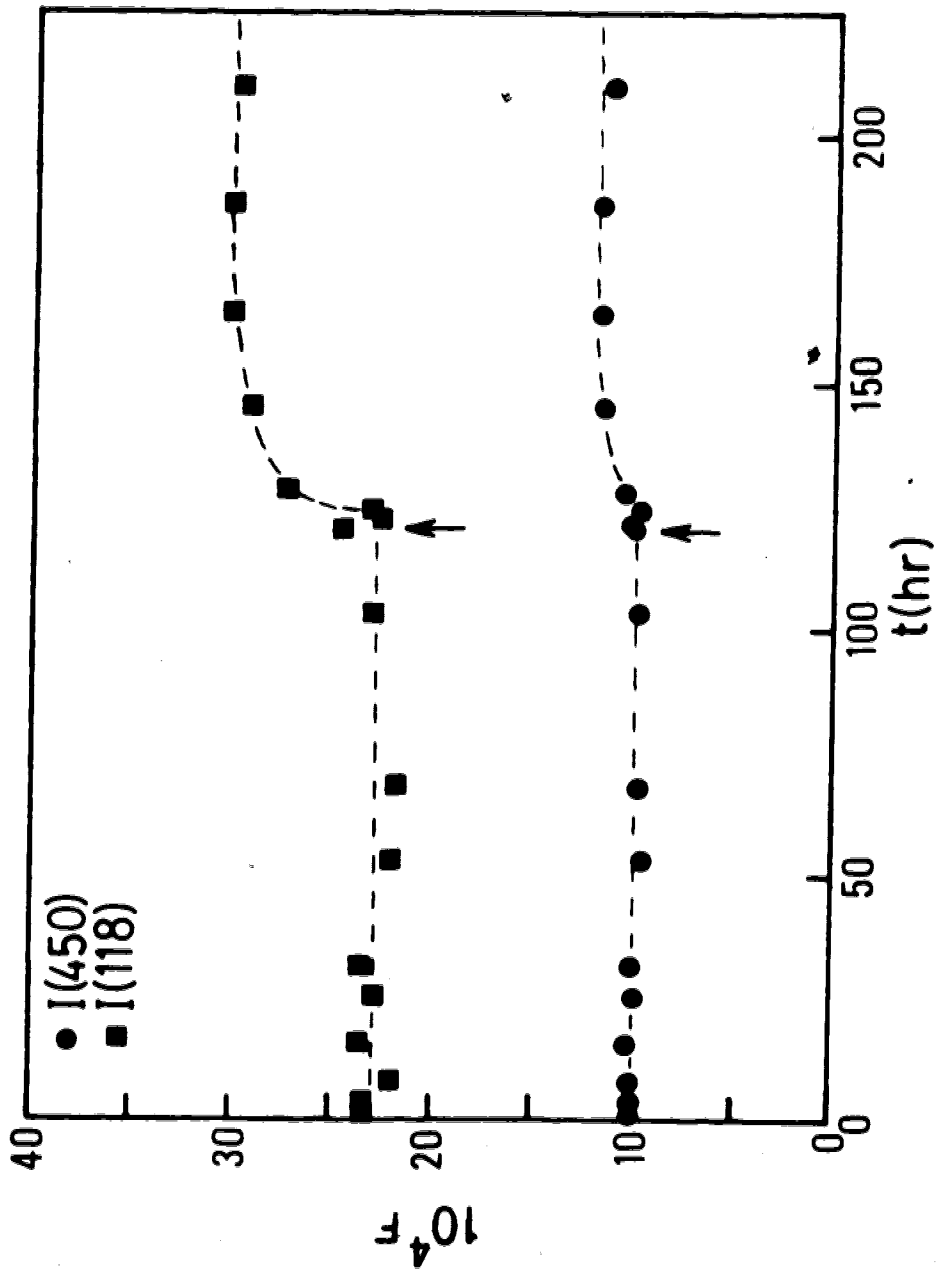
The two curves are IET spectra for an Al-Al oxide-Pb junction at two different times. The upper curve shows the effect that 70 hours of 0.5 V FP voltage annealing has on the virgin sample (lower curve).



$$10^4 \frac{1}{N} \frac{dI}{dV} (\text{mV}^{-1})$$

Fig. 6.15

This plot of peak intensity,  $F$  versus time shows how reverse polarity annealing (0.5 V) suppresses any changes in  $F$  (from 0 - 120 hours). If the bias is removed (at the arrow), the junction thermally anneals and peak intensities increase.

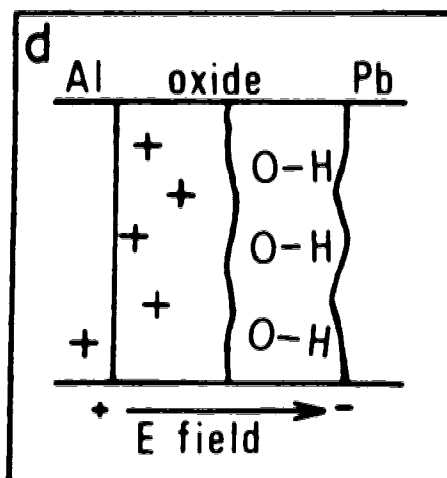
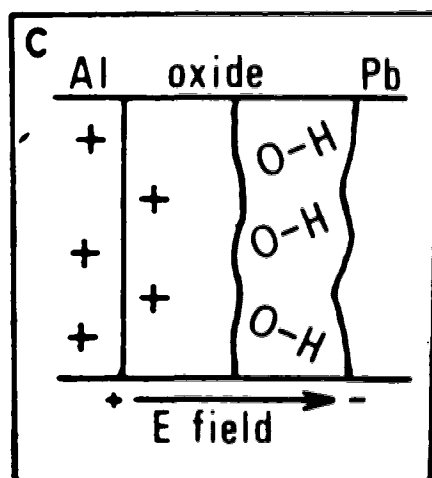
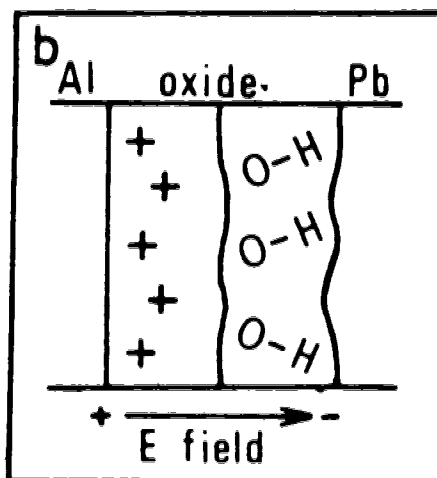
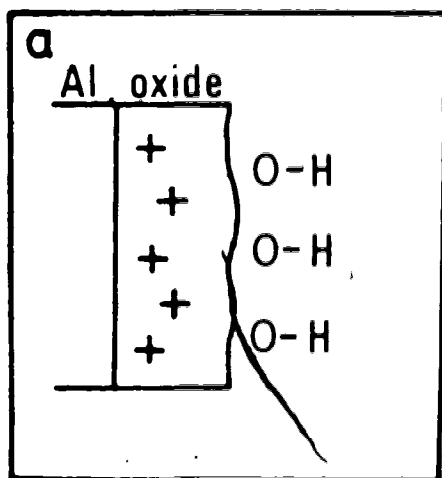


observed in voltage annealing with reverse polarity. Unlike RP voltage annealing the peak intensities increased in the usual way. A close look now at  $\phi_1$  for those junctions with a pronounced resistance dip shows that  $\phi_1$  initially increases a little (Al side becoming more negative). This, as well as the resistance drop, could be accounted for if positive Al ions left the barrier. However, since the intrinsic field of the junction has the Al electrode positive, there seems to be a contradiction unless one considers what may occur in the course of junction fabrication. Looking at the barrier during growth, one might imagine it to be aluminum oxide with positive Al ions near the aluminum electrode and OH groups standing up on the growing alumina surface [Fig. 6.16(a)]. Subsequent evaporation of the Pb cover electrode will tend to squash the OH groups, leaving them canted as shown in Fig. 6.16(b). This movement of the OH group's hydrogen closer to the oxide will cause a greater electrostatic repulsion between the aluminum ions and the hydroxyl hydrogens than existed prior to the deposition of the Pb cover electrode. Since the Al ions are smaller and more mobile than the OH groups, the mutual electrostatic repulsion can force some ions out of the barrier [Fig. 6.16(c)]. This takes place only until the intrinsic field of the junction can reorient the OH groups sufficiently to relieve the repulsive force. At this point, Al ions under the influence of the intrinsic field



Fig. 6.16

This figure shows how evaporation of the Pb electrode on the growing oxide can perturb the surface hydroxyl groups and cause expulsion of Al ions out of the barrier due to electrostatic repulsion.



are once more able to enter the barrier [Fig. 6.16(d)] and cause resistance increases. Some thermally annealed junctions show the above behaviour; some do not. Factors influencing this probably include (1) the manner in which the Pb electrode is evaporated and (2) the number and distribution of Al ions within the oxide.

In this section, a new technique for the study of ion motion and behaviour within tunnel junctions has been introduced. By applying a 0.5 V FP annealing voltage to a junction, one causes positive charges, presumably aluminum ions to accumulate at the Al-oxide interface. These ions serve to increase  $\Delta\phi$  ( $\phi_1$  decreases) as well as the junction resistance. When the voltage is removed, neutralization of ions within the barrier is reflected by the fall of  $\Delta\phi$  ( $\phi_1$  now increases). The accumulated charge also serves to enhance the junction's intrinsic electric field which further aids group reorientation. On the other hand, when a 0.5 V RP bias is applied, some positive charge is removed from the barrier and junction resistance initially falls. It rises slowly afterward, perhaps due to neutralization of some remaining charge within the barrier. Peak intensities do not change because the magnitude of the bias seems sufficient to negate the junction's intrinsic field, thereby leaving no electric field to reorient molecular groups. Junction aging is thus postponed until the reverse polarity bias is removed, at which point normal thermal annealing occurs.

Finally, an explanation for the resistance dip observed in some thermally annealed junctions has been suggested as due to a temporary electrostatic repulsion occurring between Al ions and the H of surface hydroxyl groups after the Pb cover electrode has been evaporated.

#### 6.4. Voltage Annealing with Alternating Polarity

Having studied annealing with an applied voltage of given polarity, attention is now turned to the effects of voltage annealing in which the polarity of the applied bias is reversed for each annealing period of time  $t_p$ . Such annealing is referred to as voltage annealing with alternating polarity. This is done in order to see whether any of the annealing effects brought about by a voltage of given polarity can be reversed by applying a voltage of opposite polarity for the same duration of time. Although more work needs to be done, some results can be shown.

For this experiment we use two Al-aluminum oxide-Pb tunnel junctions grown on the same aluminum base layer. The tunneling characteristics of the virgin junctions are first measured. Following this, the control is thermally annealed, while the other junction is subjected to a bias of either polarity for a time  $t_p$ . As in the previous section, we refer to the polarity with the Al electrode positive, Pb negative as forward polarity (FP) and Al negative, Pb positive as reverse polarity (RP).

At the end of an annealing period, the two junctions are cooled and their tunneling characteristics are again measured at 4.2 K in liquid helium. Changes occurring in the tunnel junctions are studied with respect to the total annealing time,  $t$ .

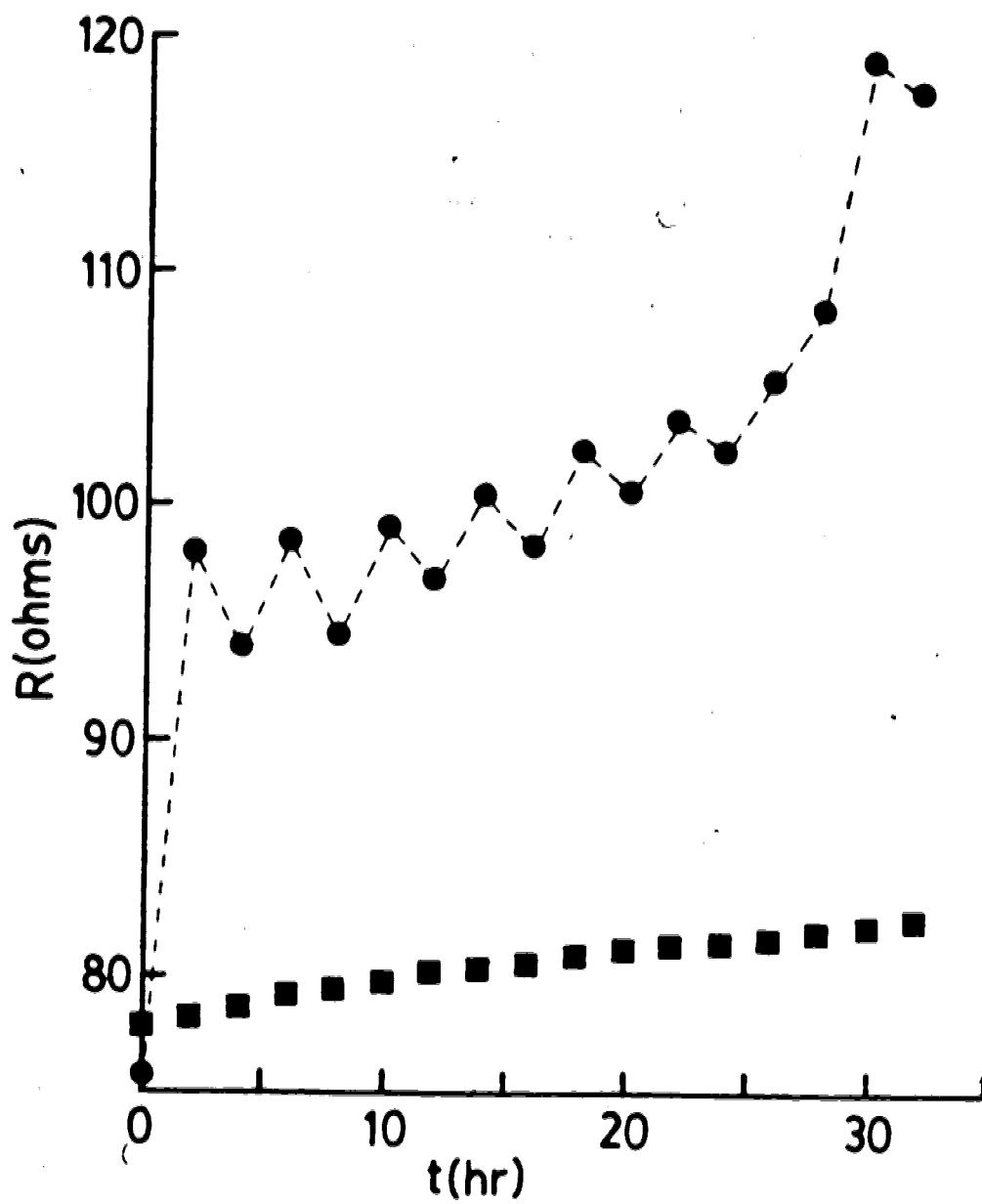
Previous results with voltage annealing (80) showed that the application of a room temperature annealing voltage of forward polarity could force positive charge into the junction at the Al-Al oxide interface, some of which was neutralized within the junction. Also, a reverse polarity voltage was able to draw a small amount of positive charge out of the barrier. This, along with other information suggested that some of the charge was fairly mobile - it could be moved in and out of the barrier easily - while another portion became trapped within the insulating barrier.

To explore this further it was decided to apply a voltage of forward polarity to a virgin junction for time  $t_p$  in order to move charge at the aluminum electrode in toward the junction interior. After that time a reverse polarity voltage would be applied for time  $t_p$  again to try and counteract the effect of the previous voltage anneal, thereby moving charge back to the aluminum electrode.

Figure 6.17 shows the resistance behaviour of a junction for which this has been done. The voltage magnitude was 1 volt and the annealing period  $t_p$  was 2

Fig. 6.17

The resistance behaviour for an alternating polarity voltage annealed junction. Here, the magnitude of the voltage is 1 volt and the annealing period  $t_p$  is 2 hours. The thermally annealed control is shown below (squares).



hours. One sees a large resistance increase in the first two hours. Application of the reverse polarity voltage causes a comparatively small resistance decrease, while subsequent application of the forward polarity voltage again, causes a small resistance increase. As can be seen, resistance goes up or down depending upon the polarity of the applied annealing voltage with a general trend of overall resistance increase. One also notes that the size of the up or down swing decreases with time. The thermally annealed control is also shown.

In Fig. 6.18, the behaviour of  $s$ , the calculated barrier thickness is shown. The first 2 hours exhibit a large change in thickness while subsequent changes are smaller, and again increase or decrease depending upon the annealing voltage polarity.

Fig. 6.19 illustrates the behaviour of  $\phi_1$  and  $\phi_2$ . Looking first at  $\phi_1$ , the barrier height at the Al-aluminum oxide surface, we see that with a forward polarity bias,  $\phi_1$  drops dramatically in the first two hours indicating an increase of positive charge at this interface. Subsequent application of a reverse polarity bias causes  $\phi_1$  to increase somewhat, suggesting a decrease in the amount of positive charge at the interface. Further annealing with opposite polarities again results in an oscillatory behaviour in  $\phi_1$  with a magnitude of the up or down swing decreasing with time. Similarly,  $\phi_2$  also exhibits an oscillatory behaviour. If one includes the results for



Fig. 6.18

The change in barrier thickness,  $s$ , with respect to total annealing time,  $t$ , is shown. Again the magnitude of the voltage is 1 volt and  $t_p$  is 2 hours. Squares represent the control junction.

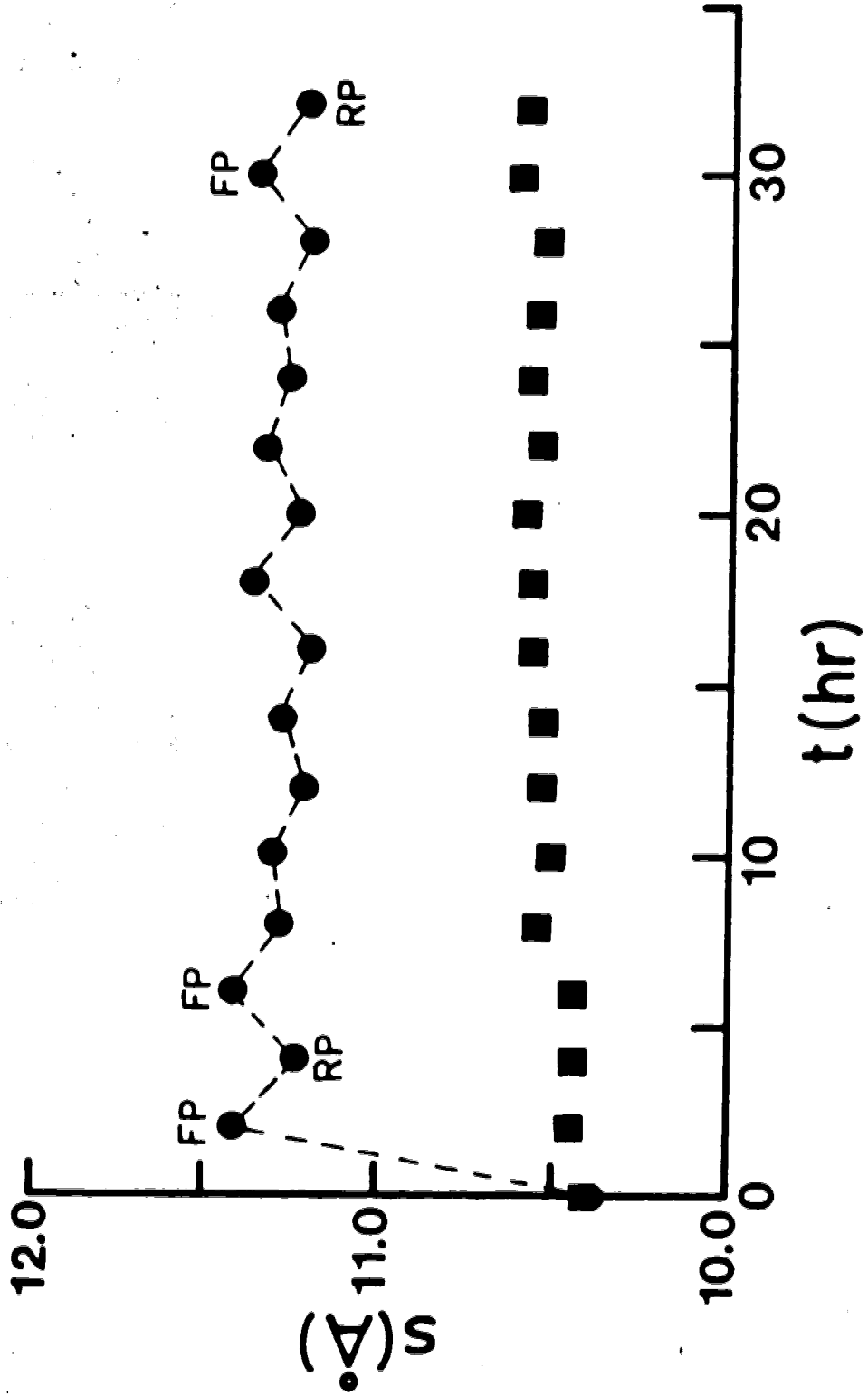
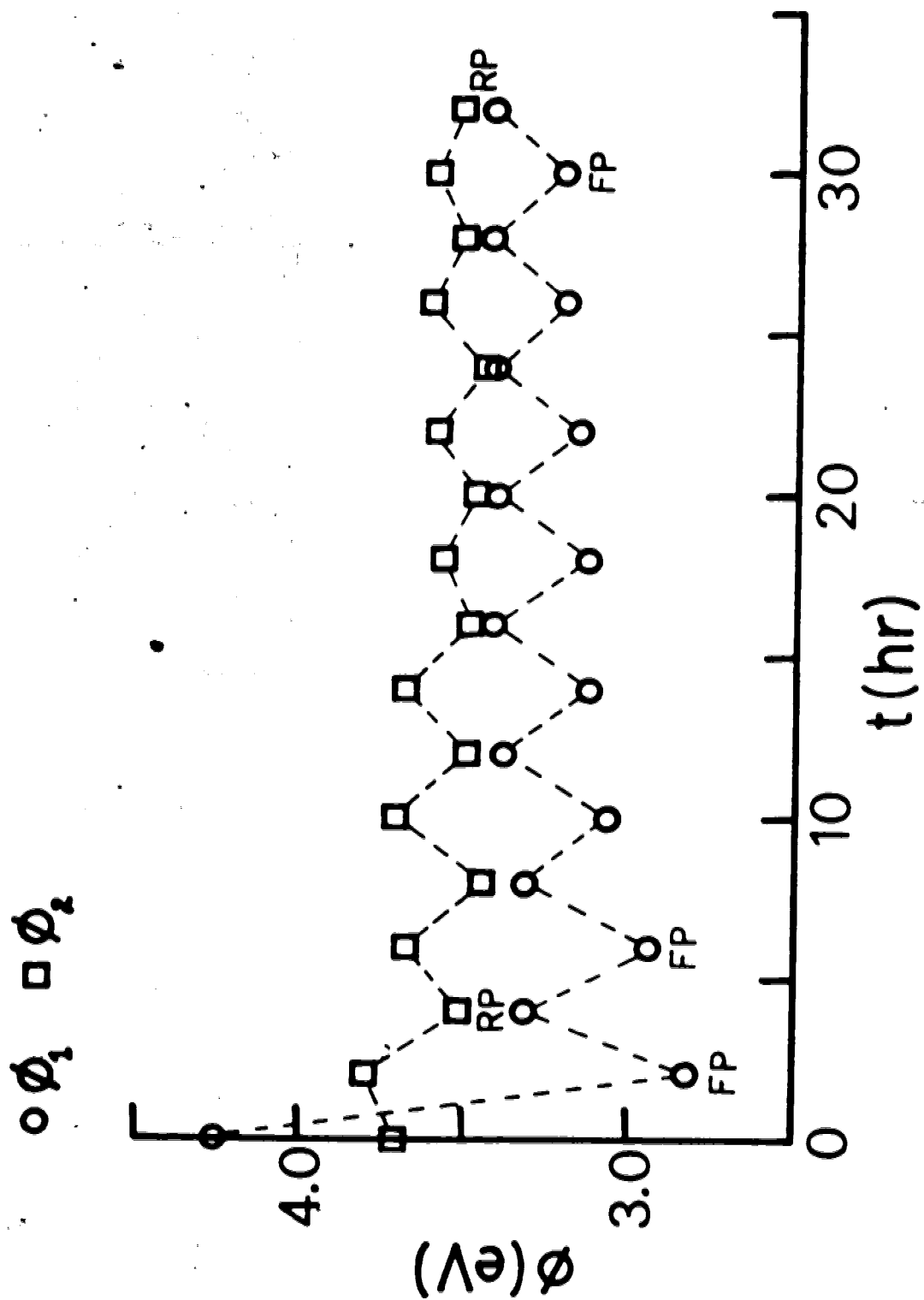


Fig. 6.19

The behaviour of  $\phi_1$  and  $\phi_2$  (barrier heights at the Al and Pb electrodes) versus time for alternating polarity voltage annealing is shown.



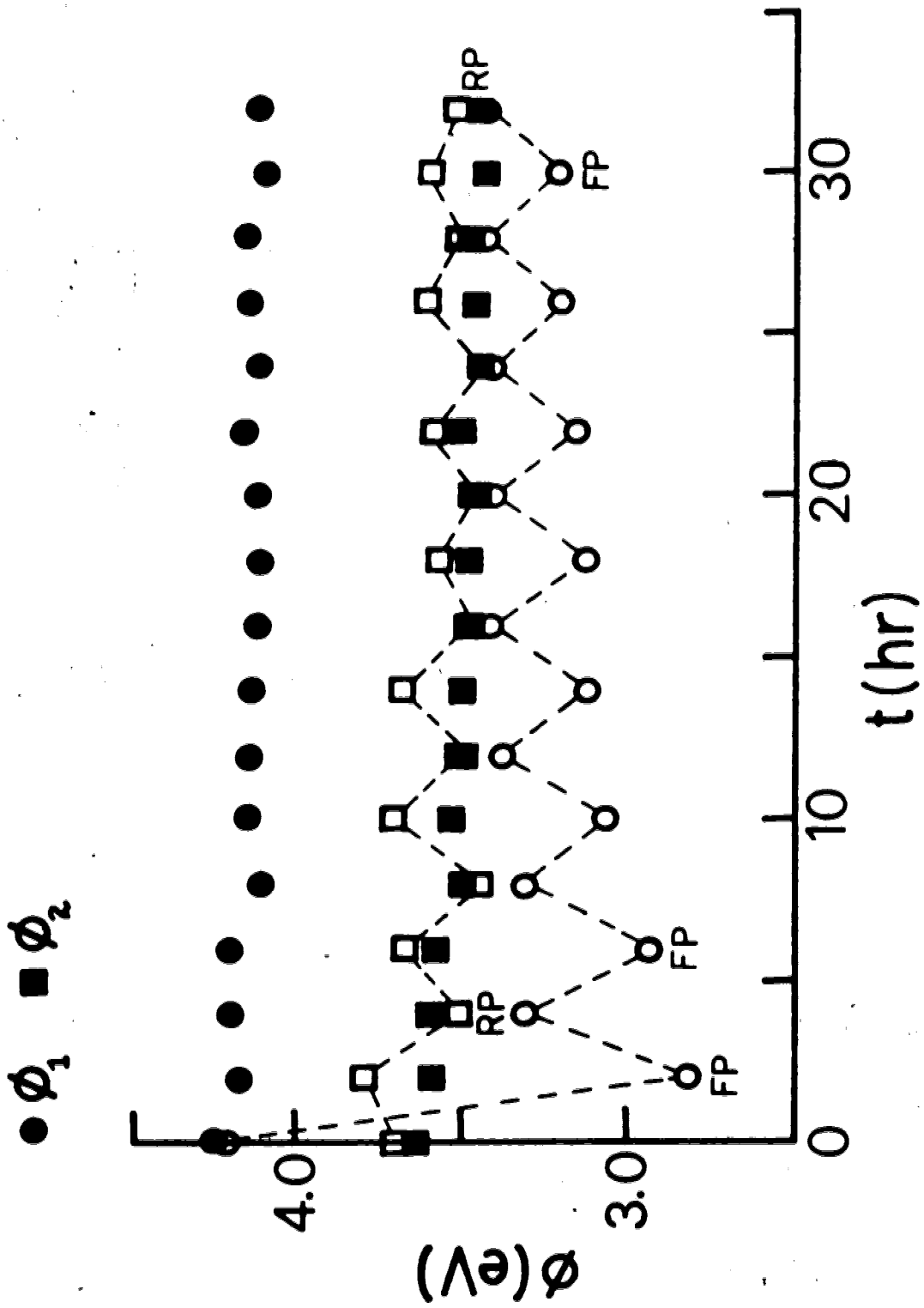
the control junction (Fig. 6.20), it is seen that the control values of  $\phi_2$  - the barrier height at the lead electrode - lie within the region determined by the oscillating  $\phi_2$  values of the other junction. We see though that the same is not true for  $\phi_1$ ; the alternating polarity has resulted in a large downward shift in  $\phi_1$ . This implies that the interesting things are happening at the Al electrode.

Summarizing this data, we see that there is a large change, occurring at the Al-Al oxide interface, in the first 2 hours when the junction is subjected to an FP anneal which cannot be completely reversed by an RP anneal. Moreover, subsequent changes due to FP annealing are small compared to those in the first 2 hours. This suggests that initially, the influence of the FP voltage quickly forces a portion of the positive charge, presumably Al ions, into a number of available trapping sites from which the ions cannot be easily removed when a reverse polarity bias is applied. By trapping is meant any mechanism within the barrier which makes it difficult to later remove the charge from the barrier. Such trapping could occur by the filling of vacancies, or by bonding of Al ions to negative ions within the insulator, possibly oxide ions.

The results following the first two hours show that a smaller portion of charge seems to be fairly mobile under the influence of changing polarities, however the

Fig. 6.20

The behaviour of  $\phi_1$  and  $\phi_2$  for the thermally annealed control junction is included in this picture as denoted by the shaded in circles and squares.



amount of this mobile charge seems to be decreasing with time as indicated by the decreasing amplitude of up and down swing on the resistance and  $\phi_1$  graphs. This, along with the general increase in resistance suggests that charge trapping is still occurring but at a much slower rate than in the initial 2 hours.

To obtain more insight into this work, further study should examine the influence of such variables as

- 1) length of annealing period,  $t_p$ ,
- 2) magnitude of the annealing voltage, and
- 3) the effect of initially annealing the junction with a reverse polarity instead of forward polarity.

One should note that in the above experiment the intrinsic field of the junction is not considered. This field has been shown to be of forward polarity with a magnitude of about 0.5 volts. Thus, applying a bias of 1V FP yields a net field of 1.5 V FP while a bias of 1V RP gives a net field of 0.5 V RP. Therefore, if one wishes to have equal and opposite net fields across the junction of 1 volt magnitude, one must use asymmetric applied biases of 0.5 V FP and 1.5 V RP respectively. Work has begun on this but the results are not yet complete.

#### 6.5. Origin of the Intrinsic Electric Field

At this stage, the origin of the junction's intrinsic electric field is considered. The intrinsic field of the Al-Al oxide-Pb tunnel junction probably does not arise



solely from a difference in the work functions of aluminum and lead ( $Al \approx 4.28$  eV,  $Pb \approx 4.25$  eV) since this difference is quite small (97) compared to the estimated 0.5 V potential difference. Also, a field seems to exist in Al-Al oxide-Al junctions for which the two electrodes are the same, thus it would seem that something within the oxide insulator is primarily responsible for the intrinsic electric field. This "something" could be the presence of a relatively immobile (due to the ion size) negative oxide ion layer created in the process of oxidizing the aluminum. It would be near the surface of the oxide (i.e. closer to the Pb electrode than the Al one in an Al-Al oxide-Pb junction) and thus create an electric field of forward polarity (Pb-ve) as observed. The presence of such oxide ions has been described by Mott (102) in his theory of the formation of protective oxide films on metals.

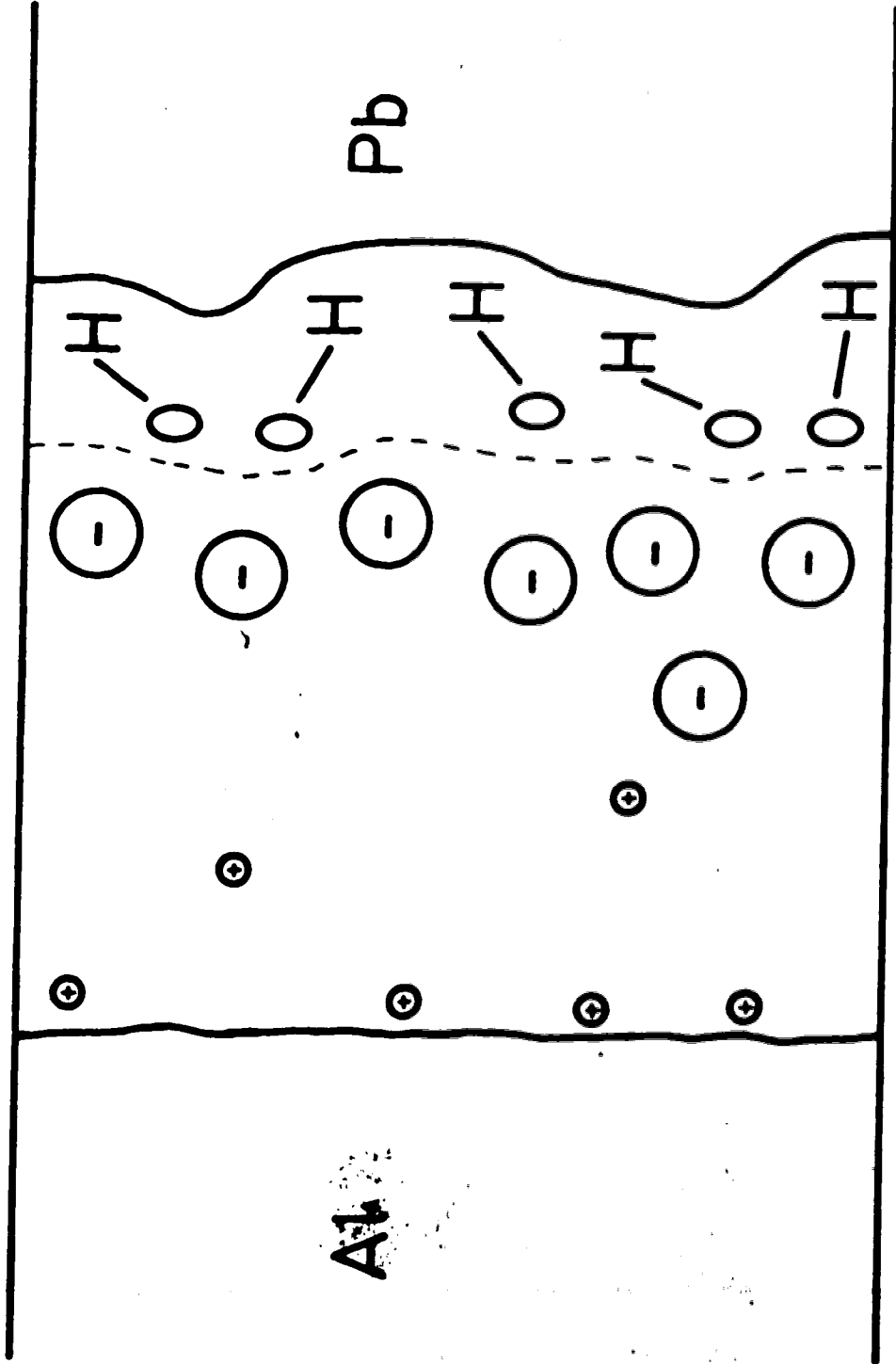
Such a negative oxide ion layer (Fig. 6.21) could have several effects:

- 1) it would provide a force for the movement of positive Al ions in the barrier;
- 2) any bonding of Al ions with oxide ions would neutralize negative oxide ion charge as well as that of positive Al ions;
- 3) with the above occurring, the process would slow down as the negative oxide ion layer is depleted (i.e. the intrinsic electric field diminishes);
- 4) the negative oxide layer's influence on the surface

Fig. 6.21

A model for the aluminum oxide barrier with the inclusion of a negative oxide ion layer is shown.

⊕ Al ion  
⊖ O ion



Al

hydroxyls may serve to attract the positive hydrogen end of the hydroxyl group thus either canting it and/or hydrogen bonding with it somewhat and thus hindering its freedom of motion;

5) any neutralization of the negative oxide layer by diffused Al ions will reduce the negative charge influence on the hydroxyl groups, thus allowing for reorientational motion away from the oxide layer toward the lead electrode.

If an external field of forward polarity (Al positive, Pb negative) is applied:

1) the creation and migration of Al ions into the barrier is enhanced;

2) the influence of the negative oxide layer on the surface hydroxyl groups is lessened due to a negative force attracting the hydrogen from the lead electrode side.

On the other hand, if a field of opposite polarity is applied:

1) a reverse polarity field would compete with the negative oxide ion layer for positive Al ions. Since a relative equilibrium existed prior to RP field application, the RP field would draw some already existing Al ions out of the barrier;

2) the positive force at the lead electrode would hinder reorientation of surface hydroxyl groups.

#### 6.6. Annealing of Al-Al Oxide-Metal Junctions

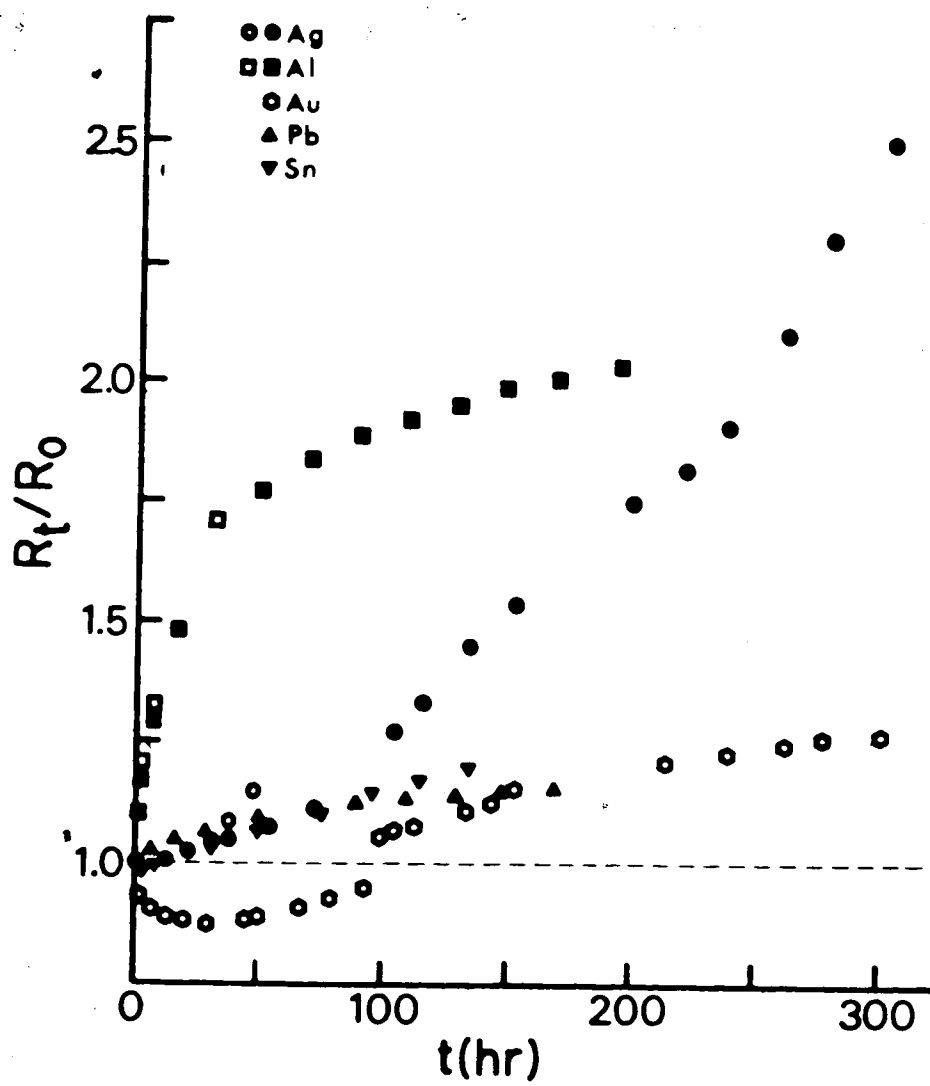
Attention is now turned to the influence of the top

metal electrode on the annealing process. In this experiment one junction of a pair of Al-Al oxide-metal junctions has a lead cover layer and serves as a control, while the other junction has a top electrode of a different metal, such as Ag, Al, Au, Cu, In, Mg or Sn. These junctions are thermally annealed. As will be seen, barrier parameters and annealing behaviour are often quite different from those observed when a lead top electrode is used.

Fig. 6.22 shows a plot of the resistance ratio  $R_t/R_0$  versus the total annealing time  $t$  for junctions with various cover electrodes where  $R_t$  is the resistance at time  $t$ . The resistance behaviour of Pb, In, Sn, and Mg appear to be fairly similar. Cu may be included also in this group although its resistance fluctuated up and down with no set pattern - it also tended to develop filaments, with a consequent resistance drop, which were "burnt out" when the sweep bias was applied to the junction at helium temperature resulting in the resistance increasing to the "expected" value. The Al and Ag behaviour is much more dramatic than that of Pb while Au is in between. The discontinuity at ~ 95 hours in the gold junction may be due to the "burning out" of a filament. Although the Al resistance ratio increase is much larger than that of Pb, the curvature of the graph is the same (i.e. an increase which tends to eventually saturate). The silver electrode junction's curvature is radically different - it is reversed and shows no sign of resistance saturation even after 300

Fig. 6.22

Plots of  $R_t/R_0$  vs  $t$  for several Al-Al oxide-metal junctions, where  $R_t$  is the resistance at time  $t$ , are shown. Data for Mg and Cu are not plotted (for the sake of clarity in the figure) but lie in the region bounded by the Pb and Sn curves.



hours of annealing.

Since these are preliminary results with data for only one or two specimens of each cover electrode available, interpretation of results is difficult at this stage, however, several observations can be made.

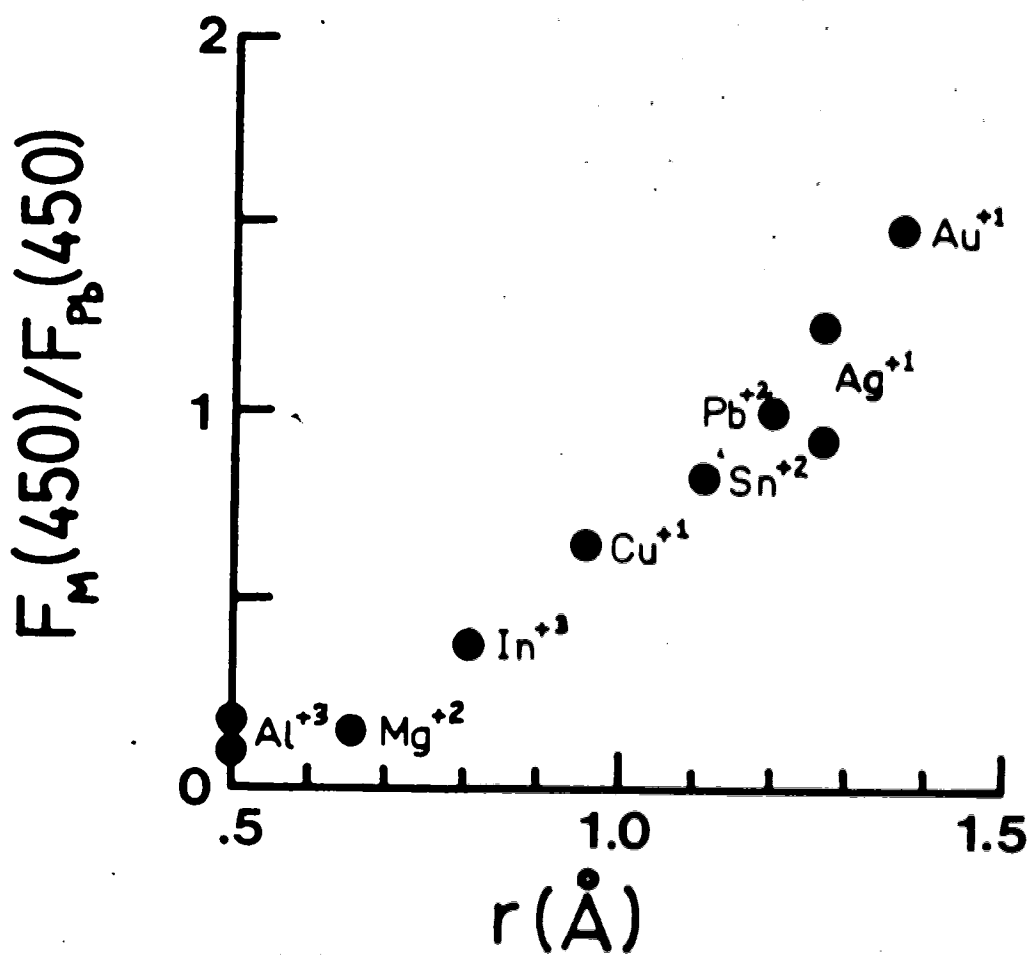
During the preparation of these samples, the top electrodes were all initially evaporated very slowly so as to gently cover the insulating barrier. In view of the past work (51, 92) on ionic radii of metals and depth penetration into the barrier, a plot of normalized (to the lead control) 450 meV peak intensity versus ionic radius for metals in selected oxidation states is shown in Fig. 6.23. The 450 meV peak is chosen because it is due to O-H stretching of hydroxyl groups on the surface of the aluminum oxide. Since these hydroxyl groups are proximate to the cover electrode, penetration of the cover electrode metal into this hydroxyl layer is expected to shunt out some of these groups and hence reduce the intensity observed in the IET spectrum.

Previous work (92) on the use of ethylene ( $C_2H_4$ ) plasma discharge barriers used the 360 meV peak due to C-H stretching, while an even earlier study (51) on oxide barriers again used the 360 meV peak, this time arising from hydrocarbon contamination on the oxide surface. These works showed a correlation between the normalized 360 meV peak intensity and ionic radius although the chosen



Fig. 6.23

A graph of normalized 450 meV peak intensity  $F_M(450)/F_{Pb}(450)$  versus  $r$ , the ionic radius of the metal, is shown. Here  $F_M(450)$  is the 450 meV peak intensity for a junction with cover metal M.



oxidation states of the metals were not the same. This cursory study using the 450 meV peak also shows a relationship between the peak intensity and ionic radius. The ionic radii used in this and previous works are shown in Table 6.1.

Another way of looking at the penetration is by comparing the resistance of a junction with a cover layer other than lead to the lead control. If there is more or less penetration, the resistance should be lower or higher as the case may be. This ratio is plotted in Fig. 6.24 using the same ionic radii as listed above for Fig. 6.23. There is a good correlation for the five metals Mg, In, Cu, Pb, and Au. Al and Sn are above the line while Ag is below.

Consider first the case of aluminum. Its IET spectrum shows a hint of the 450 meV peak (Fig. 6.25), although, having a smaller ionic radius than Mg (which in Fig. 6.26 shows no 450 meV peak at all) it is expected to show none. Aluminum thus does not appear to penetrate as far as expected which may be due to the following reason. Some of the aluminum that does penetrate may interact with the hydroxyl groups or even the aluminum oxide layer itself. Since aluminum is fairly reactive (which is why it is easy to make tunnel junctions with it as a base layer), this possibility seems likely when considering the large resistance increases exhibited by Al-Al oxide-Al junctions as well as a possible availability

Table 6.1  
Ionic radii of metals (Å)

<u>This work</u>	<u>Magno et al. (92)</u>	<u>Geiger et al. (51)</u>
Au <sup>+1</sup> 1.37	Au <sup>+3</sup> 0.85	Au <sup>+1</sup> 1.37
Ag <sup>+1</sup> 1.26	Ag <sup>+1</sup> 1.26	Ag <sup>+1</sup> 1.26
Pb <sup>+2</sup> 1.20	Pb <sup>+2</sup> 1.20	Pb <sup>+4</sup> 0.84
Sn <sup>+2</sup> 1.12	Sn <sup>+2</sup> 1.12	Sn <sup>+4</sup> 0.71
Cu <sup>+1</sup> 0.96		
In <sup>+3</sup> 0.81	In <sup>+3</sup> 0.81	In <sup>+3</sup> 0.81
	Zn <sup>+2</sup> 0.74	
Mg <sup>+2</sup> 0.66		Mg <sup>+2</sup> 0.66
Al <sup>+3</sup> 0.50		Al <sup>+3</sup> 0.50

Fig. 6.24

This figure shows a relationship between  $R_{M M} A_M / R_{Pb Pb} A_{Pb}$  and  $r$ , the ionic radius of the metal.  $R_M$  is the initial resistance of a junction with top electrode metal M and  $A_M$  its area.

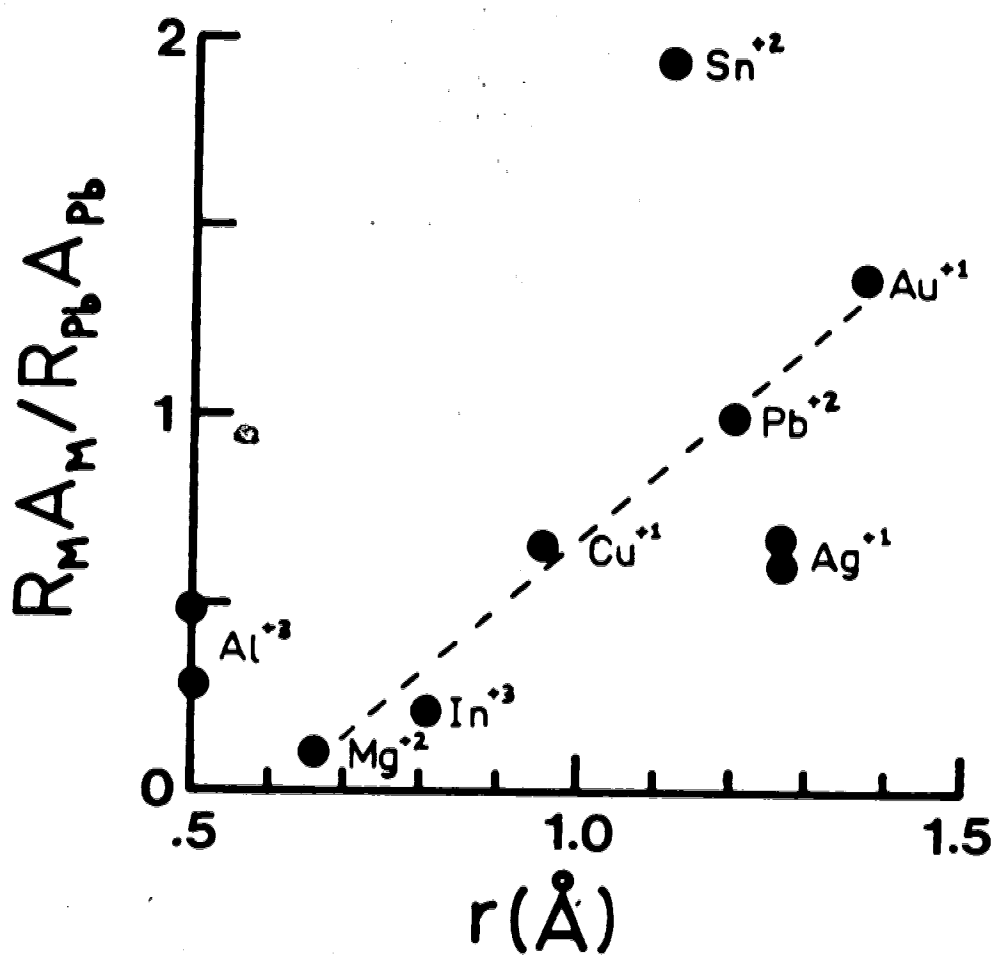


Fig. 6.25

The IET spectrum of an Al-Al oxide-Al junction is shown.

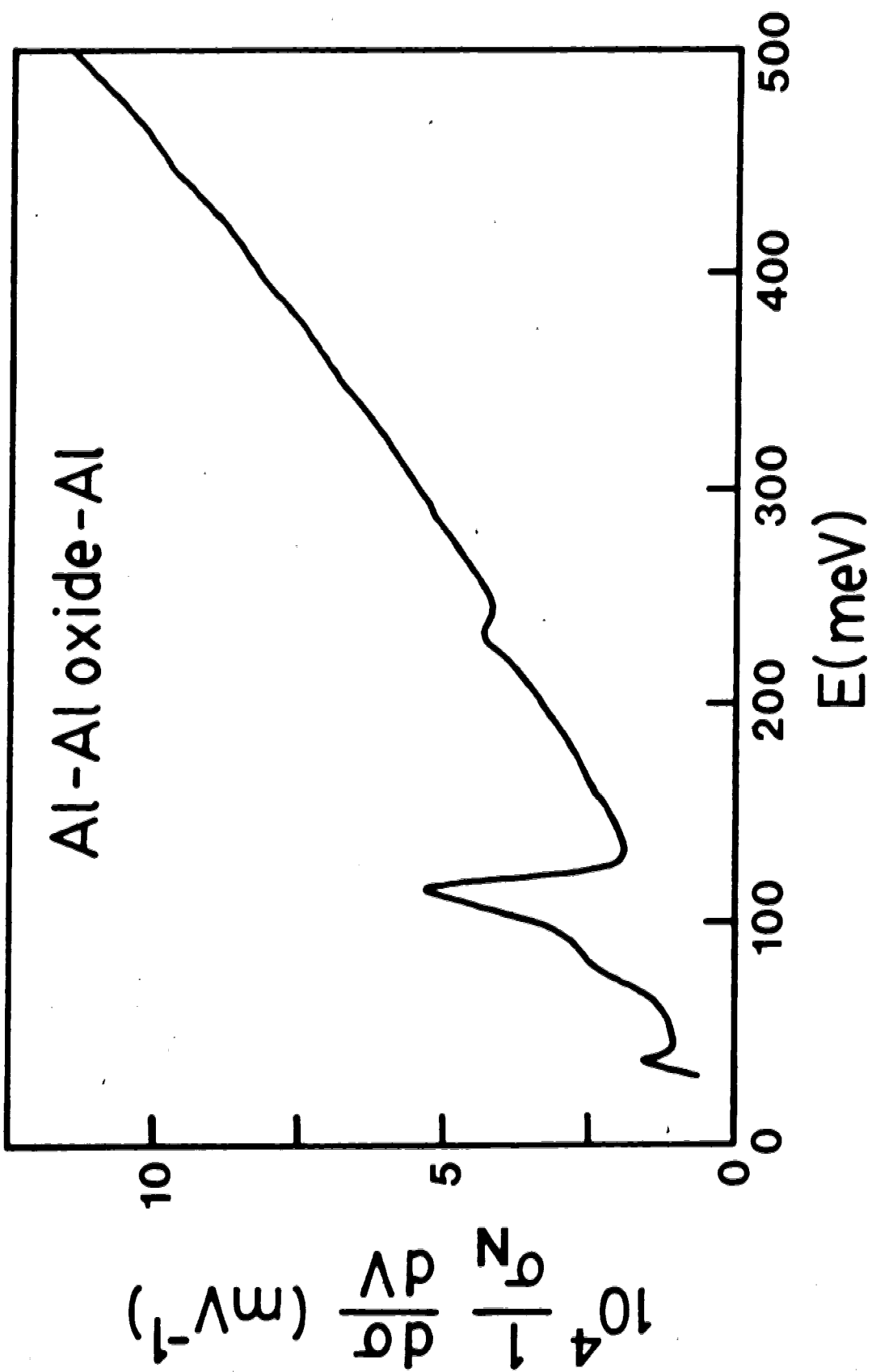
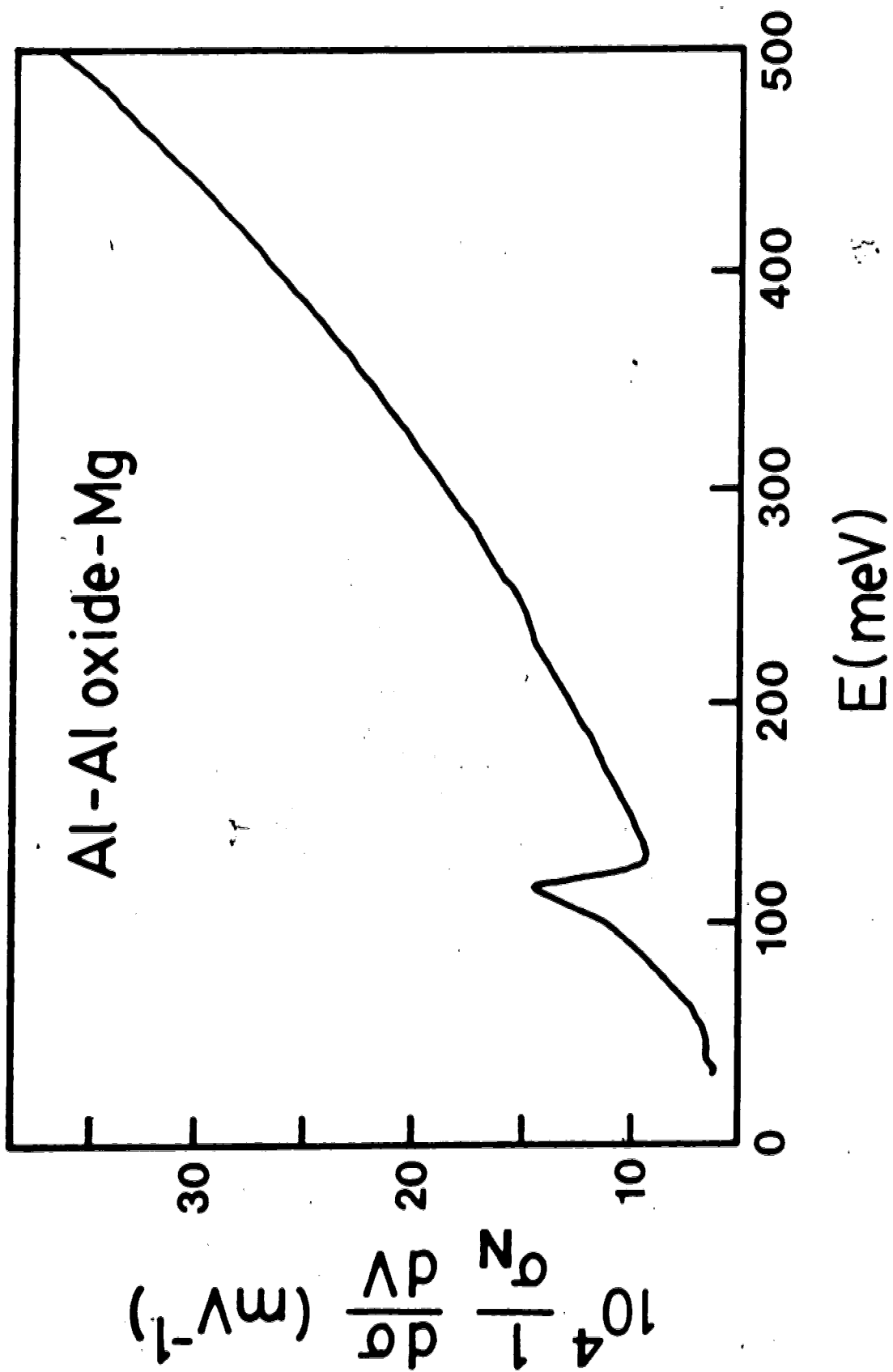




Fig. 6.26

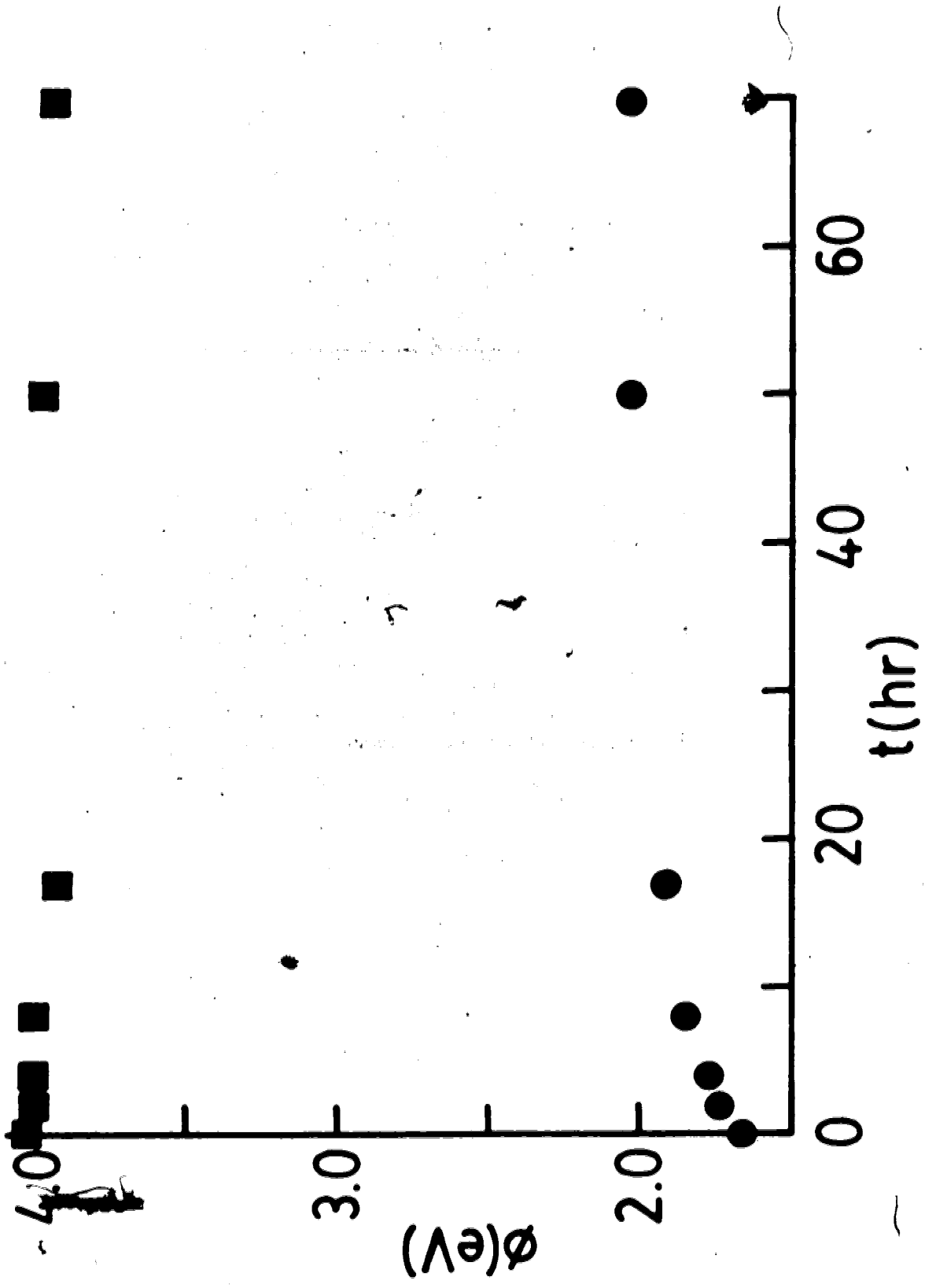
The IET spectrum of an Al-Al oxide-Mg junction is shown.  
Note the complete absence of the 450 meV peak.



of negative oxide ions thought to be responsible for the junction's intrinsic electric field. During the evaporation of the aluminum cover electrode, the small ionic radius aluminum may penetrate so far as to come in contact with some of the oxide ion layer. A reaction with a portion of this layer would create more aluminum oxide insulator and thus increase the junction resistance to a value larger than expected if the aluminum remained as "inert" metal ions or particles. The apparent penetration is thus not as great as expected. Also, it is likely that aluminum ions from the top electrode (once the junction is completed) are closer to and therefore more strongly attracted to the negative oxide ion layer (responsible for the junction's intrinsic electric field) than those from the base electrode. Hence, resistance increases during annealing due to Al ions reacting with and neutralizing the oxide ion layer, normally due to base electrode Al ions in Al-Al oxide-Pb junctions may well, in this case, be due to top electrode Al ions. As this happens, the oxide ion electric field is decreased and Al ions originally present at the base electrode will experience a less negative (i.e. more positive) potential forcing some of them out of the barrier. This will cause  $\phi_1$  to increase which is what happens (Fig. 6.27). The resistance decrease due to the loss of these ions from the barrier at the base electrode is small (for example, the application of a 0.5 V RP field to an Al-Al oxide-Pb junction yields a resistance ratio

Fig. 6.27

The behaviour of  $\phi_1$  and  $\phi_2$  versus  $t$  for an Al-Al' oxide-Al junction is shown.  $\phi_1$  is represented by circles and  $\phi_2$  by squares.



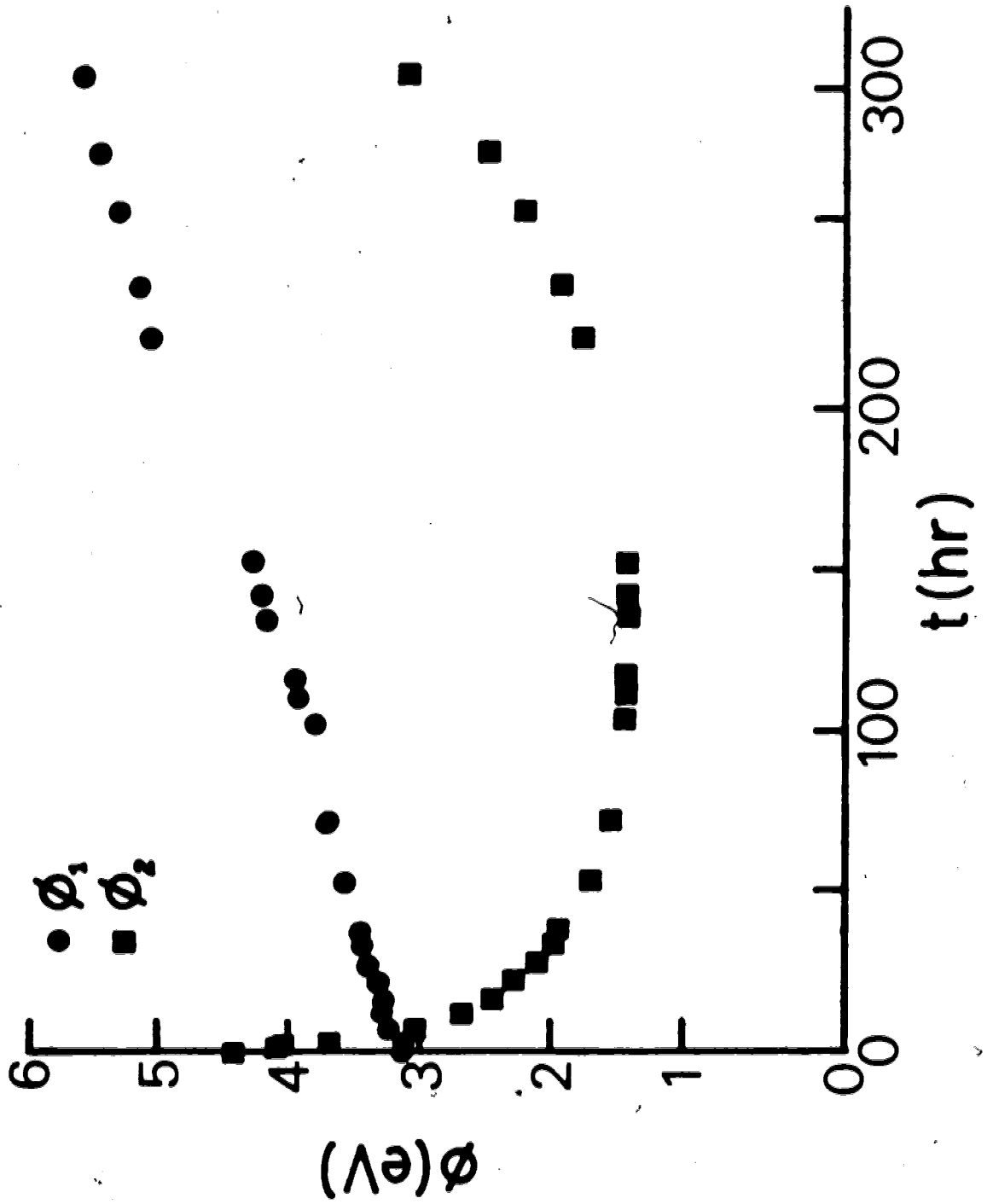
minimum  $\sim 0.95$  with a change in  $\phi_1$  comparable to that in the Al-Al oxide-Al junction) compared to the overall increase due to the reaction occurring at the top electrode, therefore the net resistance change is one that increases.

In the case of the tin cover layer, only one sample is available at present so no suggestion as to its behaviour will be put forward.

Unlike aluminum or tin, junctions with a silver top electrode are below the line (Fig. 6.24), that is to say, the silver penetrates further than expected. Its resistance behaviour (Fig. 6.22), as well as changes in  $\phi_1$  and  $\phi_2$  (Fig. 6.28) are quite different from the other junctions. The rapid initial decrease in  $\phi_2$  implies that the silver side of the junction is becoming more positive. This, coupled with the eventual resistance increase suggests that positive Ag ions are being created at the silver electrode and migrate into the aluminum oxide (perhaps under the influence of the intrinsic electric field). This influx of positive ions could cause the Al electrode side to experience a positive potential thus forcing Al ions out of the barrier and causing  $\phi_1$  to rise. One notes however, that  $\phi_1$  does not saturate but keeps on climbing; also, the resistance continues to rise. It is seen that  $\phi_2$  reaches a minimum which is maintained for 100-150 hours and then increases again. This suggests that some of the Ag ions have moved into the oxide and eventually move far enough into the oxide so as to decrease positive ion

Fig. 6.28

This graph shows how  $\phi_1$  and  $\phi_2$  (barrier heights at the Al and Ag electrodes) change with time for an Al-Al oxide-Ag junction. The Ag electrode is seen to become rapidly positive in the initial stages of thermal annealing.





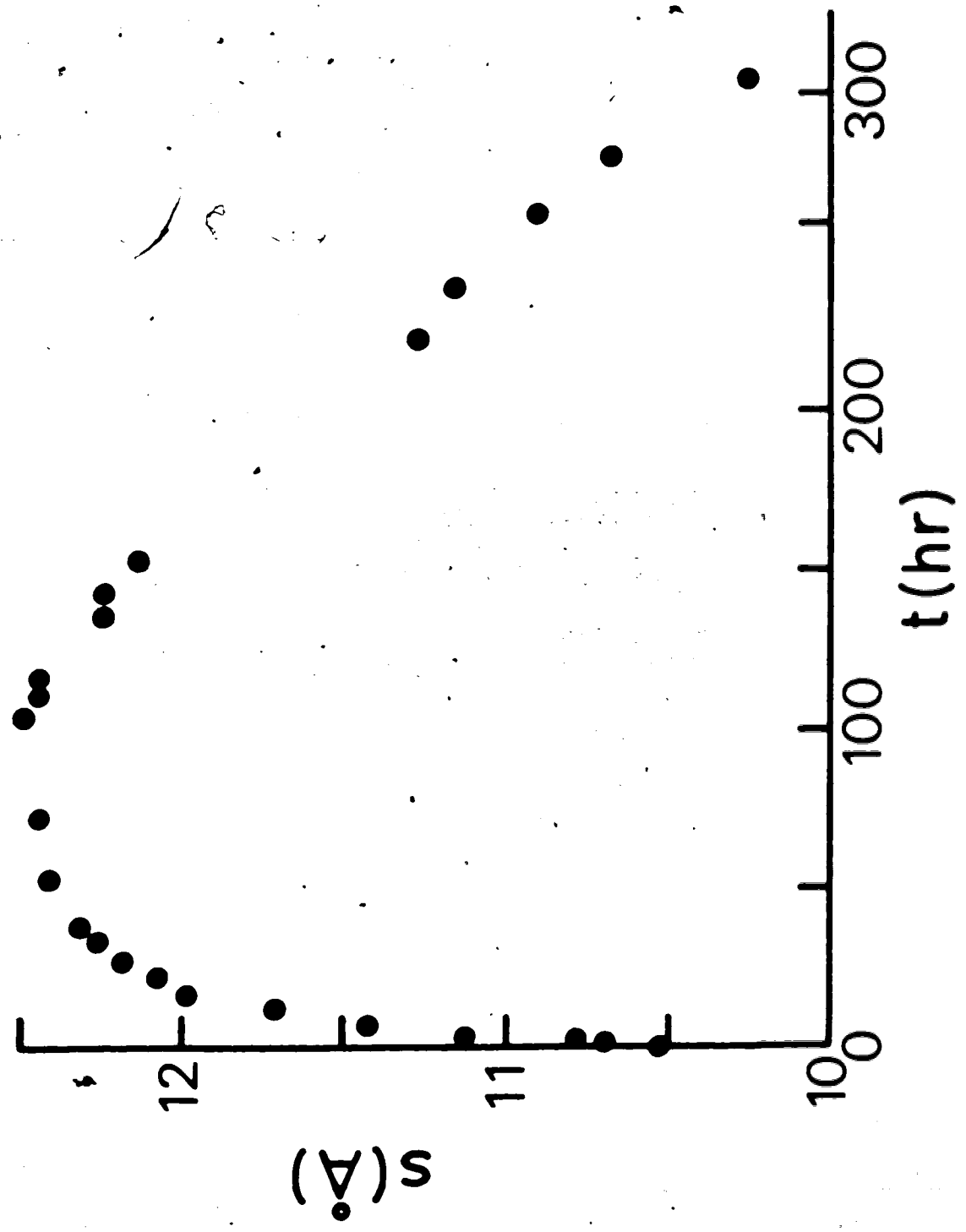
influence on the oxide-Ag interface (thus causing it to become less positive). Meanwhile, as the silver ions move toward the Al electrode, Al ions are continually being forced out thereby causing the increase in  $\phi_1$ .

The question one asks is why does this happen to silver and not to the other metals? Perhaps the answer lies in the work on  $\beta$ -alumina (81). Beta-alumina is an aluminum oxide doped with a small amount of NaO (empirical formula  $\text{Na}_2\text{O} \cdot 11\text{Al}_2\text{O}_3$ ) (12, 18) and so named because it was thought to be an isomorph of  $\text{Al}_2\text{O}_3$  since the presence of sodium was either unknown or considered unimportant by early workers. The Na ions in this material, of interest in the field of fast ionic transport in solids, are highly mobile. It is also relatively easy to substitute Ag ions for the Na ions in this material. Other ions used for substitution (which substitute less easily than Ag) tend to be monovalent cations (in particular, the alkali metals) unlike most of the metals used for the junction cover electrodes. In addition, work on  $\beta$ -alumina shows that substitution of Ag for Na causes the lattice to contract; all other cationic substitutions result in a lattice expansion. With these points in mind it is interesting to speculate that while the aluminum oxide of the barrier is not likely to contain sodium and is thus not  $\beta$ -alumina (but rather an amorphous alumina (125)), it may possess properties necessary to induce Ag ions to enter into the oxide. A tendency of Ag to enter into the insulator could

account for its initial lowered resistance compared to Pb (Fig. 6.22). During the first 100 hours of annealing a buildup of positive Ag ions may occur within the aluminum oxide near the oxide-Ag interface causing a decrease in  $\phi_2$  along with increases in resistance and barrier thickness  $s$  (Fig. 6.29). In the next 100 hours, Ag ions may predominantly drift into the aluminum oxide, causing the greater resistance increase, and enter into appropriate sites to effect a lattice contraction and hence a decrease in  $s$ . During this stage,  $\phi_2$  is fairly constant indicating that any positive charge that drifts into the oxide is replaced by new ions. Following these first 200 hours,  $\phi_2$  starts to increase again, suggesting the number of Ag ions near the top electrode is decreasing as the ions enter into the oxide, meanwhile still increasing the resistance and decreasing  $s$ . Although one can thus interpret these annealing results, questions remain and further work needs to be done on Al-Al oxide-Ag junctions before making any definite conclusions.

Fig. 6.29

The change in barrier thickness with time,  $s$  vs  $t$ , for Al-Al oxide-Ag is shown. At first,  $s$  increases to a maximum and then decreases quite rapidly.



## CHAPTER 7

### SUMMARY AND CONCLUSIONS

#### 7.1. Conclusions

In the course of studying annealing effects in tunnel junctions, many interesting observations were made.

Al-Al oxide-Pb tunnel junctions subjected to thermal annealing at room temperature show overall increases in resistance and in IET peak intensities (118 and 450 meV peaks) with respect to time. A reorientation of surface hydroxyl groups under the influence of an intrinsic electric field of forward polarity has been suggested.

Voltage annealing of Al-Al oxide-Pb tunnel junctions tended to enhance or inhibit the changes observed in the thermal annealing case, depending upon the polarity of the applied voltage. Enhancement was observed with a forward polarity bias. In fact, the application of a forward polarity voltage (0.5 V FP) causes an accumulation of positive charge, presumably Al ions, at the Al-Al oxide interface. On the other hand a reverse polarity bias (0.5 V RP) causes the removal of some positive charge from the Al-Al oxide interface region. In addition, peak intensities do not change because the magnitude of the bias seems sufficient to negate the junction's intrinsic field, thereby leaving no electric field to reorient

molecular groups. Junction aging is thus postponed until the reverse polarity voltage is removed, at which time normal thermal annealing occurs.

Voltage annealing with alternating polarity showed that a large portion of the positive charge that could be moved into the aluminum oxide under the influence of a forward polarity bias remained trapped within the barrier, while a smaller portion was fairly mobile and could be moved in or out depending upon the polarity of the applied bias. The largest changes occurred within the first two hours of annealing.

The origin of the junction's intrinsic electric field, estimated to be 0.5 V FP, has been suggested as being due to a layer of negative oxide ions near the aluminum oxide surface, just below the surface hydroxyl groups. These oxide ions are assumed to be formed as part of the process of aluminum oxide growth in a plasma discharge.

Preliminary thermal annealing studies of Al-Al<sub>2</sub>O<sub>3</sub> oxide-metal tunnel junctions resulted in some behaviour similar to Pb for Cu, In, Mg, and Sn, while Ag, Al, and Au were different. Speculative models were presented for the aluminum and silver behaviour, but further work needs to be done on these, and the other metal cover electrodes. Finally, a relation between the surface hydroxyl stretch peak intensity (450 meV) and ionic radius of the top electrode metal showed that more penetration into the oxide

occurred the smaller the ionic radius became.

## 7.2 Afterthoughts

At the outset, the Al-Al oxide-Pb system was chosen as the system to study since it is the most common type of junction used in IETS, the oxide being frequently doped with organic molecules. The oxide barrier, being less complex than an oxide plus organic molecule barrier, was thought to be a "simple" material to study. However, through the course of experiments described in this thesis, as well as research into the literature concerning areas such as catalysis, chemistry, mineralogy, IR and Raman spectroscopy, etc., the "simple" barrier was found to be somewhat more complicated.

Aluminum oxide, hydrated and unhydrated, exists in a multitude of forms, both man-made and natural (34, 35, 49, 124, 125). Only one form of unhydrated aluminum oxide exists in nature. This is the most stable form,  $\alpha$ -alumina ( $\alpha$ -Al<sub>2</sub>O<sub>3</sub>) which is also called corundum and is one of the hardest known minerals. Hydrated forms of alumina (124) found in nature include boehmite and diaspore (AlO(OH)), and gibbsite and bayerite (Al(OH)<sub>3</sub>). Heating and dehydrating these minerals under various conditions yields a variety of other aluminas including  $\gamma$ ,  $\delta$ ,  $\eta$ ,  $\theta$ ,  $\chi$ ,  $\kappa$ , and finally, with enough heat  $\alpha$ -alumina is arrived at (35).  $\gamma$ -alumina is of interest as a catalytic substrate (88, 89) and has been well studied (103, 104).

The alumina formed by the electrolytic anodization of aluminum metal has been found to be amorphous alumina (125) which can undergo a transformation to  $\gamma$ -alumina upon heating above  $\sim 400^\circ\text{C}$ . The aluminum oxide formed in the plasma discharge is most likely amorphous alumina (125) covered with some surface hydroxyl groups.

Infrared spectroscopy has been used to study the various forms of alumina (38, 45, 88-90, 103-105, 120-123, 125). Bands occur in the 30-120 meV region of the various spectra for different types of alumina. Other work has also shown that the absorption region for metal-oxygen stretching (in our case Al-O stretching) depends upon the coordination of the metal with respect to the oxygen (11, 45, 121). For tetrahedral coordination ( $\text{AlO}_4$ ) the region is 85-110 meV ( $700-900\text{ cm}^{-1}$ ) whereas octahedral coordination ( $\text{AlO}_6$ ) has the range 60-80 meV ( $500-650\text{ cm}^{-1}$ ).

An X-ray diffraction study on amorphous alumina (a-alumina) by A.M. Jones (Ph. D. thesis, 1974, Texas Christian University) suggests that most of the aluminum is in tetrahedral coordination. Also, as mentioned in Chapter 5.2, work on anodized alumina (an amorphous material) gives infrared bands at 960 and  $650\text{ cm}^{-1}$  (117 and 79 meV) due to alumina modes.

The identification of the 118 meV peak as being due to Al-O stretching is thus reaffirmed, however, one now again must consider the 85 meV shoulder as being composed of modes other than OH bending, such as modes



due to tetrahedrally coordinated and some octahedrally coordinated alumina. The resolution of this will certainly require more study and perhaps an examination of the infrared spectroscopic behaviour of other metals in tetrahedral coordination (21, 29, 99, 117, 121, 128).

### 7.3. Suggestions for Further Work

In the course of this work a better insight into the nature of the aluminum oxide barrier in tunnel junctions has been gained. However, as is usual, more questions have been raised than answered and so a few suggestions for further work will be presented.

As mentioned in Chapter 6.4 on alternating polarity voltage annealing further study should examine 1) the length of the annealing period  $t_p$ , 2) the magnitude of the annealing voltage, and 3) the effect of initially annealing the junction with a reverse polarity instead of forward polarity bias. Of interest would also be the application of "asymmetric" voltages, such that the net field (sum of the applied and intrinsic fields) would be the same in FP and RP annealing.

On the whole, more work needs to be done on junctions with different cover electrodes. Junctions with Al and Ag top electrodes are of particular interest in that their annealing behaviour is markedly different from Pb. As a note, the IET spectra of Ag junctions suggest the existence of an undershoot on the 450 meV peak

(surface OH stretching). This may be related to the predicted undershoot of Davis (33), and Birkner and Schattke (16).

It has been suggested here that the 85 meV shoulder is due to more than OH bending modes. Infrared work suggests the presence of other alumina modes in this region. A study of the annealing behaviour of Al-Al oxide-Mg and Al-Al oxide-Al junctions may provide the first step in separating OH bending modes from alumina modes, since the small ionic radii of these metals causes the surface OH groups to be shunted out.

Finally, one eventually hopes to study metal-insulator-metal junctions with insulators other than aluminum oxide in order to better understand the interaction of the different metal electrodes with the insulating barrier.

## BIBLIOGRAPHY

1. J.G. Adler and J.E. Jackson. System for observing small non-linearities in tunnel junctions. Rev. Sci. Instr. 37, 104 (1966).
2. J.G. Adler. Observation of longitudinal phonons in magnesium and aluminum by inelastic electron tunneling. Phys. Lett. 29A, 675 (1969).
3. J.G. Adler. Observation of the phonon spectra of MgO by inelastic electron tunneling in metal-insulator-metal junctions. Solid State Commun. 7, 1635 (1969).
4. J.G. Adler, T.T. Chen, and J. Straus. High resolution electron tunneling spectroscopy. Rev. Sci. Instr. 42, 362 (1971)
5. J.G. Adler and J. Straus. Application of minicomputers in high resolution electron tunneling. Rev. Sci. Instr. 46, 158 (1975).
6. J.G. Adler, M.K. Konkin, and R. Magnó. The technology of IETS in Inelastic Electron Tunneling Spectroscopy, Edited by T. Wolfram. (Springer-Verlag, Berlin, 1978) p. 146.
7. J.A. Appelbaum and W.F. Brinkman. Theory of many-body effects in tunneling. Phys. Rev. 186, 464 (1969).
8. S. Andersson and J.W. Davenport. Energy dependence of vibrational excitation of adsorbed CO and OH. Solid State Commun. 28, 677 (1978).
9. C.N. Banwell. Fundamentals of Molecular Spectroscopy (McGraw-Hill, New York, 1966).

10. J. Bardeen. Tunnelling from a many-particle point of view. *Phys. Rev. Lett.* 6, 57 (1961).
11. S.S. Batsanov and S.S. Derbeneva. Effect of valency and coordination of atoms on position and form of infrared absorption in inorganic compounds. *Zh. Strukt. Khim.* 10, 602 (1969). Engl. Trans. *J. Structural Chem.* 10, 510 (1969).
12. C.A. Beevers and M.A.S. Ross. The crystal structure of "Beta Alumina"  $\text{Na}_2\text{O}\cdot 11\text{Al}_2\text{O}_3$ . *Z. Krist.* 97, 59 (1937).
13. A.J. Bennett, C.B. Duke, and S.D. Silverstein. Theory of the tunneling spectroscopy of collective excitations. *Phys. Rev.* 176, 969 (1968).
14. D.W. Berreman. Infrared absorption at longitudinal optic frequency in cubic crystal films. *Phys. Rev.* 130, 2193 (1963).
15. A. Bianconi, R.Z. Bachrach, S.B.M. Hagstrom and S.A. Flodström. Al-Al<sub>2</sub>O<sub>3</sub> interface study using surface soft-X-ray absorption and photoemission spectroscopy. *Phys. Rev.* B19, 2837 (1979).
16. G.K. Birkner and W. Schattke. Inelastic tunneling assisted by molecular impurities. *Z. Physik* 256, 185 (1972).
17. W.M. Bowser and W.H. Weinberg. The nature of the oxide barrier in inelastic electron tunneling spectroscopy. *Surface Sci.* 64, 377 (1977).

18. W.L. Bragg, C. Gottfreid, and J. West. The structure of  $\beta$  alumina. *Z. Krist.* 77, 255 (1931).
19. A.B. Brailsford and L.C. Davis. Impurity-assisted inelastic tunneling: One-electron theory. *Phys. Rev. B* 2, 1708 (1970).
20. W.F. Brinkman, R.C. Dynes, and J.M. Rowell. Tunneling conductance of asymmetrical barriers. *J. Appl. Phys.* 41, 1915 (1970).
21. R.H. Busey and O.L. Keller, Jr. Structure of the aqueous pertechnetate ion by Raman and infrared spectroscopy. Raman and infrared spectra of crystalline  $\text{KTCO}_4$ ,  $\text{KReO}_4$ ,  $\text{Na}_2\text{MoO}_4$ ,  $\text{Na}_2\text{WO}_4$ ,  $\text{Na}_2\text{MoO}_4 \cdot 2\text{H}_2\text{O}$ , and  $\text{Na}_2\text{WO}_4 \cdot 2\text{H}_2\text{O}$ . *J. Chem. Phys.* 41, 215 (1964).
22. R.V. Coleman, R.C. Morris, and J.E. Christopher. Experiments on electron tunneling in solids, in Methods of Experimental Physics, Edited by R.V. Coleman. (Academic Press, New York, 1974) Vol. 11, p. 123.
23. C. Caroli, R. Combescot, P. Nozieres, and D. Saint-James. Direct calculation of the tunneling current. *J. Phys. C* 4, 1916 (1971).
24. C. Caroli, R. Combescot, D. Lederer, P. Nozieres, and D. Saint-James. A direct calculation of the tunneling current II Free electron description. *J. Phys. C* 4, 2598 (1971).

25. C. Caroli, R. Combescot, P. Nozieres, and D. Saint-James. A direct calculation of the tunneling current: IV. Electron-phonon interaction effects. J. Phys. C 5, 21 (1972).
26. C. Caroli, R. Combescot, D. Lederer-Rozenblatt, P. Nozieres, and D. Saint-James. Comment on a recent theory of tunneling without the transfer-Hamiltonian formalism. Phys. Rev. B 12, 3977 (1975).
27. S. Chapman. On the production of auroral and night-sky light. Phil. Mag. 23, 657 (1937).
28. T.T. Chen and J.G. Adler. Electron tunneling in clean Al-insulator-normal metal junction. Solid State Commun. 8, 1965 (1970).
29. H.H. Claassen and A.J. Zielen. Structure of the perrhenate ion. J. Chem. Phys. 22, 707 (1954).
30. R. Combescot. A direct calculation of the tunneling current III. Effect of localized impurity states in the barrier. J. Phys. C 4, 2611 (1971).
31. R. Combescot and G. Schreder. Tunneling in metal-semiconductor contacts: I. Influence of the impurities. J. Phys. C 6, 1363 (1973).
32. R. Combescot and G. Schreder. Tunneling in metal-semiconductor contacts: II. Influence of the electron-phonon interaction. J. Phys. C 7, 1318 (1974).
33. L.C. Davis. Impurity-assisted inelastic tunneling: Many-electron theory. Phys. Rev. B 2, 1714 (1970).

34. F.H. Day. The Chemical Elements in Nature (George G. Harrap & Co. Ltd., London, 1963).
35. M.K.B. Day and V.J. Hill. The thermal transformations of the aluminas and their hydrates. *J. Phys. Chem.* 57, 946 (1953).
36. G.A. Dorsey, Jr. The characterization of anodic aluminas I. Composition of films from acidic anodizing electrolytes. *J. Electrochem. Soc.* 113, 169 (1966).
37. G.A. Dorsey, Jr. The characterization of anodic aluminas III. Barrier layer composition and structure. *J. Electrochem. Soc.* 113, 284 (1966).
38. G.A. Dorsey, Jr. Far infrared absorption of hydrous and anhydrous aluminas. *Analyt. Chem.* 40, 971 (1968).
39. C.B. Duke. Tunneling in Solids (Academic Press, New York, 1969).
40. C.B. Duke, G.G. Kleiman, and T.E. Stakelon. Microscopic theory of tunneling: General theory and application to the static impurity. *Phys. Rev.* B 6, 2389 (1972).
41. J.R. Dyer. Applications of Absorption Spectroscopy of Organic Compounds (Prentice-Hall, Inc., Englewood Cliffs, N.J., 1965).
42. V.A. Dzis'ko, M. Kolovertnova, T.S. Vinnikova, and Yu. O. Bulgakova. The effect of poisoning on the selectivity of aluminum oxide in the decomposition

- of n-butyl alcohol. *Kinetika i Kataliz* 7, 655 (1966). *Engl. Trans. Kinetics and Catalysis* 7, 577 (1966).
43. H. Engstrom, J.B. Bates, J.C. Wang, and M.M. Abraham. Infrared spectra of hydrogen isotopes in  $\alpha$ - $\text{Al}_2\text{O}_3$ . *Phys. Rev. B* 21, 1520 (1980).
44. J.C. Evans. Raman spectroscopy in Infrared Spectroscopy and Molecular Structure, Edited by M. Davies. (Elsevier, Amsterdam, 1963) p. 199.
45. V.C. Farmer, Editor. The Infrared Spectra of Minerals (Mineralogical Society, London, 1974).
46. T.E. Feuchtwang. Theory of tunneling without transfer Hamiltonian: Relation between continuum and discrete formalisms, and equivalence with elementary theory for noninteracting systems. *Phys. Rev. B* 12, 3979 (1975).
47. J.C. Fisher and I. Giaever. Tunneling through thin insulating layers. *J. Appl. Phys.* 32, 172 (1961).
48. R.B. Floyd and D.G. Walmsley. Tunneling conductance of clean and doped Al-I-Pb junctions. *J. Phys. C* 11, 4601 (1978).
49. K. Frye. Modern Mineralogy. (Prentice-Hall Inc., Englewood Cliffs, N.J., 1974).
50. P.O. Gartland. Adsorption of oxygen on clean single crystal faces of aluminium. *Surface Sci.* 62, 183 (1977).



51. A.L. Geiger, B.S. Chandrasekhar, and J.G. Adler.  
Inelastic electron tunneling in Al-Al-oxide-metal systems. Phys. Rev. 188, 1130 (1969).
52. I. Giaever, H.R. Hart, Jr., and K. Megerle. Tunneling into superconductors at temperatures below 1°K. Phys. Rev. 126, 941 (1962).
53. K.H. Gundlach. Eine Methode zur Bestimmung der Austrittsarbeit Metall-Metalloxyd aus Tunnelstrommessungen an Sandwichschichten in Basic Problems in Thin Film Physics, Edited by R. Niedermayer and H. Mayer. (Vandenhoeck & Ruprecht, Göttingen, 1966) p. 696.
54. K.H. Gundlach. On the potential barrier shape in Al-Al<sub>2</sub>O<sub>3</sub>-Al tunnel junctions. Solid-State Electron. 12, 13 (1969).
55. K.H. Gundlach and J. Kadlec. Space-charge dependence of the barrier height on insulator thickness in Al-(Al-Oxide)-Al sandwiches. Appl. Phys. Lett. 20, 445 (1972).
56. R.M. Handy. Electrode effects on aluminum oxide tunnel junctions. Phys. Rev. 126, 1968 (1962).
57. P.K. Hansma. Inelastic electron tunneling. Phys. Rept. 30C, 145 (1977).
58. P.K. Hansma and J. Kirtley. Recent advances in inelastic electron tunneling spectroscopy. Acc. Chem. Res. 11, 440 (1978).

59. W.A. Harrison. Tunneling from an independent-particle point of view. *Phys. Rev.* 123, 85 (1961).
60. P. Hepple, Editor. Molecular Spectroscopy (The Institute of Petroleum, London, 1968) p. 43.
61. D.F. Hornig, H.F. White, and F.P. Reding. The infrared spectra of crystalline  $H_2O$ ,  $D_2O$  and HDO. *Spectrochim. Acta* 12, 338 (1958).
62. R.C. Jaklevic and J. Lambe. Molecular vibration spectra by electron tunneling. *Phys. Rev. Lett.* 17, 1139 (1966).
63. R.C. Jaklevic and J. Lambe. Molecular excitations in barriers II, in Tunneling Phenomena in Solids, Edited by E. Burstein and S. Lundquist. (Plenum Press, New York, 1969) p. 243.
64. R.C. Jaklevic and M.R. Gaerttner. Inelastic electron tunneling spectroscopy. Experiments on external doping of tunnel junctions by an infusion technique. *Applications of Surface Sci.* 1, 479 (1978).
65. J. Kadlec and K.H. Gundlach. Transient phenomena and their effect on the insulator barrier in Al-(Al-Oxide)-Al structures:  $T = 100^\circ K$ . *Thin Solid Films* 11, 423 (1972).
66. J. Kadlec and K.H. Gundlach. Transient phenomena and their effect on the insulator barrier in Al-(Al-Oxide)-Al structures:  $T = 300^\circ K$ . *Thin Solid Films* 20, 287 (1974).

67. R.G. Keil, T.P. Graham and K.P. Roenker. Inelastic electron tunneling spectroscopy: A review of an emerging analytical technique. *Appl. Spectrosc.* 30, 1 (1976).
68. J.J. Kipling and D.B. Peakall. Reversible and irreversible adsorption of vapours by solid oxides and hydrated oxides. *J. Chem. Soc.*, 834 (1957).
69. J. Kirtley and P.K. Hansma. Vibrational-mode shifts in inelastic electron tunneling spectroscopy: Effects due to superconductivity and surface interactions. *Phys. Rev. B* 13, 2910 (1976).
70. J. Kirtley, D.J. Scalapino and P.K. Hansma. Theory of vibrational mode intensities of inelastic electron tunneling spectroscopy. *Phys. Rev. B* 14, 3177 (1976).
71. J. Kirtley. Theoretical interpretation of IETS data in Inelastic Electron Tunneling Spectroscopy, Edited by T. Wolfram. (Springer-Verlag, Berlin, 1978) p. 80.
72. J. Kirtley and P. Soven. Multiple scattering theory of intensities in inelastic electron tunneling spectroscopy (IETS). *Phys. Rev. B* 19, 1812 (1979).
73. J. Kirtley and J.T. Hall. Theory of intensities in inelastic-electron tunneling spectroscopy orientation of adsorbed molecules. *Phys. Rev. B* 22, 848 (1980).

74. J. Klein, A. Léger, M. Belin, D. Défourneau, and M.J.L. Sangster. Inelastic-electron-tunneling spectroscopy of metal-insulator-metal junctions. Phys. Rev. B 6, 2336 (1973).
75. M.K. Konkin, R. Magno, and J.G. Adler. Asymmetry in inelastic electron tunneling peak intensities. Solid State Commun. 26, 645 (1978).
76. M.K. Konkin and J.G. Adler. Instabilities in thin tunnel junctions. Appl. Phys. Lett. 32, 436 (1978).
77. M.K. Konkin, R. Magno, and J.G. Adler. The use of barrier parameters for the characterization of electron tunneling conductance curves. Solid State Commun. 26, 949 (1978).
78. M.K. Konkin and J.G. Adler. A study of instabilities in superconducting tunnel junctions. Suppl. au Journal de Physique C-6, 591 (1978).
79. M.K. Konkin and J.G. Adler. Annealing effects in tunnel junctions (thermal annealing). J. Appl. Phys. 50, 8125 (1979).
80. M.K. Konkin and J.G. Adler. Annealing effects in tunnel junctions (voltage annealing). J. Appl. Phys. 51, 5450 (1980).
81. J.T. Kummer.  $\beta$ -alumina electrolytes. Prog. in Solid State Chem. 7, 141 (1972).
82. J. Lambe and R.C. Jaklevic. Molecular vibration spectra by inelastic electron tunneling. Phys. Rev. 165, 821 (1968).

83. J. Lambe and R.C. Jaklevic. Molecular excitations in barriers I, in Tunneling Phenomena in Solids, Edited by E. Burstein and S. Lundquist. (Plenum Press, New York, 1969) p. 233.
84. J.D. Langan and P.K. Hansma. Can the concentration of surface species be measured with inelastic electron tunneling? Surface Sci. 52, 211 (1975).
85. B.F. Lewis, M. Mosesman, and W.H. Weinberg. The chemisorption of  $H_2O$ ,  $HCOOH$  and  $CH_3COOH$  on thin amorphous films of  $Al_2O_3$ . Surface Sci. 41, 142 (1974).
86. E.R. Lippincott. The vibrational spectra and structure of the aluminum hydride ion. J. Chem. Phys. 17, 1351 (1949).
87. L.H. Little. Infrared Spectra of Adsorbed Species (Academic Press, New York, 1966).
88. D.S. MacIver, H.H. Tobin, and R.T. Barth. Catalytic aluminas I. Surface chemistry of eta and gamma alumina. J. Catalysis 2, 485 (1963).
89. D.S. MacIver, W.H. Wilmot, and J.M. Bridges. Catalytic aluminas II. Catalytic properties of eta and gamma alumina. J. Catalysis 3, 502 (1964).
90. A.J. Maeland, R. Rittenhouse, W. Lahar, and P.V. Romano. Infrared reflection-absorption spectra of anodic oxide films on aluminum. Thin Solid Films 21, 67 (1974).

91. R. Magno and J.G. Adler. Inelastic electron-tunneling study of barriers grown on aluminum. Phys. Rev. B 13, 2262 (1976).
92. R. Magno, M.K. Konkin and J.G. Adler. Effect of cover electrode metal on inelastic electron tunneling structure. Surface Sci. 69, 437 (1977).
93. R. Magno and J.G. Adler. Intensity and line-shape measurements in inelastic electron tunneling spectroscopy. J. Appl. Phys. 49, 5571 (1978).
94. M. Malfese and W.J. Orville-Thomas. The infrared spectra and structure of some complex hydroxosalts. J. Inorg. Nucl. Chem. 29, 2533 (1967).
95. J.C. McLennan and G.M. Shrum. On the origin of the auroral green line  $5577 \text{ \AA}$ , and other spectra associated with the aurora borealis. Proc. Roy. Soc. (A) 108, 501 (1925).
96. J.C. McLennan and H.J.C. Ireton. On the spectroscopy of the auroral green line radiation. Proc. Roy. Soc. (A) 129, 31 (1930).
97. H.B. Michaelson. The work function of the elements and its periodicity. J. Appl. Phys. 48, 4729 (1977).
98. J.L. Miles and P.H. Smith. The formation of metal oxide films using gaseous and solid electrolytes. J. Electrochem. Soc. 110, 1240 (1963).
99. M.R. Mohammad and W.F. Sherman. Infrared and Raman spectra of  $\text{ReO}_4^-$  isolated in alkali halides. J. Phys. C 14, 283 (1981).

100. N.F. Mott. A theory of the formation of protective oxide films on metals. Trans. Faraday Soc. 35, 1175 (1939).
101. N.F. Mott. The theory of the formation of protective oxide films on metals, II. Trans. Faraday Soc. 39, 472 (1940).
102. N.F. Mott. The theory of the formation of protective oxide films on metals - III. Trans. Faraday Soc. 43, 429 (1947).
103. J.B. Peri. Infrared and Gravimetric study of the surface hydration of  $\gamma$ -alumina. J. Phys. Chem. 69, 211 (1965).
104. J.B. Peri. A model for the surface of  $\gamma$ -alumina. J. Phys. Chem. 69, 220 (1965).
105. C.M. Phillippi. Analytical infrared spectra of (particulate alpha-aluminas. Developments in Applied Spectroscopy 7B, 23 (1968).
106. S.R. Pollack and C.E. Morris. Electron tunneling through asymmetric films of thermally grown  $Al_2O_3$ . J. Appl. Phys. 35, 1503 (1964).
107. S.R. Pollack and C.E. Morris. Tunneling through gaseous oxidized films of  $Al_2O_3$ . Trans. AIME 233, 497 (1965).
108. C.P. Poole. Electron Spin Resonance (Interscience, New York, 1967) p. 395.
109. J.S. Rogers, J.G. Adler, and S.B. Woods. Apparatus for measuring characteristics of superconducting

- tunnel junctions. *Rev. Sci. Instr.* 35, 208 (1964).
110. D.J. Scalapino and S.M. Marcus. Theory of inelastic electron-molecule interactions in tunnel junctions. *Phys. Rev. Lett.* 18, 459 (1967).
111. D. Scargill. Deformation frequencies of OH groups in nitrosylruthenium complexes. *J. Chem. Soc.*, 4444 (1961).
112. W. Schattke and G.K. Birkner. Theory for impurity assisted tunneling. *Z. Physik* 252, 12 (1972).
113. O.I. Shklyarevskii, A.A. Lysykh, and I.K. Yanson. Study of the composition of the barrier layer and various mechanisms in tunnel contacts on aluminum base. *Sov. J. Low Temp. Phys.* 4, 717 (1978).
114. R.M. Silverstein and G.C. Bassler. Spectrometric Identification of Organic Compounds. (J. Wiley & Sons, Inc., New York, 1967).
115. J.G. Simmons. Intrinsic fields in thin insulating films between dissimilar electrodes. *Phys. Rev. Lett.* 10, 10 (1963).
116. M.G. Simonsen and R.V. Coleman. Tunnelling measurements of vibrational spectra of amino acids and related compounds. *Nature* 244, 218 (1973).
117. H. Stammreich, D. Bassi, and O. Sala. Raman spectrum and force constants of the chromate ion. *Spectrochim. Acta* 12, 403 (1958).
118. D. Steele. Theory of Vibrational Spectroscopy (Saunders, Philadelphia, 1971).



119. H.A. Szymanski. IR Theory and Practice of Infrared Spectroscopy. (Plenum Press, New York, 1964).
120. T. Takamura, H. Kihara-Morishita, and U. Moriyama. Infrared reflectance spectra of barrier-type anodic oxide films formed on pure aluminum. *Thin Solid Films* 6, R17 (1970).
121. P. Tarte. Infra-red spectra of inorganic aluminates and characteristic vibrational frequencies of  $\text{AlO}_4$  tetrahedra and  $\text{AlO}_6$  octahedra. *Spectrochim. Acta* 23A, 2127 (1967).
122. A.V. Uvarov. Infra-red investigation of the interaction between water and an aluminum oxide surface. *Russ. J. Phys. Chem.* 36, 717 (1962).
123. A.V. Uvarov, T.V. Antipina, and S.P. Tikhomirova. Application of infrared spectroscopy in the study of the surfaces of certain modifications of alumina. *Russ. J. Phys. Chem.* 41, 1647 (1967).
124. I. Valetton. Bauxites. *Developments in Soil Science* 1. (Elsevier, Amsterdam, 1972).
125. W. Vedder and D.A. Vermilyea. Aluminum + water reaction. *Trans. Faraday Soc.* 65, 561 (1969).
126. E.J. Verwey. Incomplete atomic arrangement in crystals. *J. Chem. Phys.* 3, 592 (1935).
127. W.H. Weinberg. Inelastic electron tunneling spectroscopy: A probe of the vibrational structure of surface species. *Ann. Rev. Phys. Chem.* 29, 115 (1978).

128. L.A. Woodward and H.L. Roberts. The Raman and infrared absorption spectra of osmium tetroxide. Trans. Faraday Soc. 52, 615 (1956).
129. I.K. Yanson, N.I. Bogatina, B.I. Verkin, and O.I. Shklyarevskii. Asymmetry of tunnel spectrum intensities of impurity organic molecules. Sov. Phys. JETP 35, 540 (1972).

APPENDIX 1

INSTABILITY PAPERS

January 31, 1983

I, Richard Magno, grant permission for the following papers to be used in the appendices of the thesis "Annealing Effects in Tunnel Junctions" by M.K. Konkin:

R. Magno, M.K. Konkin and J.G. Adler. Surface Sci. 69, 437 (1977).

M.K. Konkin, R. Magno and J.G. Adler. Solid State Commun. 26, 645 (1978).

M.K. Konkin, R. Magno and J.G. Adler. Solid State Commun. 26, 949 (1978).

Richard Magno

*Richard Magno*

DEPARTMENT OF PHYSICS  
403) 432-4127 (CHAIRMAN'S OFFICE)  
403) 432-5298 (GENERAL OFFICE)



THE UNIVERSITY OF ALBERTA  
EDMONTON, CANADA  
T6G 2J1

January 31, 1983

I, J.G. Adler, grant permission for the following papers to be used in the appendices of the thesis "Annealing Effects in Tunnel Junctions" by M.K. Konkin.

M.K. Konkin and J.G. Adler. J. Appl. Phys. 50, 8125 (1979).

M.K. Konkin and J.G. Adler. Suppl. au Journal de Physique C-6, 591 (1978)

R. Magno, M.K. Konkin and J.G. Adler. Surface Sci. 69, 437 (1977).

M.K. Konkin, R. Magno and J.G. Adler, Solid State ~~Commun.~~ 26, 645 (1978).

M.K. Konkin, R. Magno and J.G. Adler. Solid State ~~Commun.~~ 26, 949 (1978).

M.K. Konkin and J.G. Adler. J. Appl. Phys. 50, 8125 (1979).

M.K. Konkin and J.G. Adler. J. Appl. Phys. 51, 5450 (1980).



J.G. Adler

JGA/rn

## Instabilities in thin tunnel junctions<sup>a)</sup>

M. K. Konkin and J. G. Adler

Department of Physics, University of Alberta, Edmonton, Alberta T6G 2J1 Canada  
(Received 21 November 1977; accepted for publication 22 January 1978)

Tunnel junctions prepared for inelastic electron tunneling spectroscopy are often plagued by instabilities in the 0–500-meV range. This paper relates the bias at which the instability occurs to the barrier thickness.

PACS numbers: 73.40.Gk, 74.90.+r, 85.25.+k

Recent interest in inelastic electron tunneling spectroscopy (IETS) has necessitated quick and convenient fabrication techniques for stable tunnel junctions. However, in the study of junctions from 0 to 500 meV, instabilities are often seen. The instability shows up as a large noisy patch in the second derivative signal  $d^2I/dV^2 = d\sigma/dV$ , where  $I$  is the current,  $V$  is the voltage, and  $\sigma$  is the conductance. Figure 1 shows three tunneling spectra with instabilities present.

The junctions in this study were prepared by first evaporating an aluminum base film onto a clean glass slide. A plasma discharge of either oxygen, methane, or oxygen followed by methane formed the barrier. Although this work deals only with three types of plasma-prepared barriers, these instabilities are also seen in junctions with thermally grown, liquid-doped, and vapor-doped barriers. After evaporating lead top electrodes, the junctions were cooled to 77 K in liquid nitrogen. The spectra for these junctions were obtained at 4.2 K over a range 0–500 meV using an updated version of the bridge-minicomputer system described by Adler and Straus.<sup>1</sup>

The data collected often showed instabilities. By

looking at several dozen junctions it was found that the position of the instability was related to the product  $RA$  (which is proportional to the barrier thickness<sup>2</sup>) where

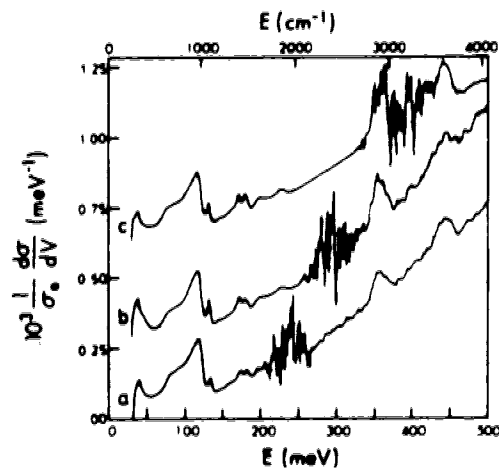


FIG. 1. These three offset curves (A) negative illustrate the shift of instability position with increasing  $RA$ . For these junctions which were prepared by putting different amounts of methane on an oxide,  $RA$  is (a)  $1.83 \Omega \text{ mm}^2$ , (b)  $4.46 \Omega \text{ mm}^2$ , and (c)  $8.23 \Omega \text{ mm}^2$ .

<sup>a)</sup>Supported in part by the National Research Council of Canada.

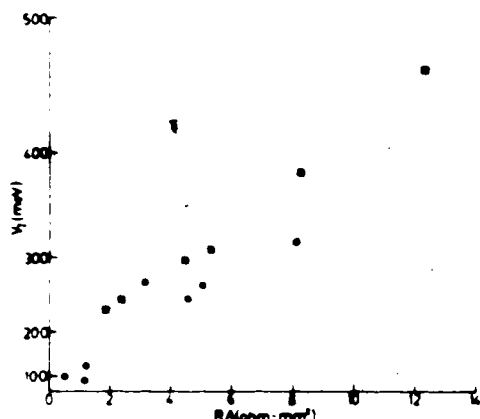


FIG. 2. This figure shows the instability position,  $V_i$  (center of the instability), plotted on a quadratic scale against  $RA$ . The circles represent junctions with an oxide barrier, while the squares are for barriers made of methane plasma discharged on an oxide. Note that the methane plus oxide plot will intercept the ordinate at a positive value, while the single layer (oxide) appears to pass through the origin.

$R$  is the zero bias resistance at 77 K and  $A$  is the junction area. Figure 1 illustrates how the instability position,  $V_i$ , shifts with a change in  $RA$ .<sup>3</sup> At a high enough value of  $RA$  one no longer sees instabilities in the 0–500-meV range. Figure 2 shows the instability position,  $V_i$ , on a quadratic scale against  $RA$ . The different values of  $RA$  were obtained by varying the oxygen and methane plasma discharge times during junction fabrication. The quadratic relationship between the instability position and  $RA$  suggests that the explanation of these instabilities involves the power dissipation of the junction.

All the data shown were from junctions studied within a day or two of preparation. There are indications that

the instability position changes with thermal cycling and aging, shifting it to higher bias.

When an instability is present it seems to affect the IET spectrum only as far as noise is concerned. At biases below the instability the signal is relatively quiet, while above it the noise level is increased (Fig. 1). The widths of observed instabilities range from a few meV up to ~100 meV. Another property of the instability is that it moves to lower and lower bias voltage as the magnetic field applied to a junction is increased, vanishing near or above the critical field of bulk Pb (e.g., ~1 kOe for an instability of ~280 meV zero field position).

In conclusion, the thinner the barrier the lower the bias at which instabilities occur. Because this often masks peaks of interest to IETS, junction preparation parameters should be adjusted to produce a thickness (i.e., an  $RA$  value) such that instabilities will not be present in the region of interest. If  $RA$  is chosen so that instabilities occur only above the region of interest, reasonable signal-to-noise ratios are obtained, so long as junction resistances are kept low. Finally, the quadratic relationship between the instability position and  $RA$  suggests that an instability model should involve power dissipation in the junction.

<sup>1</sup>J.G. Adler and J. Straus, Rev. Sci. Instrum. 46, 158 (1975).

<sup>2</sup>R. Magno, M.K. Konkin, and J.G. Adler, Surf. Sci. 60, 437 (1977).

<sup>3</sup>It should be noted that the center of the instability  $V_i$  differs slightly depending on bias polarity with  $V_i$  for Al positive being closer to zero bias by about 10 meV or less.

A STUDY OF INSTABILITIES IN SUPERCONDUCTING TUNNEL JUNCTIONS†

M.K. Konkin and J.G. Adler

Department of Physics, University of Alberta Edmonton, Alberta, Canada T6G 2J1

Résumé.- Les jonctions à effet tunnel supraconducteurs présentent souvent des instabilités. Cet article relie la tension à laquelle l'instabilité se produit à l'épaisseur de la barrière et démontre la dépendance de la position de l'instabilité au champ magnétique.

Abstract.- Superconducting tunnel junctions often exhibit instabilities. This paper relates the bias at which the instability occurs to the barrier thickness, as well as showing the magnetic field dependence of the instability position.

Superconducting tunnel junctions find many applications in the study of : phonon spectra of superconductors, inelastic excitations in the junction barrier, etc... It is therefore of prime importance to have quick and convenient fabrication techniques for stable tunnel junctions. An instability shows up as a large noisy patch in the second derivative  $\frac{d^2I}{dV^2} \equiv \frac{d\sigma}{dV}$  where  $I$  is the current,  $V$  the voltage, and  $\sigma$  the junction conductance. The insert in Figure 1 shows three tunneling spectra with instabilities present.

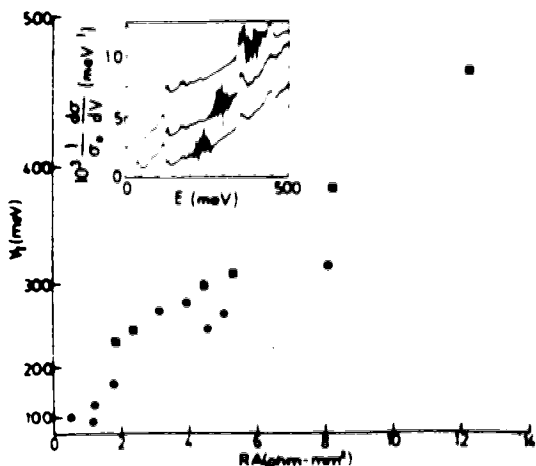


Fig. 1 : This figure shows the instability position  $V_I$  (center of the instability), plotted on a quadratic scale against  $RA$ . Circles represent junctions with an oxide barrier, while squares are for barriers made of methane plasma discharged on an oxide. The three offset curves (Al-ve) in the insert illustrate the shift of instability position to higher bias with increasing  $RA$ .

The junctions in this study were prepared by first evaporating an aluminium base film onto a clean glass slide. A plasma discharge of either oxygen, methane, or oxigen followed by methane formed the barrier. Although this work deals only with three types of plasma prepared barriers, these instabilities are also seen in junctions with thermally grown, liquid-doped and vapor-doped barriers. After evaporating lead top electrodes, the junctions were cooled to 77 K in liquid nitrogen. The spectra for these junctions were obtained at 4.2 K over a range of 0-500 meV using an updated version of the bridge-minicomputer system described by Adler and Straus //.

The data collected often showed instabilities. By looking at several dozen junctions it was found that the position of the instability was related to the product  $RA$  (which is proportional to the barrier thickness //2// where  $R$  is the zero bias resistance at 77 K and  $A$  is the junction area. Figure 1 illustrates how the instability position,  $V_I$ , shifts with a change in  $RA^2$ . At a high enough value of  $RA$  one no longer sees instabilities in the 0-500 meV range. Figure 1 also shows the instability position,  $V_I$ , on a quadratic scale against  $RA$ . The different values of  $RA$  were obtained by varying the oxigen and methane plasma discharge times during junction fabrication. The quadratic relationship between the instability position and  $RA$  suggests that the explanation of these instabilities involves the power dissipation of the junction. A study of the behaviour of the instability in a magnetic field (Figure 2) shows that it moves to a lower and lower voltage as the field is increased. The plot is shown in reduced field units

†Supported in part by the National Research Council of Canada.



C6-592

to take into account the slight variation in critical field from junction to junction.

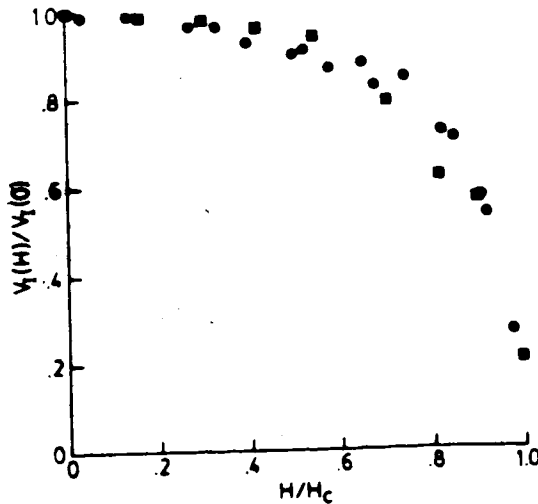


Fig. 2 : Instability position vs applied magnetic field for two different oxide junctions is shown here in reduced units.  $V_I(H)$  is the field dependent instability position,  $V_I(0)$  is the zero field value - for circles  $V_I(0) = 173$  meV while for squares it is 279 meV - and  $H_c$  is the critical field.

Instabilities present in a junction seem to affect the spectrum only insofar as noise is concerned. In general the noise level is low at voltages below the instability while being somewhat larger above it (see insert Figure 1). The widths of the instabilities have been observed to range from about 1meV to about 10meV. The data presented here was obtained within a day or two of junction preparation. There is some evidence that the instability position shifts to higher bias with thermal cycling and junction aging.

In conclusion we have shown that there is a quadratic relationship between the instability position and RA, indicating that power dissipation in the junction is involved. The magnetic field dependence of the instability position, as well as the absence of instabilities in junctions with both electrodes normal indicates that superconductivity is involved.

### References

- /1/ Adler, J.G. and Straus, J., Rev. Sci. Instr. 46 (1975) 158.
- /2/ Magno, R., Konkin, M.K., and Adler, J.G., Surface Sci. 69 (1977) 437.
- /3/ It should be noted that the center of the instability  $V_I$  differs slightly depending on bias polarity with  $V_I$  for A<sub>1</sub> positive being closer to zero bias by about 10meV or less.

APPENDIX 2

IETS PAPERS

Surface Science 69 (1977) 437-443  
© North-Holland Publishing Company

## EFFECT OF COVER ELECTRODE METAL ON INELASTIC ELECTRON TUNNELING STRUCTURE \*

R. MAGNO, M.K. KONKIN and J.G. ADLER

*Department of Physics, University of Alberta, Edmonton, Alberta, Canada T6G 2J1*

Received 13 June 1977; manuscript received in final form 8 August 1977

Inelastic electron tunneling spectra peak intensities have been measured for a group of Al- $M_x$  junctions for which  $M_x$  was Ag, Au, In, Pb, Sn or Zn and the barriers were formed in an ethylene glow discharge. The intensity of the 360 meV peak which is associated with the stretching of carbon-hydrogen bonds was found to increase with junction barrier thickness for a given cover electrode. The intensity decreases as the cover electrode is changed from Ag to Pb, Sn, Au, In, and finally Zn. This order correlates with decreasing ionic radius, suggesting that the decrease in peak intensity is due to the increased penetration of the cover electrode into the insulator, resulting in a thinner barrier.

### 1. Introduction

It has long been known [1-5] that Pb is the optimum metal for use as a cover electrode in metal-insulator-metal tunnel junctions prepared for the purpose of studying inelastic electron tunneling. This paper deals with the variation in intensity of inelastic electron tunneling spectra with junction counter electrode. Data are shown for a series of Al- $M_x$  junctions where  $M_x$  is either Ag, Au, In, Pb, Sn or Zn, and the barriers are made in an ethylene glow discharge [6]. Geiger, Chandrasekhar, and Adler [7] examined the intensity of inelastic structure for various cover electrodes using oxygen glow discharged aluminum base layers and showed a correlation between the intensity and the ionic radius of the cover electrode. Earlier work of Handy [8] which studied resistances as a function of the covering electrode for Al- $M_x$  junctions indicated a correlation between the atomic radius of the counter electrode and the resistance of the junction.

Inelastic electron tunneling manifests itself by an increase in conductance,  $\sigma$ , at energies  $|eV| < \hbar\omega$ , where  $\hbar\omega$  is the threshold energy for the inelastic effect in question [1-5]. The conductance increases since each inelastic excitation adds a new channel to the tunneling process. In the case of a band of molecular vibrations the change in conductance,  $\delta\sigma$ , is rarely more than 2%. For this reason it is advantage-

\* Work supported in part by the National Research Council of Canada.

ous to measure the derivative of the conductance with respect to energy  $d\sigma/dv$ . In this work we have used a measurement system similar to that described by Adler and Straus [9] to obtain values of the intensity

$$I = \int \left[ \frac{1}{\sigma_0} \frac{d\sigma}{dv} - g(v) \right] dv, \quad (1)$$

where  $\sigma_0$  is a value of the conductance at low bias chosen for normalization and  $g(v)$  is the smooth background  $d\sigma/dv$  under the inelastic peak.

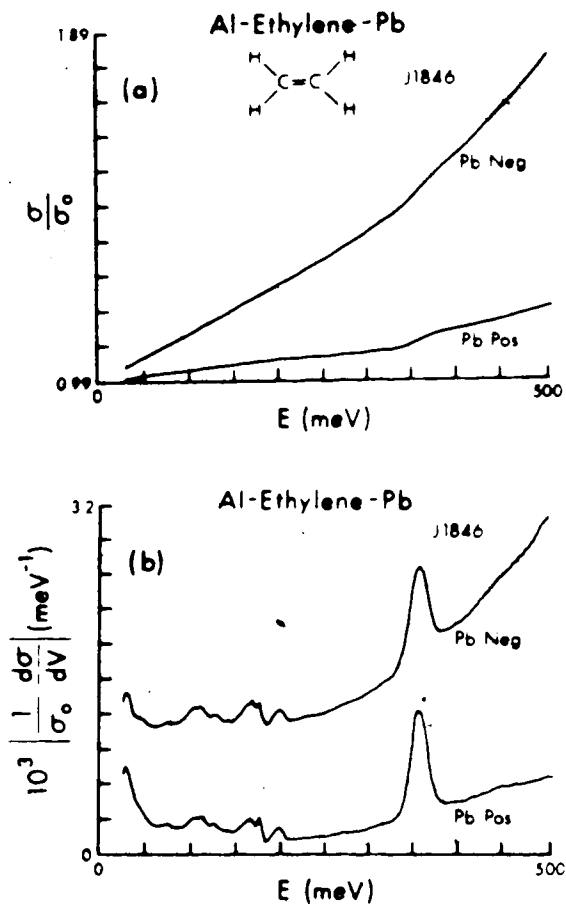


Fig. 1. Conductance (a) and its derivative (b) for a typical Al-Pb junction.  $\sigma_0$  is the value of  $\sigma$  at 35 meV and is used to normalize the curves.

## 2. Experimental

The samples examined in this study consisted of a pair of junctions formed on a common base layer. The base was made by evaporating an aluminum film onto a clean glass slide. The barrier was produced in a dc glow discharge of ethylene. Details of the glow discharge procedure have been reported elsewhere [6]. The two junctions sharing a common base layer and insulating barrier were completed by evaporating a Pb control electrode for the first junction and a metal  $M_x$  for the second junction. Measurements were carried out at 4.2 K in liquid helium and the data were taken on an improved version of the bridge and minicomputer system described earlier [9].

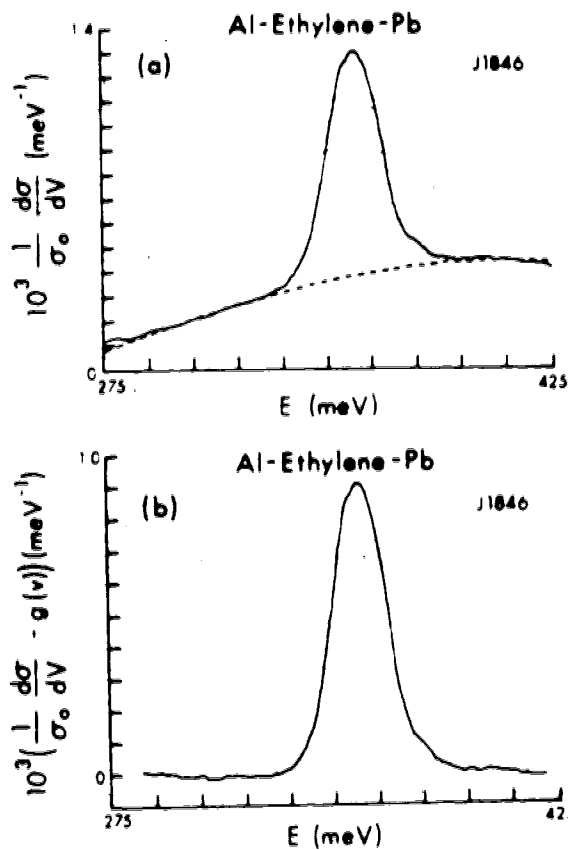


Fig. 2. (a)  $(1/\sigma_0) d\sigma/dv$  near 360 meV with the Pb electrode biased positively for an Al-Pb junction. The dashed curve is the background  $g(v)$ . (b)  $(1/\sigma_0) d\sigma/dv$  with background removed, this curve forms the integrand of eq. (1).

The junctions were swept from 0–500 meV ( $M_x$  positive) except for those with a Pb cover layer for which the region below 35 meV was omitted to avoid saturation of the lock-in amplifiers by structure due to the Pb phonons and the superconducting energy gap.

A typical conductance curve is shown in fig. 1a, while its derivative  $(1/\sigma_0) d\sigma/dv$  is illustrated in fig. 1b. These data and all those shown in this paper have been normalized at 35 meV to allow for comparison of various junctions regardless of junction resistance (the conductance at 35 meV differs from that of zero bias by less than 3% in all cases). A typical high resolution sweep in the 275 to 425 meV range (Pb electrode positive) is illustrated in fig. 2a, along with the dashed background curve,  $g(v)$ . The integrand as used in eq. (1) is shown in fig. 2b. The mini-computer based system [9] allows this background subtraction and the ensuing integration for obtaining intensities to be carried out in a few minutes. All junction pairs were analysed in this way to determine the intensity of the 360 meV peak.

### 3. Results and discussion

Consider first the Al–Pb junctions. The resistance of a junction should increase exponentially with the thickness of the barrier, thus a plot of the intensity versus  $\ln(10RA)$  (where  $R$  is the junction's resistance and  $A$  its cross-sectional area) may be expected to be linear. Such a plot is illustrated in fig. 3. It should be noted that the junction areas varied by almost an order of magnitude from less than  $0.1 \text{ mm}^2$  to greater than  $0.7 \text{ mm}^2$ . The results thus indicate that the tunneling measurement

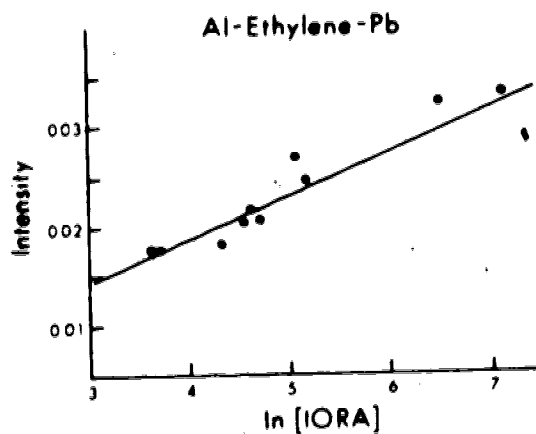


Fig. 3. Intensity of the 360 meV peak plotted against  $\ln(10RA)$  for a group of Al–Pb junctions.

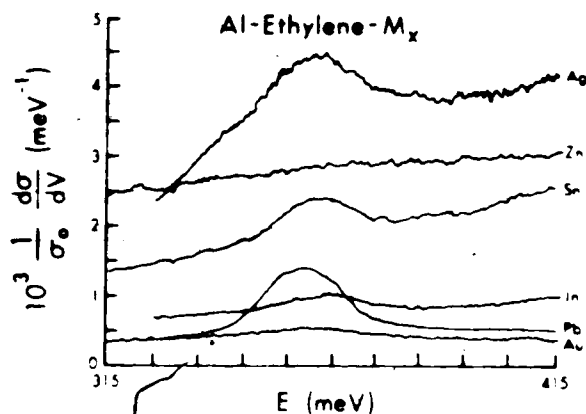


Fig. 4. Typical data for the various covering metals used.

is sampling carbon-hydrogen bonds throughout the volume of the barrier rather than just those near a metal-barrier interface.

We turn our attention now to the variation of intensity due to the cover electrode metal. Those results are shown in fig. 4 and plotted against ionic radius in fig. 5. These results suggest that smaller ionic radius metals penetrate the barrier more, effectively resulting in a thinner barrier junction.

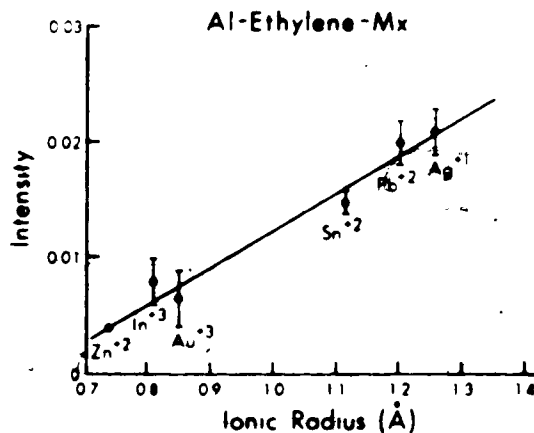


Fig. 5. Intensity of the 360 meV peak versus the ionic radius of the cover metal.

#### 4. Summary

In conclusion, we found that the intensity of the spectra increases with barrier thickness for a given cover electrode (fig. 3), while it depends on the penetration of the cover electrode into the barrier when different covers are used (fig. 5). The distance the metal penetrates depends upon its ionic radius. This conclusion is similar to that reached by Geiger et al., except that the data (fig. 5) are plotted using ionic radii different from those previously used. A comparison is given in table 1. It should be noted that the intensities measured here are those defined by eq. (1), while the data of Geiger, Chandrasekhar, and Adler [7] refer to the relative intensities of the hydrocarbon peak near 360 meV to the alumina hydrate (or alumina) peak near 118 meV. The ionic radii used in the earlier work [7] were those given by Pauling (which list only one oxidation state per element), while we have chosen more frequently occurring oxidation states with perhaps the exception of tin. If one replots the data of Geiger et al. one finds that the radii used in this work actually give better agreement. The important point of both papers is a qualitative one which indicates that the ionic radius is an important parameter in determining the properties of tunnel junctions.

The details of the penetration of the cover metal into the barrier merit further examination. At this point it is not known whether the penetration occurs as the cover metals are deposited or by subsequent diffusion.

It is possible that this experimental technique could be developed further as a method for determining the ionization state of metallic ions in the type of environment existing in tunnel junctions.

Finally it should be pointed out that from fig. 5 one might expect silver to be the optimum cover metal, this however is not so since Al-Ag junctions are noisier than Al-Pb junctions as well as having steeper conductances.

Table 1  
Summary of ionization states and ionic radii

This work		Geiger et al. [7]	
	Radius (Å) [10]		Radius (Å)
Ag <sup>+1</sup>	1.26	Ag <sup>+1</sup>	1.26
Pb <sup>+2</sup>	1.20	Pb <sup>+4</sup>	0.84
Sn <sup>+2</sup>	1.12	Sn <sup>+4</sup>	0.71
Au <sup>+3</sup>	0.85	Au <sup>+1</sup>	1.37
In <sup>+3</sup>	0.81	In <sup>+3</sup>	0.81
Zn <sup>+2</sup>	0.74		



**References**

- [1] J.C. Jaklevic and J. Lambe, *Phys. Rev. Letters* 17 (1966) 1139.
- [2] J. Lambe and R.C. Jaklevic, *Phys. Rev.* 165 (1968) 821.
- [3] C.B. Duke, *Tunneling in Solids* (Academic Press, New York, 1969).
- [4] E.L. Wolf, in *Solid State Physics*, Vol. 30, Eds. H. Ehrenreich, F. Seitz and D. Turnbull (Academic Press, New York, 1975) p. 1.
- [5] For a recent review of inelastic electron tunneling, see P.K. Hansma, *Physics Reports*, to be published.
- [6] R. Magno and J.G. Adler, *Thin Solid Films* 42 (1977) 237.
- [7] A.L. Geiger, B.S. Chandrasekhar and J.G. Adler, *Phys. Rev.* 188 (1969) 1130.
- [8] R.M. Handy, *Phys. Rev.* 126 (1962) 1968.
- [9] J.G. Adler and J. Straus, *Rev. Sci. Instr.* 46 (1975) 158.
- [10] (a) Sargent-Welch, *Table of Periodic Properties of the Elements*.  
(b) Value for  $\text{Au}^{+3}$  *Handbook of Chemistry and Physics*, 49th ed. (Chemical Rubber Publ. Co., Cleveland, 1968) p. F-152.

## ASYMMETRY IN INELASTIC ELECTRON TUNNELING PEAK INTENSITIES\*

M.K. Konkin, R. Magno and J.G. Adler

Department of Physics, University of Alberta, Edmonton, Alberta, Canada T6G 2J1

(Received 6 January 1978 by R. Barrie)

Experiments show that for an organic material placed on an oxide one sees an asymmetry of inelastic electron tunneling peak intensity for bias voltages of opposite sign. When the barrier is composed only of the organic material with no deliberate oxidation such asymmetry disappears.

RECENTLY there has been considerable interest regarding the asymmetry of IETS (inelastic electron tunneling spectroscopy) peak intensities [1]. This asymmetry is manifest in the unequal intensities (arising from molecular vibrations of organic molecules in Al-oxide-organic-Pb junctions) observed at opposite junction bias polarity. When the Al base film is negative with respect to the Pb top film one obtains a larger peak intensity than with reverse polarity.

Yanson *et al.* [2] first looked at peak intensity asymmetries in Sn-Pb and Al-Pb junctions with an organically doped oxide barrier. They showed that an asymmetry does exist and gave reasons to support this. Since they did not use calibrated data (i.e. the second derivative  $d\sigma/dV$ , where  $\sigma$  is the junction conductance as opposed to the 2nd harmonic voltage signal) little more on the subject could reliably be said.

Kirtley, Scalapino and Hansma [3] did theoretical calculations for peak asymmetries. To support their theory, ratios of conductance change  $\Delta\sigma(+V)/\Delta\sigma(-V)$  vs voltage  $V$  were found. The  $\Delta\sigma(V)$  refers to the height of a step in the conductance curve caused by the opening up of a new tunneling channel due to the inelastic excitation of a molecular vibration, for example. For Al-oxide-benzoic acid-Pb data, a plot of  $\Delta\sigma(+V)/\Delta\sigma(-V)$  vs  $V$  was shown to lie near their theoretical curve.

In this work we use absolute IETS peak intensities obtained from calibrated second derivative data to show the asymmetry. Moreover, we demonstrate the lack of asymmetry for a barrier composed of only the organic material with no prior oxidation step.

Tunnel junctions were prepared by first evaporating an aluminum base film onto a clean glass slide. The aluminum film was then oxidized in an oxygen-helium plasma discharge followed by a methane discharge to cover the oxide with a simple organic material. Finally,

a lead top electrode was evaporated to complete the junction (Al-Pb was chosen for best resolution) [4]. The junctions thus produced were studied at 4.2 K and the data were obtained using an updated version of the bridge-minicomputer system described by Adler and Straus [5]. Since we calibrate our data we are able to work with absolute quantities such as  $d\sigma/dV \equiv d^2I/dV^2$  as opposed to raw second harmonic signals, or relative units normalized to some arbitrary peak height.

For the asymmetry study we chose the second derivative peak due to C-H stretching modes occurring near 360 meV because of: (1) its prominence, (2) isolation from other peaks, and (3) the relative ease with which a background can be subtracted.

The peak intensity is calculated from the data by

$$F(V) = \int \left( \frac{1}{\sigma_0} \frac{d\sigma}{dV} - g(V) \right) dV$$

where  $\sigma_0$  is the conductance used to normalize  $d\sigma/dV$  (in this paper  $\sigma_0 = \sigma(-30 \text{ meV})$ , since we did not sweep through zero bias in order to avoid the superconducting energy gap and large Pb phonon peaks) and  $g(V)$  is the smooth background under the inelastic peak [6]. We define [4] an asymmetry parameter  $\alpha(V)$  as

$$\alpha(V) = F(+V)/F(-V)$$

where  $F(+V)$  is the peak intensity when the base film is positive with respect to the top film (i.e. for these junctions Al positive, Pb negative) and  $F(-V)$  is the peak intensity with the base film negative with respect to the top film (i.e. Al negative, Pb positive). When  $F(-V)$  is larger than  $F(+V)$  (as typically occurs for organic vibrations in Al-oxide-organic-Pb junctions)  $\alpha(V) < 1$ .

For junctions with plasma discharged methane on aluminum oxide, the asymmetry  $\alpha(360 \text{ meV})$  ranged from 0.6 to 0.8 (several dozen junctions with varying oxidation and methanation times were studied). Junctions with no prior oxidation discharge gave  $\alpha(360 \text{ meV}) \approx 1$  showing that very little or no asymmetry exists for a barrier made of a single simple material. We have

\* Supported in part by the National Research Council of Canada.

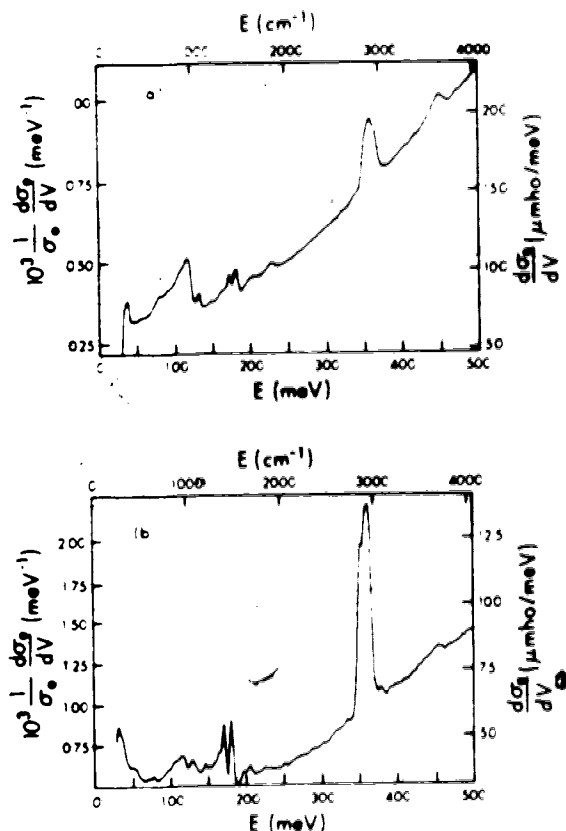


Fig. 1. (a)  $d\sigma_e/dV$  for an Al-oxide-methane-Pb junction. (b)  $d\sigma_e/dV$  for an Al-methane-Pb junction.  $\sigma_e$  is the even part of the junction conductance.

observed similar asymmetries with several formic acid vapor doped on plasma oxidized aluminum junctions, while formic acid vapor deposited on pure aluminum shows  $\alpha$  near unity [7]. Typical results are shown in Figs. 1 and 2.

These results can be understood as follows. In the asymmetric junctions (which have prepared oxide layers) the organic material is closer to the Pb electrode than to the Al one. When electrons tunnel from Al to Pb they cross most of the barrier at a high energy, then lose energy to an inelastic excitation, and have to tunnel only a short distance at low energy. Going from Pb to Al the electron loses most of its energy near the beginning of its journey and thus has to tunnel through most

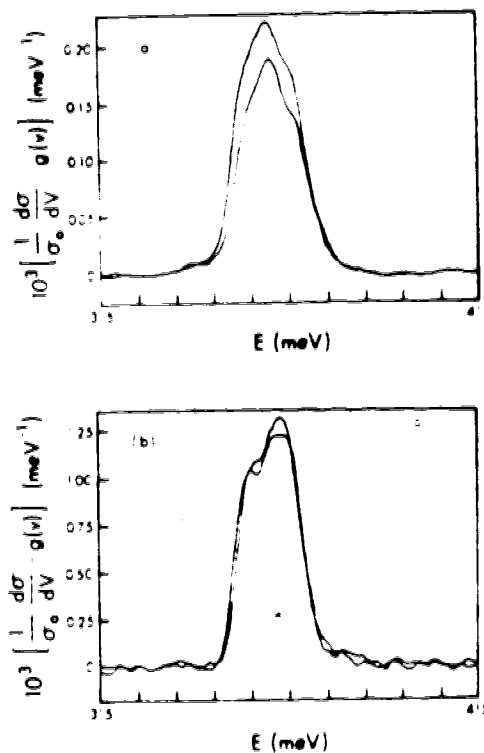


Fig. 2. Peak asymmetry illustrated by plots of  $(1/\sigma_0) \times (d\sigma/dV) - g(V)$  (for the two bias directions) used to calculate the intensities  $F(+V)$  and  $F(-V)$  as described in the text for the two junctions of Fig. 1. For (a)  $\alpha(360 \text{ meV}) \approx 0.81$  and for (b)  $\alpha(360 \text{ meV}) \approx 0.98$ .

of the barrier at low energy. Because the probability of tunneling diminishes as the electron energy decreases, fewer electrons will get through the barrier in the latter case. Hence, one sees a greater inelastic tunneling intensity for Al negative with respect to Pb than vice versa.

In conclusion we have shown that by using absolute inelastic electron tunneling peak intensities one can study peak asymmetry. For barriers composed of an organic material on an oxide one sees a definite asymmetry, while for a barrier made of the organic substance alone the asymmetry disappears. Our observations thus clarify the earlier confusion [1] which motivated this study. Finally it should be noted that this method may be used to determine whether a barrier is homogeneous ( $\alpha \approx 1$ ) or heterogeneous ( $\alpha \neq 1$ ).

#### REFERENCES

1. *Inelastic Electron Tunneling Spectroscopy* (Edited by WOLFRAM T.). Springer Verlag (1978).
2. YANSON I.K., BOGOTINA N.I. & SHKLYAREVSKI O.I., *Zh. Eksp. Teor. Fiz.* 62, 1023 (1972) [*Sov. Phys. JETP* 35, 540 (1972)].
3. KIRTLEY J., SCALAPINO D.J. & HANSMA P.K., *Phys. Rev.* B14, 3177 (1976).

4. ADLER J.G., KONKIN M.K. & MAGNO R., The Technology of IETS, in *Inelastic Electron Tunneling Spectroscopy* p. 146 (Edited by WOLFRAM T.), Springer Verlag (1978).
5. ADLER J.G. & STRAUS J., *Rev. Sci. Instrum.* **46**, 158 (1975); ADLER J.G., MAGNO R. & KONKIN M.K. (to be published).
6. MAGNO R., KONKIN M.K. & ADLER J.G., *Surf. Sci.*, **69**, 437 (1977).
7. MAGNO R. & ADLER J.G., *J. Appl. Phys.* (in press).

## THE USE OF BARRIER PARAMETERS FOR THE CHARACTERIZATION OF ELECTRON TUNNELING CONDUCTANCE CURVES\*

M. K. Konkin, R. Magno and J. G. Adler

Department of Physics, University of Alberta, Edmonton, Alberta, Canada T6G 2J1

(Received 22 February 1978 by R. Barrie)

This paper deals with barrier parameters calculated from the coefficients of polynomial fits to electron tunneling conductance curves for a large sample of junctions with various types of barriers. Methods of data handling, along with a comparison of the results from two different parameter calculations are shown. Finally, relationships between the barrier parameters and other junction characteristics - particularly  $RA$ , the product of junction resistance with area (a simple and extremely useful parameter) - are discussed.

THEORETICAL tunnel conductance calculations have been carried out by Simmons [1]. These have been extended and discussed by others, in order to deal with the calculation of barrier parameters using the fitting coefficients derived from electron tunneling conductance curves. The parameters are the barrier thickness  $s$ , the average barrier height  $\phi$  ( $\phi = \frac{1}{2}[\phi_1 + \phi_2]$  at zero bias), and  $\Delta\phi = \phi_2 - \phi_1$  the difference of the barrier heights at the two electrodes. Using the methods of Brinkman, Dynes, and Rowell [2] (BDR), and Albrecht, Keller, and Thieme [3] (AKT) parameters have been calculated for a sample of approximately fifty junctions with various barriers (e.g. sulfides, organics, and oxides plus organics). A comparison of these parameters, along with fitting methods and data handling are shown. Since independent measurements of  $s$  [4],  $\phi$  [5] and  $\Delta\phi$  have not been made, little can be said about a comparison between experimental and calculated values. There do, however, exist relationships between the calculated  $s$ ,  $\phi$  and  $\Delta\phi$  and simple junction parameters, such as  $RA$  (where  $R$  is the junction resistance and  $A$  its area) which provides a quick characterization of the junction properties. These will be discussed.

Junctions used in this study were prepared by first evaporating an aluminum base film onto a clean glass substrate. Exposure of the base film to a plasma discharge of oxygen, methane, ethylene, fluoroform, or oxygen followed by methane formed the barriers. Evaporation of lead top electrodes completed the junctions (areas ranged from 0.06 to 0.72 mm<sup>2</sup> and resistances from 10 to 2000  $\Omega$ ). Measurements were taken at 4.2 K using an updated version of the bridge-minicomputer system described by Adler and Straus [6].

To calculate barrier parameters, we used the coefficients  $b_0$ ,  $b_1$  and  $b_2$  of a polynomial fit to the normalized tunneling conductance curve  $\sigma(V)/\sigma_N = b_0 + b_1V + b_2V^2 + \dots$  where  $\sigma(V)$  is the derivative of current with respect to voltage and  $\sigma_N = \sigma(-30 \text{ meV})$ . This normalizing bias was chosen because all junctions in this study had superconducting Pb cover electrodes. In order to avoid large structure due to Pb phonons and the energy gap, our sweep avoided the  $\pm 30 \text{ meV}$  region. Because of this,  $R$  is taken as  $1/\sigma_N$ . The fitting region used was typically 150-500 meV (using a 6th degree polynomial for convenience). This avoided the zero bias region and any low energy inelastic structure, thus concentrating on the elastic part of the conductance [Fig. 1(a)]. The fitting of oxide or oxide plus methane data was fairly easy due to a lack of prominent inelastic tunneling structure above 150 meV [Fig. 1(a)]. Data from junctions with organic barriers such as ethylene presented a problem because of the large conductance step at 360 meV (due to C-H stretching). This was solved by lowering data above the step by the step height and then performing the fit; two regions were used in this case 185-345 meV and 380-499 meV [Fig. 1(b)]. The same procedure was used for fluoroform and methane data. By using the minicomputer system, data handling and polynomial fits could be carried out quickly and easily.

Once the coefficients were extracted, barrier parameters were calculated using the methods of BDR and AKT. The difference in the numbers obtained by the two methods for  $s$  and  $\phi$  is negligible. For example, the values of  $s_{\text{AKT}}$  which turn out to be larger than those for  $s_{\text{BDR}}$  deviate approximately 0.03 Å over a range of 10.5-14.5 Å. For  $\phi$  the maximum deviation is about 0.002 V from  $\sim 2.0$ -3.5 V and  $\phi_{\text{AKT}}$  is again greater than  $\phi_{\text{BDR}}$ . Since the earlier work of BDR gives

\* Supported in part by the National Research Council of Canada.

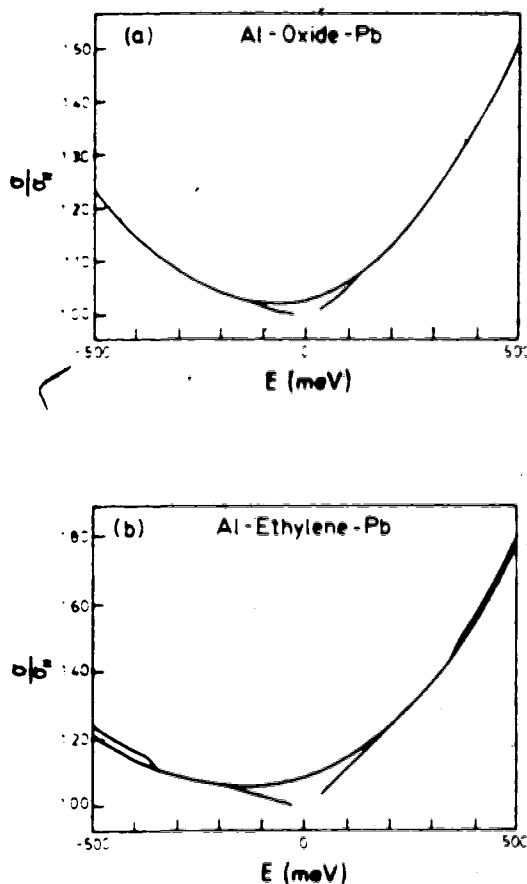


Fig. 1. (a) Polynomial fit for an Al-oxide-Pb junction. The fitting region is from 150–500 meV. (b) Polynomial fit for an Al-ethylene-Pb junction. The fitting regions are 185–345 and 380–500 meV to avoid the 360 meV conductance step. Beyond 380 meV the polynomial fit parallels the conductance curve.

satisfactory parameters, the rest of the numbers used in this paper will be those calculated using this method [(BDR method I – WKB approximation using equation (7)).

When calculating a set of parameters for comparison or graphical purposes, one should use the same general fitting region for the whole data set. Depending on the fitting region, the parameter values change. For a particular fitting region, however, the same trends among the parameters remain.

In Fig. 2, a plot of  $\phi$  vs  $s$  for Al-ethylene-Pb data, fit in the 185–345 and 380–500 meV regions is shown. Chosen for a wide range of  $s$  and  $\phi$  values, the data points, at first glance seem scattered with a general trend of decreasing  $\phi$  as  $s$  increases. Looking at  $RA$  values, however, one sees that  $RA$  increases from left to right along the arrow direction, with data points of the same  $RA$  value (e.g. 11.0–11.5  $\Omega\text{-mm}^2$ ) lying along a line perpendicular to the arrow direction. These lines are

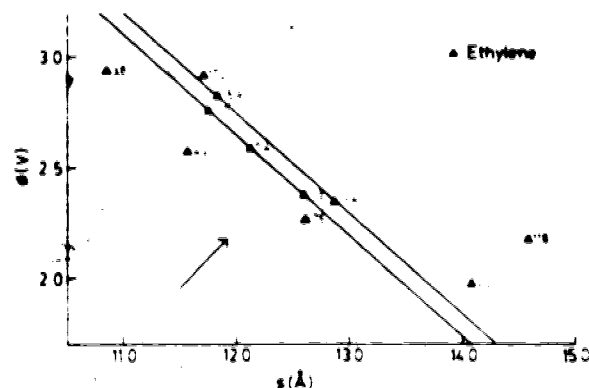


Fig. 2. This figure shows  $\phi$ , the average barrier height plotted against  $s$  the barrier thickness. The numbers beside the data points give their  $RA$  ( $\Omega\text{ nm}^2$ ) values. Points with the same  $RA$  values define straight lines parallel to each other. Going from left to right along the direction normal to the lines (indicated by the arrow) one sees that  $RA$  increases. There is thus some order to a seemingly scattered plot.

actually gentle curves described by  $s\phi^{1/2} = C$  with the constant  $C$  dependent on  $RA$ . How to determine the constant will be shown later.

The exponential dependence of tunneling current on barrier thickness can be demonstrated by plotting  $s\phi^{1/2}$  against  $\ln(RA)$ . As shown in Fig. 3 this yields a straight line which is fairly independent of the barrier's chemical composition; data includes oxide, oxide plus methane, fluoroform, methane, ethylene, and also junctions with contamination (e.g. formic acid recognized by its spectrum) or instabilities [7]. When present, an instability shows up as a noisy patch in the  $d\sigma/dV$  curve. The instability region for the 0–500 meV range is below  $RA \approx 18$ . Also, by looking at this graph one can determine the  $RA$  dependent constant  $C$ , previously mentioned, such that  $s\phi^{1/2} = C$ . The equation for the line determined by the data (with the exception of the ethylene data which tend to deviate from it) is given by  $s\phi^{1/2} = 0.961 \ln(RA) + 17.33$ . For junctions with different base or cover electrodes data points do not generally fall on this line.

The data also show a relation between  $\Delta\phi/\phi$  and  $\Delta\sigma/\sigma$ , where

$$\Delta\sigma = \frac{\sigma(+500) - \sigma(-500)}{\sigma_N}$$

and

$$\phi = \frac{1}{2} \left[ \frac{\sigma(+500)}{\sigma_N} + \frac{\sigma(-500)}{\sigma_N} \right]$$

using a normalized conductance curve. This can be thought of as a steepness difference in the conductance curve for two bias polarities and may also be written as

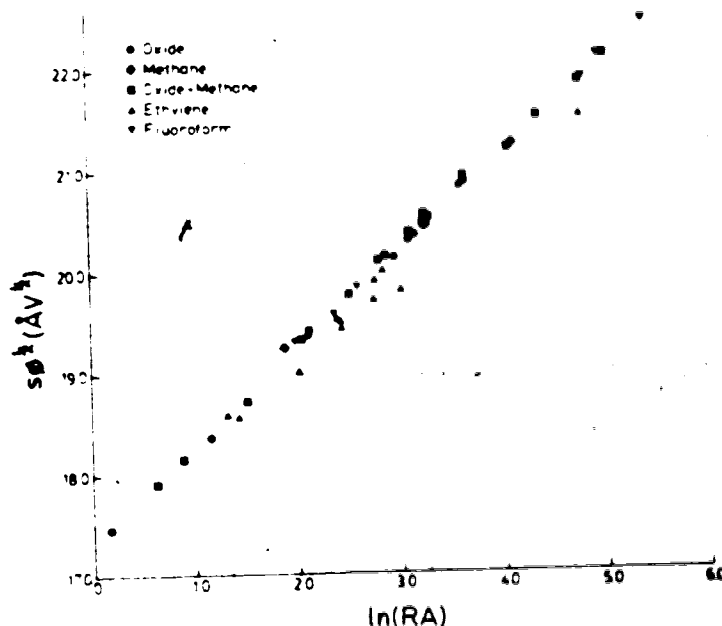


Fig. 3. A graph of  $s\phi^{1/2}$  vs  $\ln(RA)$ . Data is shown for junctions with barriers formed in a plasma discharge of oxygen, methane ( $\text{CH}_4$ ), oxygen followed by methane, fluoroform ( $\text{CHF}_3$ ), or ethylene ( $\text{C}_2\text{H}_4$ ).

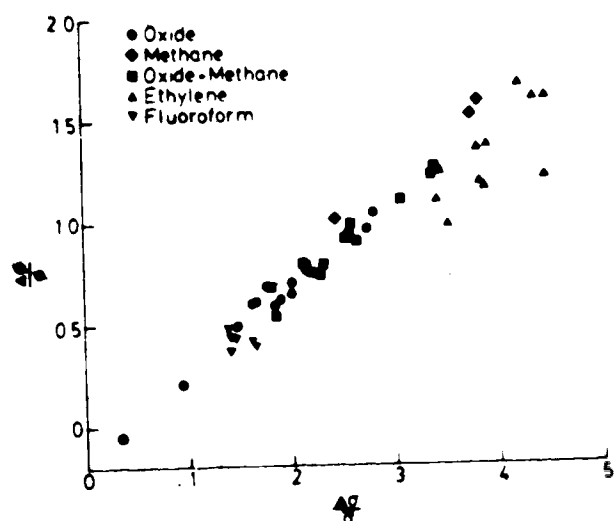


Fig. 4. This figure shows the linear relationship between  $\Delta\phi/\phi$  and  $\Delta\sigma/\sigma$ . It should be noted that the ethylene points which show more scatter than the rest of the data are also those which deviate from the line in Fig. 3.

$$\frac{\Delta\sigma}{\sigma} = \frac{2[\sigma(+500) - \sigma(-500)]}{\sigma(+500) + \sigma(-500)}$$

The resultant linear plot is shown in Fig. 4. Looking at this graph, the ethylene points show noticeably more scatter than the rest of the data. This fact, along with the deviation on the  $s\phi^{1/2}$  vs  $\ln(RA)$  graph (the points which deviate in Fig. 3 also do so in Fig. 4) suggests that there is something different about ethylene.

If one returns to Fig. 3 one sees that this is not the plot one would use specifically for plotting the data [i.e. according to BDR one would use  $\ln(RA)$  vs  $1.025s\phi^{1/2} + \ln(s/\phi^{1/2})$ ] but rather a simplified expression which works quite well for the majority of junctions. Plotting the complete expression, one obtains the expected straight line with no data point deviation. The term thus responsible for the ethylene deviation involves  $s/\phi^{1/2}$ . For the other junctions this factor is fairly constant, while for ethylene it tends to be larger. Comparing our expansion with the BDR expression for parameter calculation one finds that  $b_2 = B(s^2/\phi)$  (i.e. the quadratic coefficient is proportional to  $s^2/\phi$ ) where  $B$  is a constant. For the deviant ethylene points  $b_2$  is larger than for the other barrier types. Going back to Fig. 4 one sees that for the more scattered ethylene values,  $\Delta\phi/\phi$  is smaller than expected for a given  $\Delta\sigma/\sigma$  value. Using  $b_1$ , one can express  $\Delta\phi/\phi$  as  $Db_1(\phi^{1/2}/s)$  where  $D$  is a constant. In this expression, the inverse of  $s/\phi^{1/2}$  is involved and thus  $\Delta\phi/\phi$  will be smaller than expected. If one uses a value of  $s/\phi^{1/2}$  which for other junctions is fairly constant to calculate  $\Delta\phi/\phi$ , one finds that the scatter of Fig. 4 is reduced.

The way that the larger quadratic coefficient,  $b_2$ , manifests itself is in the shape of the conductance curve (in the fitting region). The shapes of ethylene curves are different from those of the other barrier types. Whereas the curves of the others exhibit a fairly smooth curved shape of conductance in the fitting region used, the ethylene curves do not show this type of behavior over

the whole range, but have instead a flatter region between 185 and 300 meV. Indeed, if data are fit in the 380–500 meV region where the smooth curvature does exist, the deviation in Fig. 3 is eliminated and the scatter in Fig. 4 reduced. The cause of the different curvature is not known, however it may be due to a difference in barriers formed from the plasma discharge products of a double-bonded organic (e.g. ethylene) as opposed to those produced from a single bonded organic material (e.g. methane or fluoroform). It would be a project by itself to determine what is actually happening.

In conclusion, one finds that for a wide range of junction resistances and area, the conductance can be represented by:  $\sigma_N = kA e^{-\beta\phi^{1/2}}$  where  $k = e^{1.04\phi}$  and  $\beta = 1.041$ . The constants  $k$  and  $\beta$  are not related to the material forming the barrier but rather to the electrode materials. The scatter observed for ethylene barriers is due to a relatively large quadratic coefficient resulting in a value of  $s/\phi^{1/2}$  which is larger than the fairly constant value obtained for other barrier types. Finally, a linear relation exists between  $\Delta\phi/\phi$  and  $\Delta\sigma/\sigma$ .

#### REFERENCES

1. SIMMONS J.G., *J. Appl. Phys.* **34**, 2581 (1963).
2. BRINKMAN W.F., DYNES R.C. & ROWELL J.M. *J. Appl. Phys.* **41**, 1915 (1970).
3. ALBRECHT H., KELLER G. & THIEME F., *Surf. Sci.* **69**, 677 (1977).
4. KNORR K. & LESLIE J.D., *Solid State Commun.* **12**, 615 (1973).
5. FOWLER R.H. & NORDHEIM L., *Proc. R. Soc. (Lond.)* **A119**, 173, (1928).
6. ADLER J.G. & STRAUS J., *Rev. Sci. Instrum.* **46**, 158 (1975).
7. KONKIN M.K. & ADLER J.G., *Appl. Phys. Lett.* **32**, 436 (1978).



## Annealing effects in tunnel junctions (thermal annealing)

M. K. Konkin and J. G. Adler

Department of Physics, University of Alberta, Edmonton, Alberta, Canada, T6G 2J1

(Received 12 April 1979; accepted for publication 2 August 1979)

This paper describes the results of subjecting Al-oxide-Pb tunnel junctions to thermal annealing. By looking at the junction resistance, barrier parameters (thickness, average barrier height, and the separation between the barrier heights at the Al and Pb electrodes), and inelastic electron tunneling (IET) peak intensities, one can study time-dependent effects occurring in the junction. These observations indicate changes in the tunneling barrier and IET spectra, and suggest that surface hydroxyl (-OH) groups experience reorientation.

PACS numbers: 73.40.Gk, 74.50.+r, 73.40.Rw, 68.20.+t

In this paper we set out to explore the nature of the insulating barrier in metal-insulator-metal tunnel junctions. It is known that tunnel junctions left at room temperature for any length of time usually undergo changes in resistance.<sup>1</sup> In order to prevent this, the junctions are stored at a low temperature (i.e., liquid nitrogen at 77 K). To carry out useful studies of phenomena such as chemisorption of organic molecules on oxide surfaces, it is necessary to have some knowledge of the temporal behavior of the oxide barrier in junctions prior to chemisorption. This is particularly applicable to cases in which one is studying chemical changes occurring within the barrier (e.g., chemical reactions of molecules infused into oxide junctions<sup>2</sup>).

This work describes what happens to Al-oxide-Pb tunnel junctions during thermal annealing. By looking at junction resistance, barrier parameters (thickness, average barrier height, and the difference between the barrier heights at the Al and Pb electrodes), and inelastic electron tunneling (IET) peak intensities, one can study time-dependent effects occurring in the junction. One observes changes in the tunneling barrier and IET spectra indicating that surface hydroxyl groups (-OH) experience reorientation.

The Al-oxide-Pb junctions used in this study were prepared in a vacuum system which was first cleaned with a ~5 min oxygen discharge followed by ~15 min of argon plasma cleaning. An aluminum base film (2000 Å thick) was then evaporated onto a clean glass substrate. Oxidation of the base film was carried out in an oxygen-helium (40-60%)

plasma [using Matheson research-grade oxygen (99.99% purity) and Helium (99.9999% purity)] with a total gas-mixture pressure of about 200 μ Hg. To create the plasma, two circular concentric copper electrodes were used, the outer one being a circular band of copper sheet and the inner one a circular piece of copper rod. Typical plasma currents ranged from 2 to 6 mA with voltages of the order of 375-425 V (outer electrode positive, inner electrode negative) for a discharge time of about 30 min. Two lead electrodes (2000 Å thick) were then evaporated (at a rate of ~900 Å/min.) to form two junctions on the same substrate sharing a common base layer (one of which could be used as a control junction when required). The entire fabrication was done *without breaking the vacuum*. Once formed, junctions were cooled to 77 K in liquid nitrogen until ready for study. Measurements were taken at 4.2 K using an updated version of the bridge-minicomputer system described by Adler and Straus.<sup>1</sup>

Having briefly described junction fabrication, one should note that the insulating barrier formed in a plasma is not likely to be stoichiometric alumina and may contain other groups (e.g., -OH). The covering metal electrode will perturb the barrier in at least two ways: It may penetrate into the barrier, or it may alter the orientation of surface groups (i.e., sit on or squash them somewhat). Also, due to the work functions of the two-metal electrodes, a strong electric field will arise across the barrier<sup>3</sup> which will have some effect. For an idea of the field strength, a potential difference of 0.5 V (similar to differences in work functions) across a 10-Å junc-

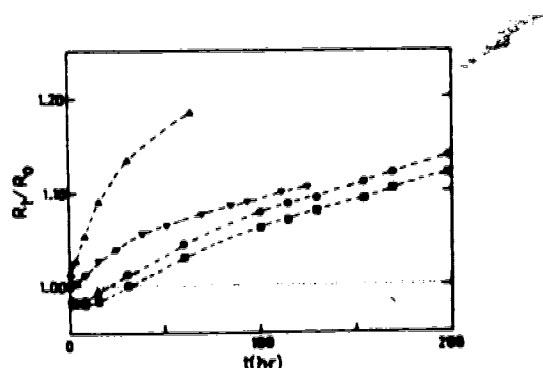


FIG. 1. This figure shows a plot of  $R_t/R_0$  versus  $t$  for several junctions, where  $R_t$  is the junction resistance at time  $t$ ,  $R_0$  is the initial resistance, and  $t$  is the total annealing time.

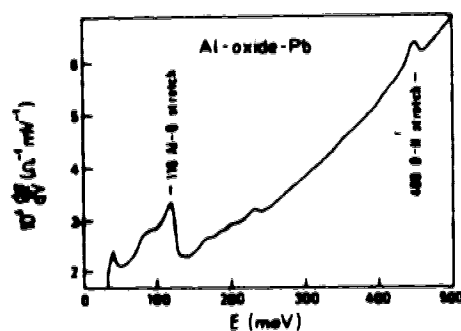


FIG. 2. A typical IET spectrum for an Al-oxide-Pb tunnel junction is shown. Peaks of interest occur at 118 meV and 450 meV.

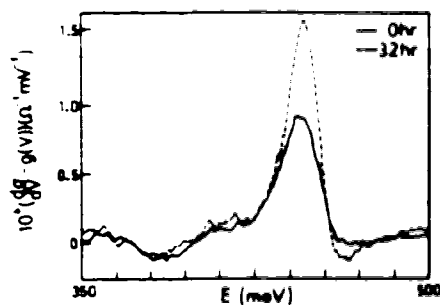


FIG. 3 The change in the 450-meV peak with annealing is shown here for two different times: 0 and 32 h.

tion gives a field of  $5 \times 10^4$  V/m. This may aid in group orientation and ionic diffusion.

The thermal annealing experiments were carried out by removing a junction from liquid-nitrogen temperature and placing it at room temperature, about  $20^\circ\text{C}$ , for the desired length of time. To prevent the ice which formed on the tunnel junction electrodes (when removed from liquid nitrogen to room air) from melting and subsequently damaging the junction, annealing was carried out in a vacuum. All annealing times referred to in this paper are cumulative times (i.e., total time the junction has been annealed). The most obvious parameter which changes with annealing is the junction resistance  $R$ . Figure 1 shows a plot of the resistance ratio  $R_t/R_0$  versus  $t$  (total annealing time) for a series of thermally annealed (open circuit) oxide junctions where  $R_0$  is the initial resistance (within a few minutes of junction formation), and  $R_t$  the resistance at time  $t$  (at  $-30$  mV). The curves suggest three regions: (1) An initial decrease (some curves drop below  $R_t/R_0 = 1.00$ ) in resistance (or none at all), (2) A rapid resistance increase which becomes, (3) a more gentle increase.

Other noticeable changes occur in the conductance  $\sigma$  versus applied bias  $V$ , and in the second derivative  $d\sigma/dV \equiv d^2I/dV^2$ , the IET spectrum. The spectrum of an oxide (Fig. 2) shows two main peaks of interest, the 450-meV peak due to surface OH stretching, and an Al-O stretching mode at 118 meV due to the aluminum oxide (all peak positions referred to in this paper are for the polarities Al nega-

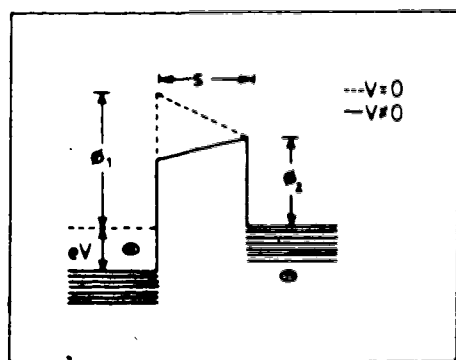


FIG. 4 The model for the trapezoidal barrier with thickness  $t$  and barrier heights  $\phi_1$  and  $\phi_2$  (at the Al and Pb electrodes, respectively) is shown here, with an applied bias  $eV$ .

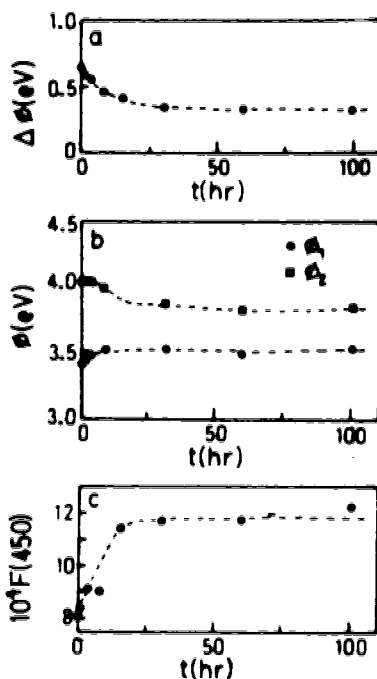


FIG. 5(a) A plot of the separation between barrier heights at the two electrodes  $\Delta\phi$  versus total annealing time  $t$  shows the decrease of  $\Delta\phi$  with time. (b) This plot of the barrier heights at the two electrodes versus time shows a decrease at the Pb side ( $\phi_2$ ) but little change at the Al side ( $\phi_1$ ). (c) This graph shows how the 450-meV peak intensity increases with annealing time and finally levels off.

tive and Pb positive). Upon thermal annealing one often sees noticeable changes in the spectrum of a particular junction: For example (Fig. 3), the OH mode at 450 meV increases in size and sharpens up slightly.

Some changes also occur in the shape of the conductance curves. One can conveniently characterize these curves' by calculating the barrier parameters, with  $s$ , the average barrier thickness,  $\bar{\phi}$ , the average barrier height [ $\bar{\phi} = \frac{1}{2}(\phi_1 + \phi_2)$  at zero bias], and  $\Delta\phi = \phi_2 - \phi_1$ , the differ-

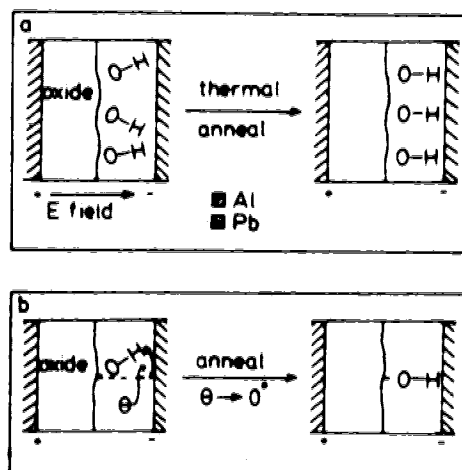


FIG. 6(a) A schematic representation of the tunnel barrier shows how the OH groups reorient under the influence of an electric field during thermal annealing. (b) Here, a close-up view shows how  $\theta$  decreases with reorientation and results in the hydrogen side of the OH group moving closer to the Pb electrode.

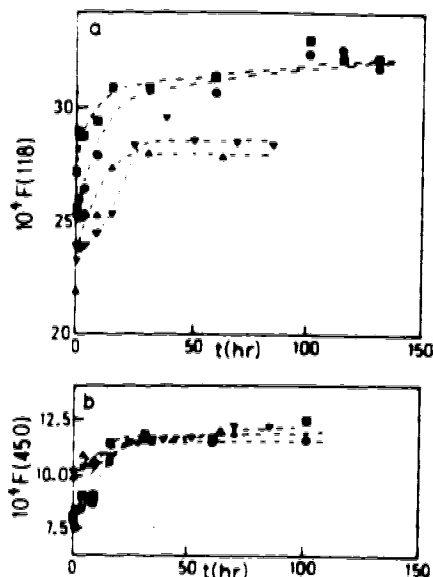


FIG. 7(a) A plot of the 118-meV (Al-O) intensity versus annealing time for several tunnel junctions. (b) This graph of the 450-meV (-OH) intensity versus annealing time for several tunnel junctions shows that for all the samples the same saturation intensity is reached.

ence of the barrier heights at the two electrodes (Fig. 4). This was done assuming a trapezoidal barrier and the WKB approximation following the method of Brinkman, Dynes, and Rowell<sup>6</sup> (Eq. 7). The model is not taken literally but rather as an indicator of the qualitative changes taking place in the barrier. For thermally annealed junction, one finds that  $s$ , the effective barrier thickness, increases with time (this does not mean the barrier is necessarily becoming physically wider but rather the tunneling resistivity is becoming greater), and that  $\bar{\phi}$ , the average barrier height, decreases with time. The most interesting results involve the barrier heights at the Al and Pb electrodes,  $\phi_1$  and  $\phi_2$ . Figure 5(a) shows a decrease in  $\Delta\phi$  which levels off within 40 h. In Fig. 5(b) one sees that  $\phi_1$ , the barrier height at the aluminum electrode, remains fairly constant whereas  $\phi_2$ , for the lead electrode, decreases and then levels off. This suggests that there has been an increase in positive charge density near the lead electrode. Another interesting quantity to study is the area under the peaks of interest in Fig. 2 referred as peak intensities. It should be noted that our data is calibrated and we thus work with absolute values of  $d\sigma/dV \equiv d^2I/dV^2$ , as opposed to raw second-harmonic signals. From the data, the integrated peak intensity is calculated by

$$F(V) = \int \left[ \frac{1}{\sigma_N} \frac{d\sigma}{dV} - g(V) \right] dV,$$

where  $\sigma_N$  is the conductance used to normalize  $d\sigma/dV$  (in this paper  $\sigma_N = \sigma(V_N) = \sigma(-30 \text{ meV})$ , since we did not sweep through zero bias in order to avoid structure due to the superconducting energy gap and phonons of Pb), and  $g(V)$  is the smooth background under the inelastic peak. One finds that the intensity of the 450-meV peak for the

junction described increases with time and tends to saturate [Fig. 5(c)].

Looking back over the results we find

- (1) A rapid 450-meV peak intensity increase to saturation,
- (2) A decrease in  $\Delta\phi$ ,
- (3) A decrease in  $\phi_2$  (the lead side becoming more positive),
- (4)  $\phi_1$  remains constant for the aluminum electrode,
- (5) A slight sharpening of the 450-meV peak.

Since there is a large electric field in the barrier ( $\sim 10^8$  V/m), a possible interpretation can be given by considering the reorientation of the surface hydroxyl groups on the aluminum oxide. The above mechanism is shown schematically in Fig. 6(a) where the originally quite random OH groups reorient themselves under the influence of the electric field. Figure 6(b) shows that, in realigning the OH dipole,  $\theta$  (the average angle of an OH group from the normal to the plane of the Pb electrode) tends to  $0^\circ$ , i.e., the OH stretch motion is more perpendicular to the Pb electrode. This will result in an intensity increase for this mode proportional to  $\cos^2 \theta$  for a stretching mode.<sup>8</sup> Secondly, Fig. 6(b) shows that with reorientation the positive hydrogen of the OH moves closer to the lead electrode, increasing the positive charge density near it; therefore  $\phi_2$  decreases while practically no effect is exerted on  $\phi_1$  at the Al side.

One also finds that upon annealing, the intensity of the 118-meV peak due to Al-O stretching increases in a manner similar to the 450-meV increase. By looking at the intensity-vs.-annealing time curves [Fig. 7(a)] for a few junctions, one can see that the lower the initial 118-meV intensity the greater the annealing effect (as measured by the ratio of saturation intensity at  $\sim 60$  h to initial intensity), suggesting that more reorientation can take place the lower the initial 118-meV intensity. Whereas the 118-meV intensities tend to saturate at different values, the 450-meV intensities all tend to saturate at approximately the same value [Fig. 7(b)]. This suggests that there is a certain "monolayer" coverage of surface OH for all junctions (which has its own particular initial orientation) while the amount of aluminum oxide [Fig. 7(a)] can vary.

To summarize, we have found that junctions subjected to thermal annealing undergo resistance changes (up and down) as well as changes in barrier parameters and IET peak intensities with time. This suggests reorientation of the insulating barrier (surface OH and aluminum oxide) under the influence of a natural electric field. Also, by looking at the values at which the IET peak intensities saturate, one deduces that there is a certain monolayer coverage of surface OH for all the junctions while the amount of aluminum oxide varies.

#### ACKNOWLEDGMENTS

We wish to thank Mr. Donald Patrick Mullin for technical help in the course of this work and NSERC for a grant in partial support of this project.

R. M. Handy, Phys. Rev. 126, 1968 (1962)  
R. C. Jaklevic and M. R. Gaertner, Appl. Surf. Sci. 1, 479 (1978)  
J. G. Adler and J. Straus, Rev. Sci. Instrum. 46, 158 (1975)  
J. G. Simmons, Phys. Rev. Lett. 1, 10 (1963)  
M. K. Konkin, R. Magno, and J. G. Adler, Solid State Commun. 26, 949 (1978)

W. F. Brinkman, R. C. Dyson, and J. M. Rowell, J. Appl. Phys. 41, 1915 (1970)  
R. Magno, M. K. Konkin, and J. G. Adler, Surf. Sci. 69, 437 (1977)  
D. J. Scalapino and S. M. Marcus, Phys. Rev. Lett. 18, 459 (1967)

## Annealing effects in tunnel junctions (voltage annealing)

M. K. Konkin and J. G. Adler

Department of Physics, University of Alberta, Edmonton, Alberta, Canada, T6G 2J1

(Received 29 February 1980; accepted for publication 19 June 1980)

This paper describes the time-dependent changes which occur in Al-oxide-Pb tunnel junctions as a result of voltage annealing (i.e., keeping a fixed bias across junction electrodes). By examining changes in junction resistance, barrier parameters (barrier thickness, average barrier height, and the separation between barrier heights at the two electrodes) and inelastic electron tunneling (IET) peak intensities, one finds that applying a voltage across the junction causes an accumulation or depletion of positive charge at the Al-oxide interface depending on the polarity of the applied bias. Along with charge redistribution, the voltage-induced electric field also enhances or retards other processes (such as reorientation of surface hydroxyl groups) which normally take place during thermal annealing.

PACS numbers: 73.40.Gk, 74.50.+r, 73.40.Rw, 68.20.+t

Previous work<sup>1</sup> has described some of the effects which occur in Al-oxide-Pb tunnel junctions when they are thermally annealed. The current paper describes the results of voltage annealing. In this, a constant voltage is applied across the junction electrodes to produce an electric field which adds or subtracts from the junction's intrinsic electric field. This intrinsic field is responsible for some of the changes observed in thermal annealing; thus, altering the field with an applied bias should help to clarify our knowledge of the annealing process. Information about junction resistance, barrier parameters, and inelastic electron tunneling (IET) peak intensities as they change under the influence of voltage annealing indicates that positive charge at the Al-oxide interface can be increased or decreased, depending on the polarity of the applied bias. Also, by proper choice of bias polarity, junction aging (i.e., any changes occurring within the junction after its completion) can be retarded.

The Al-oxide-Pb tunnel junctions used in this study (about 20) were prepared by first evaporating an aluminum base layer onto a glass substrate. Oxidation of the aluminum film in an oxygen-helium plasma discharge<sup>1</sup> to form the insulating barrier was then followed by the simultaneous evaporation of two lead top electrodes. In this manner, one junction of the pair served as a control (thermally annealed only) while the other junction was subjected to voltage annealing. Newly completed junctions had  $R_0A$  values (proportional to junction thickness) ranging from 15 to 55  $\Omega$  mm,<sup>2</sup> where  $R_0$  was the resistance of the virgin junction and  $A$  was the area. They were stored in liquid nitrogen, while measurements were taken at 4.2 K using an advanced version of the bridge-minicomputer system described by Adler and Straus.<sup>2</sup>

Having briefly described junction fabrication, one should note that the insulating barrier formed in the plasma is not likely to be stoichiometric alumina, and may contain other groups (e.g., -OH). The covering metal electrode will perturb the barrier in at least two ways: the electrode may penetrate into the barrier,<sup>3</sup> or it may alter the orientation of surface groups (e.g., surface OH) canting them somewhat. Also, due to the work functions of the two metal electrodes, a strong electric field will arise across the barrier.<sup>4</sup> For an idea of field strength, a potential difference of 0.5 V (similar to differences in work functions) across a 10-Å junc-

tion (these are typical barrier thicknesses found using ellipsometry<sup>5</sup>) gives a field of  $5 \times 10^8$  V/m. This field can aid in group reorientation and ionic diffusion.

The voltage annealing experiments were carried out at room temperature in a vacuum. The control junction was allowed to undergo thermal annealing (open circuit) while the other junction of the pair was biased at the desired voltage and polarity. We shall refer to a bias with Al positive, Pb negative as forward polarity (FP) and Al negative, Pb positive as reverse polarity (RP). Previous thermal annealing experiments showed that the intrinsic field of a junction was of forward polarity.

Interpretation of the annealing process is carried out by examining changes in junction resistance, barrier parameters, and inelastic electron tunneling peak intensities with respect to total annealing time. The junction resistance  $R$ , is the measured resistance (at -30 mV) at time  $t$  (total annealing time). Changes occurring in the shape of the conductance curves ( $\sigma$  versus bias  $V$  for a sweep range of  $\pm 500$  mV) can be characterized<sup>6</sup> by calculating the barrier parameters  $s$ , the average barrier thickness  $\bar{\phi}$ , the average height [ $\bar{\phi} = \frac{1}{2}(\phi_1 + \phi_2)$  at zero bias], and  $\Delta\phi = \phi_2 - \phi_1$ , the difference of the barrier heights at the two electrodes (values for the parameters  $\phi_1$  and  $\phi_2$  can be easily determined from the already calculated  $\bar{\phi}$  and  $\Delta\phi$ ). This was done assuming a trapezoidal barrier and the WKB approximation following the method of Brinkman, Dynes, and Rowell<sup>7</sup> [Eq. (7)]. The model is not taken literally but rather as an indicator of the qualitative changes taking place within the barrier. Finally, the last quantities of interest in this study are the areas under peaks of interest in the IET spectrum  $d\sigma/dV$  referred to as peak intensities. From our calibrated data, the integrated peak intensity  $I$  is calculated by

$$I = \int \left[ \frac{1}{\sigma_N} \frac{d\sigma}{dV} - g(V) \right] dV,$$

where  $\sigma_N$  is the conductance used to normalize  $d\sigma/dV$  [in this paper  $\sigma_N = \sigma(V_N) = \sigma(-30 \text{ meV}) = 1/R_0$ , since we did not sweep through zero bias in order to avoid structure due to the superconducting energy gap and phonon structure of Pb] and  $g(V)$  is the smooth background under the inelastic peak.<sup>3</sup>

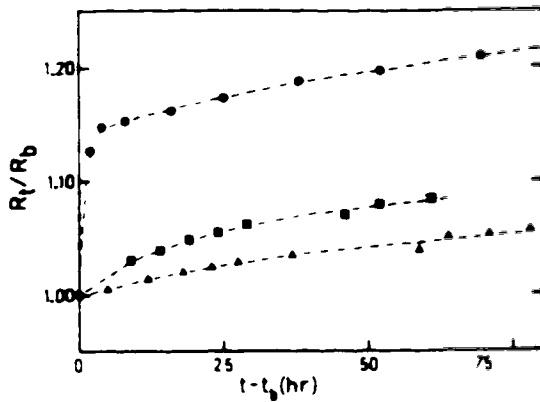


FIG. 1 This figure shows a plot of  $R_t/R_b$  vs  $t-t_b$  for three junctions biased at 0.5-V FP.  $R_t$  is the junction resistance at time  $t$ ,  $R_b$  is the resistance at the time of bias application  $t_b$ , and  $t$  is the total annealing time. For the circles, squares, and triangles,  $t_b = 0, 212,$  and  $324$  h, respectively. Each graph point is the value measured after several hours of 0.5-V FP annealing.

A number of observations were made in the course of the annealing studies. Changes in the control junction resistance, barrier parameters, and peak intensities were consistent with previous results.<sup>1</sup> In particular, reorientation of surface OH groups as monitored by the 450-meV peak (due to surface OH stretching) was suggested by (1) peak intensity increase to saturation, (2) a decrease in  $\Delta\phi$ , (3) a decrease in  $\phi_2$  (the lead side becoming more positive), and (4) little change in  $\phi_1$  for the aluminum electrode, all with respect to time. This reorientation of surface OH as well as the aluminum oxide (indicated by Al-O stretching at  $\sim 118$  meV) occurred due to the intrinsic field of the junction trying to align the dipoles. Voltage annealed junctions showed several new effects.

Junctions biased at 0.5 V with forward polarity (Al positive, Pb negative) show an increase in the slope of the resistance versus annealing time curves shortly after the desired voltage is applied. In Fig. 1 a graph of  $R_t/R_b$  versus time  $t-t_b$  (where  $R_t$  is the junction resistance at time  $t$ ,  $R_b$  is the resistance at the time of bias application  $t_b$ , and  $t$  is the

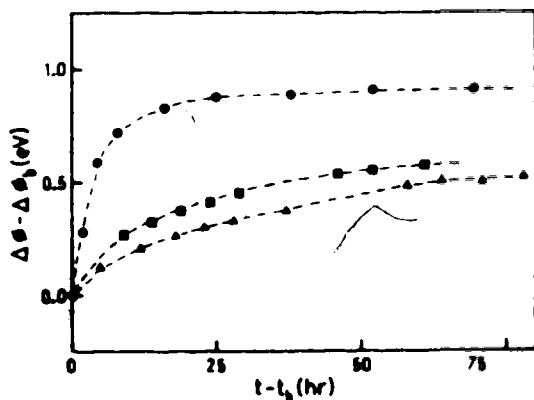


FIG. 2 A plot of  $\Delta\phi - \Delta\phi_b$  vs  $t-t_b$  for three junctions shows the effect of a 0.5-V FP bias on  $\Delta\phi$ , the difference of the barrier heights at the two electrodes. The junction age when biased  $t_b$  equals 0, 212, and 324 h for circles, squares and triangles, respectively.  $\Delta\phi_b$  is the value of  $\Delta\phi$  at time  $t_b$ .

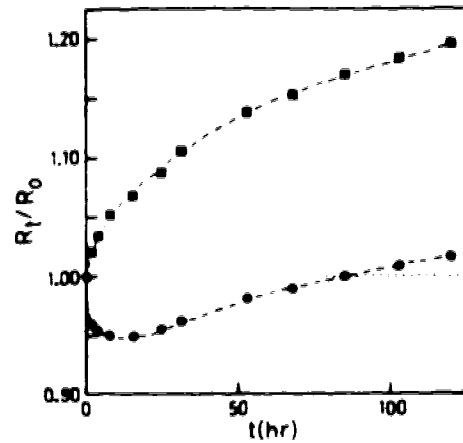


FIG. 3 The resistance behavior  $R_t/R_0$  vs time is shown here for a junction biased at 0.5-V RP (circles), and a thermally annealed control junction (squares).

total annealing time) illustrates this resistance increase for several junctions of different ages when initially biased. One sees that the increase soon slows down again and that the net resistance ratio increase after, say 50 h of application of the bias, diminishes the older the junction was to start with.

Another noticeable change is that which occurs in  $\phi_1$  and  $\phi_2$ —the potentials at the Al and Pb electrodes, respectively (depending on the nature of the sample  $\phi_1$  can be greater or smaller than  $\phi_2$ ). Following application of an annealing bias, it is found that  $\Delta\phi = \phi_2 - \phi_1$  increases in time and finally levels off as shown in Fig. 2 by  $\Delta\phi - \Delta\phi_b$  vs  $t-t_b$  ( $\Delta\phi_b$  refers to the value of  $\Delta\phi$  at time  $t_b$ ). It is seen also that an age dependence is exhibited by the magnitude of the effect. One should note that it is  $\phi_1$  which decreases markedly while  $\phi_2$  changes only a little. This implies that the barrier at the aluminum electrode acquires positive charge with time which eventually saturates as long as the biasing voltage is maintained. This charge, moreover, is trapped just within the barrier otherwise, like a capacitor, it would drain off as the annealing voltage was reduced to zero.

If junctions are annealed using reverse polarity (Al negative, Pb positive) at 0.5 V, the results are different. Looking at  $R_t/R_0$  vs  $t$  ( $R_0$  is the resistance value at  $t=0$ ), one finds an initial decrease in resistance which eventually increases slowly (Fig. 3). The barrier height at the Al electrode  $\phi_1$  goes up (implying that the Al side has become less positive) while that at the Pb electrode  $\phi_2$  remains constant.

These resistance changes as well as the behavior of  $\phi_1$  (Fig. 4) and  $\phi_2$  for a biased junction suggest movement of positive Al ions in and out of the barrier at the Al-oxide interface. When forward polarity is utilized, aluminum ions may be created at the aluminum electrode and drift a short way into the oxide barrier under the influence of the applied field. Such an occurrence raises the amount of positive charge near the Al electrode ( $\phi_1$  thus decreases) and increases junction resistance since the inclusion of Al ions within the oxide makes the barrier denser near the Al-oxide interface. On the other hand, application of a reverse polarity bias causes an initial resistance decrease and an increase in  $\phi_1$ . This indicates that some already existing positive

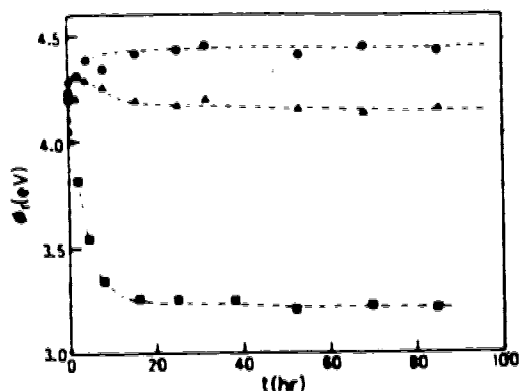


FIG 4 This figure illustrates the behavior of the barrier height at the Al electrode  $\phi$ , vs time for junctions subjected to 0.5-V RP (circles), 0.5-V FP (squares), or thermal annealing only (triangles).

charge is moved out of the barrier, which is reasonable since a negative potential has now been applied at the Al side.

One can account for the age dependence of the amount of change in  $R_t/R_0$  and  $\Delta\phi$  by noting the behavior of a voltage annealed (FP) junction once the annealing bias is removed. Figure 5 shows what happens. A decrease in  $\Delta\phi$  [Fig. 5(a)] occurs and  $\phi$  increases suggesting that the amount of positive charge near the Al electrode is being depleted. Looking now at the junction's resistance curve [Fig. 5(b)], it is seen that as charge depletion occurs, resistance increases. This leads one to believe that Al ions are being neutralized, and remain within the barrier as opposed to drifting back out to the Al electrode. The age effect can now be explained as follows. As a junction anneals, Al ions are created and drift into the junction due to its intrinsic field or under the influence of an externally applied field. The ions, once having

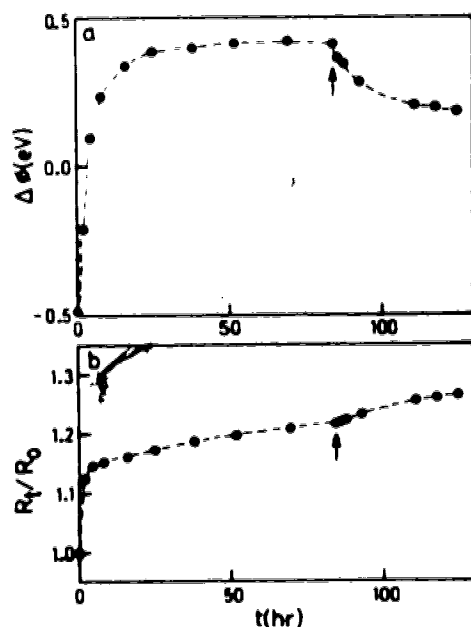


FIG. 5(a). Here we see the decrease in  $\Delta\phi$  after the removal of a 0.5-V FP bias. The arrow indicates the beginning of thermal annealing. (b) The resistance behavior of a junction during voltage annealing (0.5-V FP) and then thermal annealing (starting at the arrow) is shown.

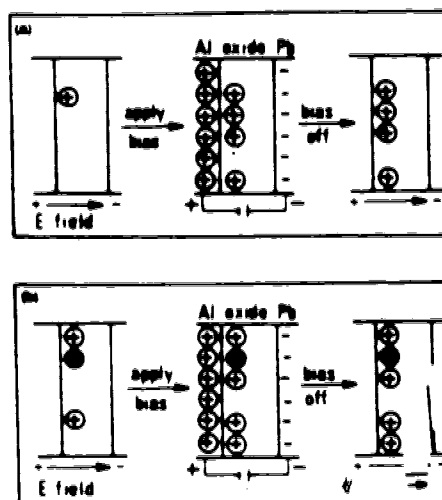


FIG 6(a) This figure shows the response of a "young" junction to FP biasing. In the first picture many vacancies exist at the Al-oxide interface. When a bias is applied (second picture) ions are created and can drift into the barrier to fill the vacancies. They remain trapped here after the bias is removed (picture three). (b) Here, the response of an "old" junction to FP biasing is shown. Vacancies are filled the same way as described in Fig. 6(a) except that there are fewer vacancies to begin with. Circles with + signs represent Al ions, and shaded-in circles denote Al atoms.

entered the barrier are eventually neutralized and new ions can be formed (maintaining a type of dynamic charge equilibrium). As a junction ages, vacancies for new ions to occupy within the insulator are diminished since some have already been filled. Thus, when an external bias is applied to an old junction as opposed to a newer one, its response is not as great simply because there are not as many vacancies in the barrier for new Al ions to fill and produce their effects. This is illustrated in Fig. 6. On the subject of aging, one finds that junction aging can be suppressed by the application of a reverse polarity bias. We will discuss this later.

Now, we turn to see what effects voltage annealing has on IET peak intensities. Looking at an oxide spectrum (Fig. 7), one notes peaks of interest at  $\sim 118$  and 450 meV due to

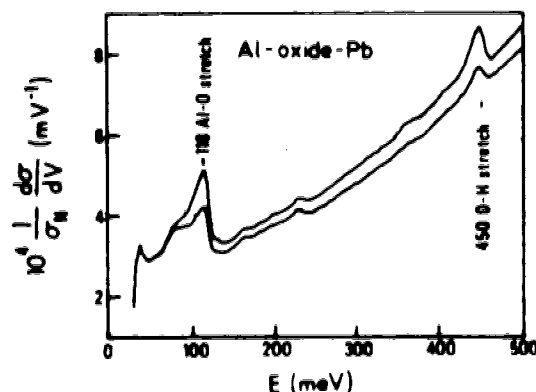


FIG. 7. The two curves are IET spectra for an Al-oxide-Pb junction at two different times. The upper curve shows the effect that 70 h of 0.5-V FP voltage annealing has on the virgin sample (lower curve). Peaks of interest occur at 118 and 450 meV.

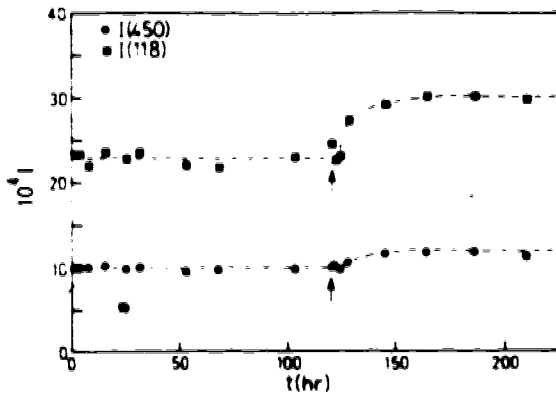


FIG. 8 This plot of peak intensity  $I$  vs time shows how reverse polarity (0.5 V) annealing suppresses any changes in  $I$  (0–120 h). If the bias is removed (at the arrow) the junction thermally anneals and peak intensities increase.

Al-O and O-H stretching, respectively. When voltage annealing is carried out with a 0.5-V FP bias, one finds the 118- and 450-meV peak intensities increase with time to values greater than those in the thermal annealing case. This suggests that with an electric field greater than the intrinsic field alone, the surface hydroxyl and aluminum oxide may experience further reorientation. On the other hand, the application of a field of 0.5-V RP is found to inhibit the change in peak intensities which normally occurs in virgin junctions under the influence of their intrinsic field (Fig. 8). This implies that the intrinsic field of the junction is neutralized by the 0.5-V RP bias, thereby leaving no electric field across the junction to reorient the molecular groups within. If the bias is now removed, the junction thermally anneals as before; resistance and peak intensities increase. By applying such a reverse field to neutralize the intrinsic field, one can thus delay the aging of a tunnel junction.

Having looked at the voltage annealing behavior, one can now use it to aid in explaining some results observed in the thermal annealing experiments. A number of thermally annealed junctions initially showed an unexplained drop in junction resistance similar to the one observed in voltage annealing with reverse polarity. Unlike RP annealing the peak intensities increased in the usual way. A close look now at  $\phi_1$  for those junctions with a pronounced resistance dip shows that  $\phi_1$  initially increases a little (Al side becoming more negative). This, as well as the resistance drop, could be accounted for if positive Al ions left the barrier. However, since the intrinsic field of the junction has the Al electrode positive, there seems to be a contradiction unless one considers what may occur in the course of junction fabrication. Looking at the barrier during growth, one might imagine it to be aluminum oxide with positive Al ions near the aluminum electrode and OH groups standing up on the growing alumina surface [Fig. 9(a)]. Subsequent evaporation of the Pb cover electrode will tend to squash the OH groups, leaving them canted as shown in Fig. 9(b). This movement of the OH group's hydrogen closer to the oxide will cause a greater electrostatic repulsion between the aluminum ions and the hydroxyl hydrogens than existed prior to the deposition of

the Pb cover electrode. Since the Al ions are smaller and more mobile than the OH groups, the mutual electrostatic repulsion can force some ions out of the barrier [Fig. 9(c)]. This takes place only until the intrinsic field of the junction can reorient the OH groups sufficiently to relieve the repulsive force. At this point, Al ions under the influence of the intrinsic field are once more able to enter the barrier [Fig. 9(d)] and cause resistance increases. Some thermally annealed junctions show the above behavior; some do not. Factors influencing this probably include (1) the manner in which the Pb electrode is evaporated and (2) the number and distribution of Al ions within the oxide.

In this paper, we have introduced a new technique for the study of ion motion and behavior within tunnel junctions. By applying a 0.5-V FP annealing voltage to a junction, one causes positive charges, presumably aluminum ions to accumulate at the Al-oxide interface. These ions serve to increase  $\Delta\phi$  ( $\phi_1$  decreases) as well as the junction resistance. When the voltage is removed, neutralization of ions within the barrier is reflected by the fall of  $\Delta\phi$  ( $\phi_1$  now increases). The accumulated charge also serves to enhance the junction's intrinsic electric field which further aids group reorientation. When a 0.5-V RP bias is applied, some positive charge is removed from the barrier and junction resistance initially falls. It rises slowly afterwards, perhaps due to neutralization of any remaining charge within the barrier. Peak intensities do not change because the magnitude of the bias seems sufficient to negate the junction's intrinsic field, thereby leaving no electric field to reorient molecular groups. Junction aging is thus postponed until the reverse polarity bias is removed, at which point normal thermal annealing occurs. Finally, an explanation for the resistance dip observed in some thermally annealed junctions has been suggested as due to a temporary electrostatic repulsion occurring between Al ions and the H of surface hydroxyl groups after the Pb cover electrode has been evaporated.

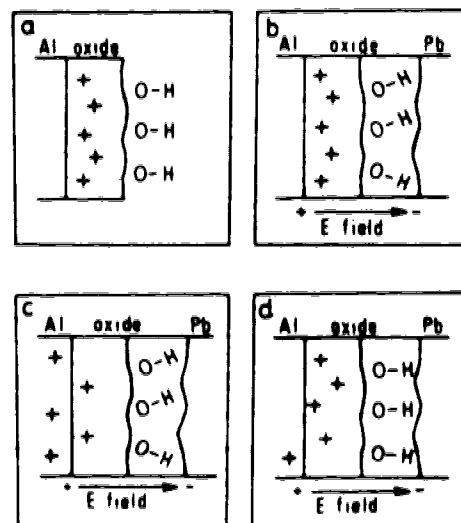


FIG. 9 This figure shows how evaporation of the Pb electrode on the growing oxide can perturb the surface hydroxyl groups and cause expulsion of Al ions out of the barrier due to electrostatic repulsion.



**ACKNOWLEDGMENTS**

We wish to thank NSERC for a grant in partial support of this project and D. Mullin (B.O.Y. 1954) for technical help in the course of this work.

<sup>1</sup>M. K. Konkin and J. G. Adler, *J. Appl. Phys.* **50**, 125 (1979).

<sup>2</sup>J. G. Adler and J. Straus, *Rev. Sci. Instrum.* **46**, 158 (1975).

<sup>3</sup>R. Magno, M. K. Konkin, and J. G. Adler, *Surf. Sci.* **69**, 437 (1977).

<sup>4</sup>J. G. Simmons, *Phys. Rev. Lett.* **1**, 10 (1963).

<sup>5</sup>K. Knorr and J. D. Leslie, *Solid State Commun.* **12**, 615 (1973).

<sup>6</sup>M. K. Konkin, R. Magno, and J. G. Adler, *Solid State Commun.* **26**, 949 (1978).

<sup>7</sup>W. F. Brinkman, R. C. Dynes, and J. M. Rowell, *J. Appl. Phys.* **41**, 1915 (1970).